

**Università degli Studi di Bergamo**



Dottorato di ricerca in Tecnologie dell'Energia e dell'Ambiente

XXI Ciclo

**BOILING OF R134a INSIDE A GLASS  
MINICHANNEL.  
A NEW APPROACH OF FLOW PATTERN  
CHARACTERIZATION BASED ON FLOW  
VISUALIZATION**

PhD Thesis of

**Dott. Ing. Stefano Dall'Olio**

A. A. 2007-2008

**Supervisor: Chiarissimo Professor Marco Marengo**



## CONTENTS

CONTENTS .....	3
ABSTRACT .....	9
LIST OF FIGURES .....	12
LIST OF TABLES .....	16
NOMENCLATURE .....	17
1. INTRODUCTION AND MAIN OBJECTIVES .....	19
1.1. Summary of the thesis .....	22
2. FUNDAMENTAL DEFINITION AND FLOW PARAMETERS .....	23
2.1. Two-phase flow .....	23
2.2. Vapor quality .....	23
2.3. Velocities .....	24
2.3.1. True average velocities .....	25
2.3.2. Superficial velocities .....	25
2.3.3. Drift velocities .....	26
2.4. Void Fraction .....	26
2.5. Definition of non-dimensional numbers .....	27
2.5.1. Reynolds number .....	27
2.5.2. Weber number .....	29
2.5.3. Boiling number .....	30
2.5.4. Bond number .....	30
2.5.5. Martinelli parameter .....	31
3. STATE OF THE ART REVIEW .....	32
3.1. Flow patterns in conventional channels .....	32
3.2. Flow Patterns in Horizontal Tubes .....	32
3.2.1. The study of Kattan, Thome, Favrat [15] .....	33

3.2.2.	The Triplett, Ghiaasiaan, Abdel- Khalik and Sadowski study [16].....	36
3.2.3.	The Zürcher, Favrat, Thome study [19] .....	37
3.2.4.	The Kawahara, Chung, and Kawaji study [21] .....	37
3.2.5.	The work of Zun [22] .....	39
3.2.6.	The study of Yu, Lin and Tseng [23] .....	40
3.2.7.	Flow pattern map of Thome and El Hajal [24].....	40
3.2.8.	Flow pattern map of Revellin and Thome [31] .....	42
3.2.9.	The work of Wojtan, Ursenbacher and Thome [33].....	45
3.2.10.	The study of Revellin and Thome [37].....	47
3.2.11.	Probabilistic flow pattern map of Jassim-Newell-Chato [42] .....	48
3.3.	General Considerations about the results found in the literature.....	50
3.4.	Void fraction.....	51
3.4.1.	The study of Triplett, Ghiaasiaan, Abdel-Khalik, LeMouel, McCord [16].....	51
3.4.2.	The study of Wojtan, Ursenbacher, Thome [30] .....	53
3.4.3.	The study of Kawahara, Chung and Kawaji [21] .....	54
3.5.	Experimental measurements in two phase flow .....	55
3.6.	Conclusions .....	56
4.	EXPERIMENTAL APPARATUS .....	59
4.1.	Starting point.....	59
4.2.	The experimental test-rig.....	60
4.3.	The new test section .....	61
4.4.	The new heating system .....	62
4.5.	Data acquisition devices .....	64
4.6.	The experimental condition and the flow visualization.....	66
4.7.	Conclusions .....	69
5.	PREDICTION OF THE HEAT FLUXES IN THE TEST SECTION.....	70
5.1.	Global heat fluxes.....	70
5.1.1.	Heater numerical simulation-axial conduction.....	71
5.1.2.	Lumped thermal simulation: SINDA/FLUINT .....	72
5.1.3.	Results .....	73

5.2.	Conclusions .....	76
6.	MEASUREMENTS AND ACCURACY OF THE MAIN PHYSICAL QUANTITIES .....	78
6.1.	Data measured .....	78
6.1.1.	Pressure drop .....	78
6.1.2.	Refrigerant thermodynamic data .....	78
6.1.3.	Heat flux .....	78
6.1.4.	Vapor quality .....	79
6.1.5.	Void Fraction.....	79
6.2.	Experimental accuracies .....	79
6.2.1.	Diameter of the tube .....	80
6.2.2.	Coating/evaporator length .....	80
6.2.3.	Pressure drop .....	80
6.2.4.	Mass flux .....	80
6.2.5.	Temperature.....	81
6.2.6.	Power supply .....	81
6.2.7.	Heat flux .....	81
6.3.	Conclusions .....	82
7.	IMAGE ANALYSIS TECHNIQUE.....	83
7.1.	Introduction to image analysis .....	83
7.1.1.	Image digitisation .....	83
7.1.2.	Pixel depth.....	83
7.1.3.	Image-Pro® Plus 4.5.1 .....	84
7.1.4.	Main steps of the automated bubble recognition routine .....	85
7.1.5.	Mathematical processing of the bubbles geometrical features.....	88
7.2.	Error in the bubble identification process .....	88
7.3.	Parameters considered for the flow pattern identification.....	89
7.4.	Automatic flow pattern identification .....	90
7.4.1.	Identification criteria .....	90
7.4.2.	Statistical tools to operate and validate flow pattern identification.....	90

7.5.	Conclusions .....	91
8.	EXPERIMENTS PERFORMED .....	93
8.1.	First group .....	93
8.2.	Second group.....	94
9.	RESULTS .....	96
9.1.	First group of experiments .....	96
9.1.1.	Void fraction.....	96
9.1.2.	Bubble diameter .....	99
9.1.3.	The $\tau$ parameter .....	101
9.2.	Second group of experiments .....	103
9.2.1.	Void fraction vs vapour quality .....	103
9.2.2.	Dimensionless Bubble diameter vs vapour quality .....	105
9.2.3.	$\tau$ parameter vs vapour quality .....	105
10.	GENERAL CONCLUSIONS .....	108
10.1.	First group of experiments .....	108
10.2.	Second group of experiments .....	108
11.	FUTURE WORK AND LATEST RESULTS .....	110
	BIBLIOGRAPHY .....	112
	PUBLICATIONS .....	116
	APPENDIX .....	117
I.	IMAGE ANALYSIS OF A TWO PHASE FLOW IN A BUNDLE OF MINI-CHANNELS USING THE COMMERCIAL CODE IMAGE PRO® P US R 4.5.1 ...	117
I.1.	The processed videos.....	117
I.2.	The main steps of bubble contour extraction .....	122
I.3.	Results .....	127

I.4.	Conclusions .....	131
II.	Fluid Physical properties .....	132

## ACKNOWLEDGEMENTS

The years of the PhD have been really interesting and unforgettable for the variety of the work conducted and for the people met inside and outside the lab.

A special thank goes to Prof. Marco Marengo who guided me during this period, that with his special enthusiasm and scientific cleverness stimulated me to conduct my work in the best possible way, founding always a solution to the problems met and opening new ways for the research.

Then Prof. Cossali for the patient and global supervision of the work, and the colleagues Simona, Elena, Carlo, Stefan, Alfio, Claudio, Stefano, Cristina, Luca, Francesco, Gabriella, Francesca with whom I spent really friendly moments and who had a lot of patience in my many days where I had not enough time for them.

Then to my mum, my father, my brother Francesco, my sister Chiara and my wife Lucija. They were with me all the days of these three years, supporting me and renovating my motivation and enthusiasm for the work.

In the end, all the friends and all the people met around the world that I forgot to mention here. Thanks for their words, the time they spent with me and the good words they said.

*Stefano Dall'Olio*

## ABSTRACT

In the interest of providing higher cooling capability for microtechnologies, the fundamentals of two-phase heat transfer in microchannels are being studied more extensively. Many two-phase flow and heat transfer prediction methods exist for vaporization inside macrochannels but these are not suitable to use for microchannels due to small-scale phenomena. Therefore, research is underway to investigate these small-scale phenomena and characterize the two-phase flow process. The most important parameters controlling two-phase flow in microchannels are bubble frequencies, lengths and velocities, coalescence of bubbles and flow pattern transitions. For these reasons, it is appropriate to apply an optical measurement technique to characterize as much quantitatively as possible the flow pattern transitions and to measure the frequency, velocity and length of vapor bubbles in microchannels, in particular at each portion of the evaporator in which the different two phase flows are formed.

In my work, these features were measured and/or detected by an optical measurement technique which begins with the acquisition of thousands of frames of the two phase flow inside a glass tube with a high speed video camera. The frames of each video are then processed using a program called Image Pro Plus® in order to have as much objectivity as possible in the classification of the different flow pattern and in the creation of the flow pattern maps.

The main reason because it is desirable to develop a flow pattern map for predicting the flow regimes of two-phase flow in microchannels is to better predict heat transfer coefficients in microcooling elements and heat spreaders for electronic cooling.

The complexity of identifying flow regimes and their transitions comes from the difficulties in obtaining good high speed images, in the interpretation of the flow (subjectivity and pattern definition depending on the author), and also in choosing the channel size that determines either macro or microscale or the transition between them.

With these ideas in mind, a new test rig to study R134a flow boiling inside mini and micro-channels has been designed and constructed during the last two years.

The test section is the most innovative part of all the system and is made up of a glass tube and is heated by a number of Indium Tin Oxide (ITO) conductive layers, distributed along the entire length of the outer surface of the tube. The use of more than one heater was done in order to have a very accurate control on the power provided to the fluid, and to be able to reach higher values of heating capacity compared to the configuration of just one heater.

Thanks to the choice of ITO layers [26, 41] it is possible to visually analyse the phenomena and mechanisms governing the boiling process, such as bubble nucleation, bubble growth, departure and bubble lift-off, and to improve the understanding of the transition lines in flow pattern maps.

The entire system is very versatile, allowing an easy substitution of the test section glass tube, ranging from an internal diameter of 4 mm till the smallest of 0.5 mm.

From the point of view of the maximum value of the heat flux that the heaters are able to provide to the fluid, it is possible to reach a value of  $45 \text{ kW/m}^2$  with the 4 mm internal diameter tube, up to  $400 \text{ kW/m}^2$  with the smallest one.

The results and the images presented in this thesis are referred to the 4 mm internal diameter configuration, with eight ITO heaters, each being able to provide a power of around 20 W. The maximum mass flux for the present situation is about  $115 \text{ kg/m}^2\text{s}$ , and the temperature range of the fluid at the inlet of the test section can be between 0 and  $30^\circ\text{C}$ .

In parallel with the design and construction of the experimental setup, the fundamental part of the test section, which means one ITO layer and the uncoated glass tube following and preceding it, has been numerically simulated and studied with a lumped parameter code developed by NASA called SINDA/FLUINT (now distributed and further developed by Cullimore).

The main objective of this numerical analysis is to understand how and in which quantity the power provided by the heater is transmitted to the fluid or lost in radiation from the surface or transferred to other parts of the glass tube by axial conduction at the boundary of the ITO.

A new image processing technique based on a new routine created inside the commercial code Image Pro<sup>®</sup> Plus has been developed and applied to the study of R134a two-phase flow inside mini and micro-channels.

The new image processing technique has been developed to perform visualization of forced convection saturated R-134a boiling in an horizontal glass mini tube.

The routine extracts the bubble contours, measures geometrical features of each frame and collect the data both analytically and statistically. These two ways of data acquisition allow the post processing code to analyse and decide whether the flow regime is bubbly, slug or elongated bubble flow. The principle is mostly based on the bubble geometrical features, and the main criterions existing in literature.

The robust design and the flexibility of the automated module enable it to process accurately many different types of videos.

Compared to the other two main optical flow pattern identification methods, the first developed by Revellin and Thome [36] based on a frequency analysis of the light signal from a laser-diode system, Newell and Jassim [42] more focused on the development of an image based recognition software image analysis, the method presented in this work is more simple, easy to use and a wider range of flow patterns can be analyzed.

Till now the flow pattern classification has been accomplished mostly subjectively, sometimes being not possible for the researchers to compare their results, and in many cases some author stressed the importance to reach a way of flow pattern identification that could be as objective as possible and not based on the subjectivity of the scientist.

In this work an easy way to obtain an objective classification technique is presented, and the parameters that are at the basis of the identification will be analysed statistically in order to understand the efficiency of the model, to optimize the values and to validate the results.

Moreover, a detailed statistical analysis has also been carried out in order to decide the number of samples needed for a flow characterization and to validate the classification itself.

Finally a special attention was devoted to the incipient boiling process, i.e. the analysis of the flow characteristics for very low values of the vapour quality, since the transparent heater is allowing the visualization of the bubbles originates by the nucleation sites on the glass surface.

The range of the flow parameters of the results presented in this thesis are: mass flow rate between 20 and 122 kg/m<sup>2</sup> s and the heat flux between 200 and 45000 W/m<sup>2</sup>, at the saturation temperatures of 20 and 25 °C.

## LIST OF FIGURES

Fig. 1. Steiner flow pattern map .....	20
Fig. 2. Flow observation for R134a, $D=0.5$ mm, $L=70.7$ mm, $G=500$ kg/m <sup>2</sup> s .....	32
Fig. 3. Stratified two-phase flow cross section.....	34
Fig. 4. Flow pattern map of Kattan compared to Steiner for R410A at $T_{\text{sat}}=5^{\circ}\text{C}$ in a 13.84 mm internal diameter tube at heat fluxes of 7.5, 17.5 and 37.5 kW/m <sup>2</sup> . ....	35
Fig. 5. Comparison between the experimental flow patterns with the flow patterns of Fukano and Kariyasaki representing their 1 mm-diameter circular test section. ....	36
Fig. 6. Flow pattern map of Thome-El Hajal for R410A at $T_{\text{sat}}=5^{\circ}\text{C}$ in a 13.84 mm internal diameter tube with its equations evaluated at three fixed mass velocities: $G=100, 200, 300$ kg/m <sup>2</sup> s.....	42
Fig. 7. Flow patterns and transitions for R245fa, $D=0.5$ mm, $L=70.7$ mm, $G=500$ kg/m <sup>2</sup> s and $T_{\text{sat}}=35^{\circ}\text{C}$ . ....	43
Fig. 8. Flow pattern maps with experimental transition lines for R134a, $D=0.5$ mm, $L=70.7$ mm, $T_{\text{sat}}=35^{\circ}\text{C}$ .....	45
Fig. 9. New flow pattern maps for R22 at $T_{\text{sat}}=5^{\circ}\text{C}$ and $D=13.84$ mm at $G=300$ kg/m <sup>2</sup> s and four initial heat fluxes: (a) 7.5 kW/m <sup>2</sup> , (b) 17,5 kW/m <sup>2</sup> , (c) 37.5 kW/m <sup>2</sup> , (d) 57,5 kW/m <sup>2</sup> .....	46
Fig. 10. Schematic of three zone evaporation model. ....	47
Fig. 11. Flow pattern maps with experimental transition lines for R134a, $D=0.509$ mm, $L=50$ mm, $T_{\text{sat}}=30^{\circ}\text{C}$ . ....	48
Fig. 12. Probabilistic two-phase flow regime map data for R410A, 100 kg/m <sup>2</sup> s, 25°C, 3.9 mm I.D. tube.....	49
Fig. 13. Comparison of measured void fractions with predictions of various correlations. (a) homogeneous model; (b) Chexal et al.....	52
Fig. 14. Void fraction evolution for stratified-wavy/intermittent flow. ....	53
Fig. 15. Conventional visualization windows in two-phase flow.....	55
Fig. 16. Stratified flow regime photographs of Barbieri, Saiz-Jabardo and Bandararra. Top: stratified flow; middle and bottom: stratified-wavy flow. Tube diameter: 15.8 mm. ....	56
Fig. 17. Mass flux vs. vapour quality map showing the experiments performed during the thesis. ....	57
Fig. 18. The first version of the test rig built to make experiments regarding the cooling of a strip of a particle detector at FERMILAB, Chicago. ....	59
Fig. 19. Experimental test rig scheme .....	60

Fig. 20. Schematic view of the basic unit of the test section: the glass tube, the heaters and the glass chamber that encloses the tube. ....	61
Fig. 21. Test section in the operating condition. ....	62
Fig. 22. Image of the test section showing the electrical wires that provide power to the ITO heaters and the white connectors that fix the wires at the borders of the coating. ....	63
Fig. 23. Test section instrumentation scheme. ....	64
Fig. 24. Electrical scheme of one electronic board designed to control the amount of power provided by each heater. ....	65
Fig. 25. Experimental set-up acquisition scheme. ....	65
Fig. 26. LabVIEW control panel interface. ....	66
Fig. 27. Temperatures with and without the IR filter. ....	67
Fig. 28. Image of the test section, where it is possible to notice the high speed camera (1), the light source (2) and the test section (3). ....	68
Fig. 29. Electronic boards to control the amount of power given to each heaters. ....	69
Fig. 30. Scheme of the heat fluxes in one basic unit of the test section. ....	70
Fig. 31. Layout of the Pipe as drawn in SINDA. ....	72
Fig. 32. Radiative and convective heat transfer between the tube and the air modelled with SINDA/FLUINT. ....	73
Fig. 33. Simulation of the power distribution in a portion of the test section including the heater and two parts of uncoated glass. The importance of axial conduction can be noticed. ....	74
Fig. 34. Comparison with the power given to the flow in each node, in the ideal case without axial conduction, with axial conduction and with the 99% value of total powerR. ....	75
Fig. 35. Simulation of the power distribution at the end of a ITO heater with different heat provided. ....	76
Fig. 36. Percentage difference between real and nominal heat flux at various value of power provided. ....	77
Fig. 37. Image-Pro® Plus 4.5.1 usual working window. ....	85
Fig. 38. Cyclic procedure to perform the flow pattern identification of several images. ....	86
Fig. 39. Effect of the automatic image analysis steps visible in a frame. ....	87
Fig. 40. Example of datasheet obtained from the image analysis of one video. ....	87
Fig. 41. a) relationship between pixels and the unit length; b) zoom on the bubble contour during the segmentation process in order to find the relative error of the area measurement. ....	88

Fig. 42. Vapor quality-mass flux graph to show the thermodynamic characteristics of the experiments performed in the first group. ....	93
Fig. 43. Convective heat transfer coefficient as a function of the vapour quality. ....	94
Fig. 44. Three position along the tube at which the video to study the evolution of the flow pattern have been recorded. ....	95
Fig. 45. Void Fraction as a function of the vapour quality and the mass flux. Fluid: R134a, D=4mm, $T_{sat}=22^{\circ}\text{C}$ , $G= 20\text{-}120\text{ kg/m}^2\text{ s}$ . ....	97
Fig. 46. Void Fraction as a function of the vapour quality and the mass flux. Fluid: R134a, D=4mm, $T_{sat}=22^{\circ}\text{C}$ , $G= 20\text{-}120\text{ kg/m}^2\text{ s}$ . ....	98
Fig. 47. Void Fraction as a function of the vapour quality and the mass flux. Fluid: R134a, D=4mm, $T_{sat}=22^{\circ}\text{C}$ , $G= 20\text{-}120\text{ kg/m}^2\text{ s}$ . ....	99
Fig. 48. Dimensionless bubble diameters as a function of the vapour quality and the mass flux. Fluid: R134a, D=4mm, $T_{sat}=22^{\circ}\text{C}$ , $G= 20\text{-}120\text{ kg/m}^2\text{ s}$ . ....	100
Fig. 49. Dimensionless bubble diameters as a function of the vapour quality and the mass flux. Fluid: R134a, D=4mm, $T_{sat}=22^{\circ}\text{C}$ , $G= 20\text{-}120\text{ kg/m}^2\text{ s}$ . ....	101
Fig. 50. $\tau$ parameter as a function of the vapour quality and the mass flux. Fluid: R134a, D=4mm, $T_{sat}=22^{\circ}\text{C}$ , $G= 20\text{-}120\text{ kg/m}^2\text{ s}$ . ....	102
Fig. 51. $\tau$ parameter as a function of the vapour quality and the mass flux. Fluid: R134a, D=4mm, $T_{sat}=22^{\circ}\text{C}$ , $G= 20\text{-}120\text{ kg/m}^2\text{ s}$ . ....	103
Fig. 52. Void fraction evolution along the test section tube. a) after the first heater, b) 30 cm ahead of the first position, c) 70 cm ahead of the first position. ....	104
Fig. 53. Dimensionless bubble diameter evolution along the test section tube. a) after the first heater, b) 30 cm ahead of the first position, c) 70 cm ahead of the first position. ....	106
Fig. 54. $\tau$ parameter evolution along the test section tube. a) after the first heater, b) 30 cm ahead of the first position, c) 70 cm ahead of the first position. ....	107
Fig. 55. Bubble nucleation inside the test section. a) $T_{in}= 21^{\circ}\text{C}$ , $G=125\text{ kg/m}^2\text{ s}$ , Power= 2 W, first heater; b) $T_{in}= 21^{\circ}\text{C}$ , $G=125\text{ kg/m}^2\text{ s}$ , Power= 3,7 W, first heater	110
Fig. 56. $T_{in}= 21^{\circ}\text{C}$ , $G=125\text{ kg/m}^2\text{ s}$ , Power= 2 W, second heater. ....	110
Fig. 57. $T_{in}= 21^{\circ}\text{C}$ , $G=125\text{ kg/m}^2\text{ s}$ , Power= 2 W, second heater. ....	111
Fig. 58. $T_{in}= 21^{\circ}\text{C}$ , $G=70\text{ kg/m}^2\text{ s}$ , Power= 4 W, second heater. ....	111
Fig. 59. Image resulting from the processing of the V1100vg120 video. ....	128
Fig. 60. Image resulting from the processing of the V1100vg120 video. ....	128
Fig. 61. Image resulting from the superposition of the original image and the processed image of the V1100vg120 video. ....	129
Fig. 62. Image resulting from the superposition of the original image and the processed image of the V1120vg80 video. ....	129

Fig. 63. Image resulting from the superposition of the original image and the processed image of the V1140vg80 video. ....	130
Fig. 64. Image resulting from the superposition of the original image and the processed image of the V1160vg80 video. ....	130

## LIST OF TABLES

Tab. 1. Comparison between nominal and real heat flux for a 40 mm long heater with different value of power provided. ....	77
Tab. 2. Complete range of videos analysed.....	122

## NOMENCLATURE

$T_{\text{sat}}$ : saturation temperature of the fluid, [ $^{\circ}\text{C}$ ]  
 $T$ : temperature, [ $^{\circ}\text{C}$ ]  
 $T_{\text{ref}}$ : reference temperature, [ $^{\circ}\text{C}$ ]  
 $G$ : mass flux, [ $\text{kg}/\text{m}^2 \text{ s}$ ]  
 $L$ : length of the channel, [m]  
 $D$ : internal diameter of the channel, [m]  
 $D_h$ : hydraulic diameter, [m]  
 $D_{\text{in}}$ : internal diameter of the channel, [m]  
 $D_{\text{ext}}$ : external diameter of the channel, [m]  
 $h$ : enthalpy, [ $\text{J}/\text{kg K}$ ]  
 $h_{LV}$ : latent heat of vaporization, [ $\text{J}/\text{kg K}$ ]  
 $h(z)$ : enthalpy at a cross section  $z$ , [ $\text{J}/\text{kg K}$ ]  
 $h_{\text{in}}$ : enthalpy of the fluid at the inlet, [ $\text{J}/\text{kg k}$ ]  
 $q'(z)$ : heat input from unit of length, [ $\text{J}/\text{m}^2$ ]  
 $\dot{M}$ : mass flow rate, [ $\text{kg}/\text{s}$ ]  
 $x$ : vapour quality  
 $A$ : area, [ $\text{m}^2$ ]  
 $\dot{Q}$ : volumetric flow rate, [ $\text{m}^3/\text{s}$ ]  
 $u$ : velocity of the phases, [ $\text{m}/\text{s}$ ]  
 $\epsilon$ : void fraction  
 $j$ : superficial velocity, [ $\text{m}/\text{s}$ ]  
 $\rho$ : density, [ $\text{kg}/\text{m}^3$ ]  
 $j$ : total superficial velocity, [ $\text{m}/\text{s}$ ]  
 $V_j$ : drift velocity of the vapour phase, [ $\text{m}/\text{s}$ ]  
 $j_j$ : drift flux, [ $\text{m}/\text{s}$ ]  
 $Re$ : Reynolds number  
 $P$ : wetted perimeter, [m]  
 $\mu$ : dynamic viscosity, [ $\text{Pa s}$ ]  
 $We$ : Weber number  
 $\sigma$ : surface tension, [ $\text{N}/\text{m}$ ]  
 $Bo$ : Bond number  
 $X_{tt}$ : Martinelli parameter  
 $f$ : friction factor  
 $W$ : circumference of the tube, [m]  
 $t$ : thickness of the ITO coating, [ $\mu\text{m}$ ]  
 $V_{\text{ITO}}$ : voltage, [V]  
 $P_{\text{ITO}}$ : heating power, [W]

$I_{ITO}$ : electrical current intensity, [A]

$R$ : electrical resistance, [ $\Omega$ ]

$Nu$ : Nusselt number

$Ra$ : Rayleigh number

$Pr$ : Prandtl number

$Q$ : power entering the test section, [W]

$P_{tot}(z)$ : the total electrical power provided by the heaters till the axial position  $z$ , [W]

$\dot{m}_{ref}$ : refrigerant mass flow rate, [kg/s]

$\epsilon_{HOM}$ : homogeneous void fraction

$L_{ITO}$ : ITO coating length, [mm]

$q$ : heat flux, [W/m<sup>2</sup>]

$x(z)$ : vapour quality at the  $z$  axial position

$g$ : acceleration of gravity, [m/s<sup>2</sup>]

$R$ : mean radius of one bubble, [m]

$\beta$ :  $R_{max}/R_{min}$  of each bubble

$\tau$ : shape parameter for the bubble

$N$ : total number of bubbles in one video

$\sigma^2$ : variance of the measure

$\sigma_M$ : standard error of the mean

## Subscripts

'<sub>L</sub>': liquid phase

'<sub>v</sub>': vapor phase

# 1. INTRODUCTION AND MAIN OBJECTIVES

Increased calculation processing speed, miniaturization and higher packing densities of electronic processing chips has lead to the development of high power, high heat flux electronics cards used by the telecommunications and server industries to process digital signals. The drive towards higher system performance has put a large demand on forced air convection cooling techniques and is heading towards the thermal limit of the technology.

Thermal management is becoming the limiting factor in the development of higher power electronic devices. To meet future heat transfer demands, innovative methods of thermally managing electronic devices are required. Within the telecom and server industries, increased performance of electronic units is achieved by the implementation of advanced silicon and optical chips with faster processing speed. In 1965, Moore stated that “The complexity for minimum component costs has increased at a rate of roughly a factor of two per year” and predicted that the number of transistors per chip would continue to double every two years. This is known as Moore’s Law and has resulted in an increase from 1000 transistors per chip in 1970 to 42million transistors per chip for Intel Pentium 4 devices in 2000 and 410 million transistors per chip on the Intel Itanium 2 processor. As Moore’s law proved itself to be true, the heat generated per chip was for example in 1988 for the Intel 386 processor a power of 1W, and this increased to approximately 100W for modern chips, for example from Intel (4), the SL7AA Pentium® 4 processor Extreme Edition has an operating power of 92.1W and temperature of 64°C. Higher packing densities of components on printed circuit boards (PCBs) and of PCBs in racking systems have occurred to reduce system costs. This has created the need for higher heat dissipation for individual cards and entire rack systems. Chip miniaturization reduces the heat transfer surface area and with increased power, very high heat fluxes are induced. Therefore to maintain the chips within operating conditions a greater demand is put onto the heat transfer system.

In such scenario, researches on refrigerant two-phase flows are fundamental to improve the efficiency of the systems mentioned before. Refrigerants two-phase flows are present in many industrial applications and present various and complex regimes, which depends on the mass flow rate, the channel geometries, the heat exchange.

To design novel cooling systems based on refrigerant flows, the standard empirical correlations for condensers and evaporators are not enough accurate, since the channel diameters are reduced to fit in the downsizing of the electronical components. Therefore since few years the researcher are trying to investigate the various refrigerant regimes in small, mini and micro, channels in order to determine the fluid mechanical regimes, the heat transfer convection coefficients and the pressure losses.

The problem appears to be complicated by the fact that many of the standard measurement techniques are not anymore adequate with the small dimension of the tubes and the channels.

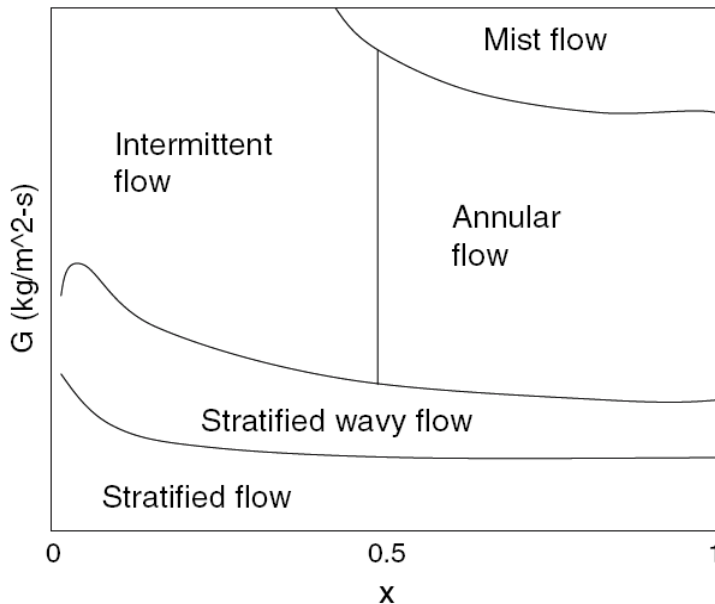
As heat exchangers became smaller, the information of the flow mechanism of a gas-liquid two-phase mixture flowing concurrently in a narrow channel was increasingly requested to improve the performance of the compact heat exchangers. For this reason void fraction, flow pattern and pressure losses are all important parameters to be investigated in two-phase flow experiments.

The fundamental knowledge such as flow pattern, void fraction and pressure loss are all important parameters for designing a heat exchanger.

In recent years, a number of researchers have carried out experiments on flow boiling heat transfer in mini-size tubes and channels.

Flow regime maps developed from flow visualization observations are commonly used or developed in the literature such as Wojtan et al.[33], Garimella et al.[29], Thome et al.[28], Didi et al.[17], Zurcher et al.[18], Mandhane et al.[6], and Baker [2] to aid in the modelling of two-phase flow.

The three main types of two-phase flow regime maps appearing in the literature Baker/Mandhane, Taitel-Dukler [8], and the most commonly used Steiner [10] type, depict boundaries between flow regimes that are not easily represented by continuous functions. This is evident from Fig. 1, which contains a depiction of a typical Steiner type flow map.



**Fig. 1. Steiner flow pattern map**

Recently, efforts have been made in the literature to develop flow regime maps in a more quantitative manner than manual classification.

Probabilistic two-phase flow regime map data first obtained by Nino[20] for refrigerant and air–water flow in multi-port microchannels is found by Jassim and Newell to eliminate the discontinuities created by traditional flow maps. Probabilistic two phase flow regime maps have quality on the horizontal axis and the fraction of time in which a particular flow regime is observed in a series of pictures taken at given flow condition on the y axis.

Jassim and Newell developed curve fit functions to represent Nino's 6-port microchannel time fraction data that are continuous for the entire quality range with correct physical limits. Jassim and Newell then utilized the probabilistic flow regime map time fraction curve fits to predict pressure drop and void fraction.

The difficulty with the probabilistic flow map based modelling technique is that large numbers of pictures must be classified for each flow condition in order to create a large amount of data necessary to generalize the time fraction functions with respect to refrigerant properties and flow conditions. Consequently, an automated image recognition technique is needed to achieve an objective classification.

In this work the novel experimental test rig allows to visually investigate the two-phase flow also in the diabatic zone of the test section and not just in the adiabatic. To obtain such results Indium Tin Oxide (ITO) coatings are used as electrical heaters.

ITO thin film has attracted interest because of its characteristics of high optical transmittance over the visible wavelength region, and excellent adhesion to glass substrates.

The main measurement tool will be the high-speed flow visualisation, which is needed to create the flow pattern maps.

This technique will allow identifying with high accuracy the boiling process even at the microscale level. It will be possible to observe several phenomena, such as bubble formation, bubble coalescence and growth till the annular flow and the total vaporisation with the establishment of dryout.

From this point of view, the present project will be likely the first to perform the experimental analysis of refrigerants boiling phenomena in horizontal minichannel heated with a transparent coating system and visualized with a high speed camera.

The main objectives of the present work are:

- develop a new experimental test rig and use an avant-garde technique to study R134a flow boiling inside mini and micro-channels;
- apply an optical measurement technique to visually characterize the flow patterns and obtain objective results;

- create a new classification technique based on the statistical variation of several geometrical characteristics of the bubbles: diameter, 2D void fraction and bubble shape;
- statistically study the transition lines in the flow pattern maps and improve their understanding;
- visually analyse the phenomena and mechanisms governing the boiling process, such as bubble nucleation, bubble growth, departure and bubble lift-off;
- study the evolution of the geometrical features of the bubbles along the glass tube to have a better understanding of the coalescence rate governing this phenomena;
- create the basis to better predict heat transfer coefficients in microcooling elements and heat spreaders for electronic cooling

### **1.1. Summary of the thesis**

A brief description of the contents of the chapters that follow is given below:

Chapter 1: introduction.

Chapter 2: presents the fundamentals of two phase flow with the main parameters and definition described.

Chapter 3: reviews the state of the art. The first topic is flow pattern maps, the second is void fraction and the last is the description of the common experimentation setup.

Chapter 4: presents a description of the new experimental facility with a detailed description of the innovative test section.

Chapter 5: shows the heat fluxes behaviour inside the test section and present a numerical simulation of one heater and its boundaries.

Chapter 6: describes the data acquisition devices and presents an accurate error analysis of each measure.

Chapter 7: presents the image processing technique and the basic concepts of the automatic flow pattern identification

Chapter 8: describes the two set of experiments performed.

Chapter 9: shows the results of the automatic flow pattern identification technique.

Chapter 10: presents the general conclusions.

Chapter 11: presents the latest results and the future work that was begun at the end of the thesis.

## 2. FUNDAMENTAL DEFINITION AND FLOW PARAMETERS

This chapter introduces the primary variables used throughout this work and derives some simple relationships between them for the case of one-dimensional two-phase flow. To distinguish between vapor and liquid the subscripts 'L' for liquid and 'v' for vapor will be used.

### 2.1. Two-phase flow

Classical thermodynamics tells us that a phase is a macroscopic state of the matter which is homogeneous in chemical composition and physical structure; e.g., a gas, a liquid or solid of a pure component. Two phase flow is the simplest case of multiphase flow, in which two phases are present for a pure component.

In internal convective vaporization and condensation processes, the vapor and liquid are in simultaneous motion inside the flow, channel. The resulting two-phase flow is generally much more complicated physically than single-phase flow. In addition to the usual inertia, viscous, and pressure forces present in single-phase flow, two-phase flows are also affected by interfacial tension forces, the wetting characteristics of the liquid on the tube wall, and the exchange of momentum between the liquid and vapor phases in the flow.

### 2.2. Vapor quality

The vapor quality ( $x$ ) is defined to be the ratio of the vapor mass flow rate ( $\dot{M}_v$  [kg/s]) divided by the total mass flow rate ( $\dot{M}_v + \dot{M}_L$ ):

$$x = \frac{h(z) - h_L}{h_{LV}} \quad (2.1)$$

When phase change does not take place in a channel, one needs to measure the mass flow rate of each phase, and the quality is then determined for the entire channel. In case there is a phase change in the channel, e.g. if the channel is heated and boiling takes place, then the quality will increase (inverse for condensation) in the direction of flow.

If there is not thermal equilibrium between the phases, one cannot calculate the quality merely by knowing the inlet quality and the heat flux from the wall. Unfortunately, it is

very difficult to measure or calculate with precision the quality of the liquid-vapor mixture flowing in a channel where a change of phase takes place.

A fictitious quality, the so called thermodynamic equilibrium quality can be calculated by assuming that both phases are saturated, i.e. that their temperatures are equal to the saturation temperature corresponding to their common pressure. The so-called thermodynamic equilibrium quality can be calculated as:

$$x = \frac{h(z) - h_L}{h_{LV}} \quad (2.2)$$

where  $h_L$  [J/kg] is the enthalpy of the saturated liquid,  $h_{LV}$  [J/kg] is the latent heat of vaporization, and  $h(z)$  [J /kg] is the enthalpy at a cross section  $z$ , which can be calculated from:

$$h(z) = h_{in} + \frac{1}{\dot{M}} \int_0^z q'(z) dz \quad (2.3)$$

where  $h_{in}$  is the enthalpy of the fluid at the inlet and  $q'(z)$  [W/m] is the heat input from unit of length.

## 2.1. Mass Flux

The mass flux ( $G$ ) is defined to be the ratio of the mass flow rate ( $\dot{M}$ ) divided by the cross-sectional area:

$$G = \frac{\dot{M}}{A} \quad (2.4)$$

Considering the continuity law, the mass flux is the expression of the mean flow velocity multiplied by the mean density. The usual unit of the mass flux is [kg/m<sup>2</sup>s].

## 2.3. Velocities

In two-phase flow there are a number of velocities which can be defined. Also, in general, the phases will not have the same velocity and there will be a relative velocity between them.

### 2.3.1. True average velocities

The true average velocities of the phases  $u_V$  and  $u_L$  are the velocities by which the phases actually travel. The cross sectional average true velocities are determined by the volumetric flow rates  $\dot{Q}_V$  and  $\dot{Q}_L$  [ $\text{m}^3/\text{s}$ ] divided by the cross-sectional areas occupied by each phase:

$$u_V = \frac{\dot{Q}_V}{A_V} = \frac{\dot{Q}_V}{\varepsilon A} \quad (2.5)$$

$$u_L = \frac{\dot{Q}_L}{A_L} = \frac{\dot{Q}_L}{(1-\varepsilon)A} \quad (2.6)$$

where  $\varepsilon$  is the ratio between the cross-sectional area occupied by the vapour and the whole cross section.

From the equation of continuity it is possible to define liquid and vapor true means velocities in a channel as follows:

$$u_V = \frac{x}{\varepsilon} \frac{\dot{M}}{\rho_V A} = \frac{G}{\rho_V} \frac{x}{\varepsilon} \quad (2.7)$$

$$u_L = \frac{1-x}{1-\varepsilon} \frac{\dot{M}}{\rho_L A} = \frac{G}{\rho_L} \frac{1-x}{1-\varepsilon} \quad (2.8)$$

### 2.3.2. Superficial velocities

The superficial velocities (also called volumetric fluxes) of the phases  $j_V$  and  $j_L$  are defined as the ratio of the volumetric flow rate of the phase considered over the total cross-sectional area of the two-phase flow. It might also be expressed as the phase velocity if it would flow alone in the entire cross section.

$$j_V = \frac{\dot{Q}_V}{A} = \frac{G}{\rho_V} x = \varepsilon u_V \quad (2.9)$$

$$j_L = \frac{\dot{Q}_L}{A_L} = \frac{G}{\rho_L}(1-x) = (1-\varepsilon)u_L \quad (2.10)$$

The total superficial velocity is defined as:

$$j = j_V + j_L \quad (2.11)$$

### 2.3.3. Drift velocities

The drift velocities of the phases  $V_{Vj}$  and  $V_{Lj}$  are defined as the true average velocity of the phase in relation to the total superficial velocity, namely:

$$V_{Vj} = u_V - j \quad (2.12)$$

$$V_{Lj} = u_L - j \quad (2.13)$$

The drift fluxes of the phases  $j_{Vj}$  and  $j_{Lj}$  are defined as follows:

$$j_{Vj} = \varepsilon V_{Vj} = \varepsilon(u_V - j) \quad (2.14)$$

$$j_{Lj} = (1-\varepsilon)V_{Lj} = (1-\varepsilon)(u_L - j) \quad (2.15)$$

It follows, from Eqs. (2.14), (2.15) and (2.11) that:

$$j_{Vj} + j_{Lj} = 0 \quad (2.16)$$

## 2.4. Void Fraction

In two-phase flow, void fraction is one of the most important parameters to be defined. It defines the cross-sectional area occupied by the gas or vapor phase respect to the total.

As it determines the true average velocities of the liquid and the vapor, it represents a fundamental parameter in the calculation of pressure drop, flow pattern transitions and heat transfer coefficients.

Cross sectional void fraction is defined as:

$$\varepsilon = \frac{A_v}{A_v + A_L} \quad (2.17)$$

where  $A_v$  is the sum of areas occupied by vapor and  $A_L$  is the sum of areas occupied by liquid.

In two-phase flow, the superficial velocity is used to calculate the cross-sectional void fraction as written in Eq. (2.18).

$$\varepsilon = \frac{j_v}{u_v} \quad (2.18)$$

The time average centreline void fraction, on the other hand, is calculated by assuming that its value is 1 if there is vapor and 0 if liquid. It does not take into account the radial distribution of the liquid and vapor but only that at the nose and rear of the bubble, i.e. essentially which at the centreline of the channel, in a slug flow.

The measurable values of the parameters are the fluid flow rate, i.e. the mass flow  $G$ , for the given thermodynamical properties, the vapour and liquid density,  $\rho_v$ ,  $\rho_L$  and, if there is an accurate estimation of the latent heat of vaporization and the heat flux convected to the fluid, the vapour quality  $x$ . Therefore from the equation (2.18) is possible to estimate the cross sectional void fraction and then to compare the estimation with the data obtained with the image analysis.

## 2.5. Definition of non-dimensional numbers

The principal non-dimensional numbers used in the present study are defined below.

### 2.5.1. Reynolds number

The Reynolds number represents the ratio of the inertial forces to the viscous forces. For the particular case of forced convection inside a tubular channel, the liquid Reynolds number can be expressed in the following form:

$$Re_L = \frac{\rho_L u_L D_h}{\mu_L} \quad (2.19)$$

where  $D_h$  is the hydraulic diameter defined as the ratio of the cross-sectional area of the fluid  $A$  to the wetted perimeter  $P_L$ :

$$D_h = \frac{4A_L}{P_L} \quad (2.20)$$

In the case of circular tubes,  $D_h = D$ .  
Considering one-dimensional flow and using the definition of the true average velocity from Eq. (2.6), the liquid Reynolds number can be expressed as:

$$Re_L = \frac{GD_h}{\mu_L} \frac{1-x}{1-\varepsilon} \quad (2.21)$$

where the  $D_h$  for the liquid phase is expressed in the following form:

$$D_h = \frac{4A_L}{P_L} = \frac{4(1-\varepsilon)A}{P_L} \quad (2.22)$$

Substituting Eq. (2.22) into (2.21) the liquid Reynolds number is defined as:

$$Re_L = \frac{4G(1-x)A}{\mu_L P_L} \quad (2.23)$$

The same approach will be used for the vapor Reynolds number which is defined as:

$$Re_V = \frac{GD_h}{\mu_V} \frac{x}{\varepsilon} \quad (2.24)$$

where the  $D_h$  for the vapor phase is expressed as:

$$D_h = \frac{4A_V}{P_V} = \frac{4A\varepsilon}{P_V} \quad (2.25)$$

Finally, substituting Eq. (2.25) into (2.24), the vapor Reynolds number is expressed as:

$$Re_V = \frac{4GxA}{\mu_V P_V} \quad (2.26)$$

In the literature other definitions of the Reynolds number may be found. As the void fraction is difficult to determine, the following expressions are also used for circular tubes:

$$Re_L = \frac{G(1-x)D}{\mu_L} \quad (2.27)$$

$$Re_V = \frac{GxD}{\mu_V} \quad (2.28)$$

From the measurement point of view only a technique able to estimate the wetted perimeter  $P_L$  could be hence useful to define the values of the two-phase Reynolds numbers.

In that situation, each phase flows alone in the complete cross-section of the tube at its own velocity. Another type of Reynolds number may be calculated:

$$Re_{LO} = \frac{GD}{\mu_L} \quad (2.29)$$

$$Re_{VO} = \frac{GD}{\mu_V} \quad (2.30)$$

It represents the liquid or the vapor phase only flowing alone in the complete cross-section of the tube at the total mass flux. Prediction methods for two-phase frictional pressure drops use one set of these Reynolds number definitions and one must be careful to use the definition used in the particular method.

### 2.5.2. Weber number

The liquid Weber number expresses the ratio of inertia to surface tension forces. The reference length is the tube diameter:

$$We_L = \frac{\rho_L \mu_L^2 D}{\sigma} \quad (2.31)$$

Usually, in two-phase flow experiments, the liquid Weber number is expressed as:

$$We_L = \frac{G^2 D(1-x)}{\rho_L \sigma} \quad (2.32)$$

or

$$We_{LO} = \frac{G^2 D}{\rho_L \sigma} \quad (2.33)$$

for when the liquid phase only flows alone in the complete cross-section of the tube at the total mass flux.

For the vapor, the same type of definitions is obtained:

$$We_V = \frac{G^2 D x}{\rho_V \sigma} \quad (2.34)$$

or

$$We_{VO} = \frac{G^2 D}{\rho_V \sigma} \quad (2.35)$$

### 2.5.3. Boiling number

The Boiling number expresses the ratio between the global heat flux  $q$  and the potential heat flux that would have been applied for complete evaporation:

$$Bo = \frac{q}{h_{LV} G} \quad (2.36)$$

### 2.5.4. Bond number

The (liquid) Bond number, notated Bo, is a dimensionless number expressing the ratio of body forces (often gravitational) to surface tension forces:

$$Bo = \frac{\rho g D}{\sigma}$$

The Bond number is a measure of the importance of surface tension forces compared to body forces. A high Bond number indicates that the system is relatively unaffected by surface tension effects; a low number (typically less than one is the requirement) indicates that surface tension dominates. Intermediate numbers indicate a non-trivial balance between the two effects. Notice that for the HFC134a the Bond values are always much greater than 10 (Bo=3700 for the present experiment) and only for nanotubes ( $D_i < 1\mu\text{m}$ ) the surface tension effect may play an important role.

### 2.5.5. Martinelli parameter

The Martinelli parameter is the ratio of the theoretical frictional pressure drop that would occur if each phase could flow separately in the complete cross-section of the channel with the original rate of each phase. In general form the Martinelli parameter is calculated as:

$$X_{tt} = \frac{\left[ \left( \frac{dP}{dz} \right)_L \right]^{0.5}}{\left[ \left( \frac{dP}{dz} \right)_V \right]} \quad (2.37)$$

where

$$\left( \frac{dP}{dz} \right)_L = f_L \frac{2G^2}{D\rho_L} (1-x)^2 \quad (2.38)$$

$$\left( \frac{dP}{dz} \right)_V = f_V \frac{2G^2}{D\rho_V} x^2 \quad (2.39)$$

with  $f_L$ , the fiction factor for the liquid expressed by:

$$\begin{aligned} f_L &= \frac{16}{Re_L} \text{ for } Re_L < 2000 \\ f_L &= 0.079 Re_L^{-0.25} \text{ for } Re_L > 2000 \end{aligned} \quad (2.40)$$

With  $Re_L$  from Eq. (2.27),

and  $f_V$ , the fiction factor for the vapor expressed by:

$$\begin{aligned} f_V &= \frac{16}{Re_V} \text{ for } Re_V < 2000 \\ f_V &= 0.079 Re_V^{-0.25} \text{ for } Re_V > 2000 \end{aligned} \quad (2.41)$$

With  $Re_V$  from Eq. (2.28).

$X_{tt}$  can be also defined as a measure of the degree to which the two-phase mixture is closer to flowing as a liquid ( $X_{tt} \gg 1$ ) or as a gas ( $X_{tt} \ll 1$ ).

### 3. STATE OF THE ART REVIEW

#### 3.1. Flow patterns in conventional channels

For two-phase flows, the respective distribution of the liquid and vapor phases in the flow channel is an important aspect of their description. Their respective distributions take on some commonly observed flow structures, which are defined as two-phase flow patterns that have particular identifying characteristics. Heat transfer coefficients and pressure drops are closely related to the local two-phase flow structure of the fluid, and thus two-phase flow pattern prediction is an important aspect of modelling evaporation and condensation. In fact, recent heat transfer models for predicting in tube boiling and condensation are based on the local flow pattern and hence, by necessity, require reliable flow pattern maps to identify what type of flow pattern exists at the local flow conditions. Analogous to predicting the transition from laminar to turbulent flow in single-phase flows, two-phase flow pattern maps are used for predicting the transition from one type of two-phase flow pattern to another.

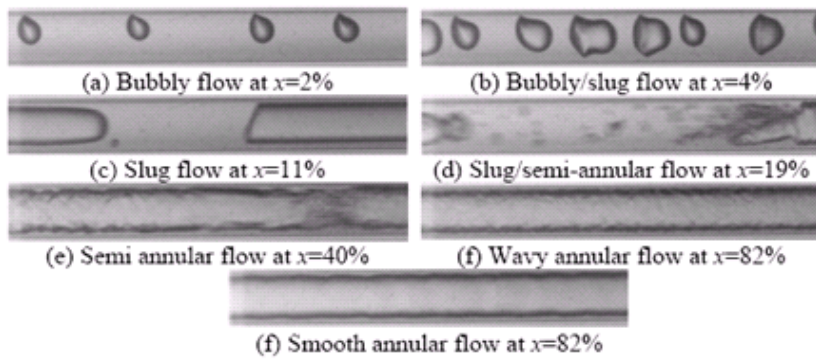


Fig. 2. Flow observation for R134a,  $D=0.5$  mm,  $L=70.7$  mm,  $G=500$  kg/m<sup>2</sup> s

#### 3.2. Flow Patterns in Horizontal Tubes

Two-phase flow patterns in horizontal tubes are similar to those in vertical flows but the distribution of the liquid is influenced by gravity that acts to stratify the liquid to the bottom of the tube and the gas to the top. Flow patterns for co-current flow of gas and liquid in a horizontal tube are shown in Fig. 2 and are categorized as follows:

- *Bubbly flow*. The gas bubbles are dispersed in the liquid with a high concentration of bubbles in the upper half of the tube due to their buoyancy. When shear forces

are dominant, the bubbles tend to disperse uniformly in the tube. In horizontal flows, the regime typically only occurs at high mass flow rates.

- *Stratified flow.* At low liquid and gas velocities, complete separation of the two phases occurs. The gas goes to the top and the liquid to the bottom of the tube, separated by an undisturbed horizontal interface. Hence the liquid and gas are fully stratified in this regime.
- *Stratified-wavy flow.* Increasing the gas velocity in a stratified flow, waves are formed on the interface and travel in the direction of flow. The amplitude of the waves is notable and depends on the relative velocity of the two phases; however, their crests do not reach the top of the tube. The waves climb up the sides of the tube, leaving thin films of liquid on the wall after the passage of the wave.
- *Intermittent flow.* Further increasing the gas velocity, these interfacial waves become large enough to wash the top of the tube. This regime is characterized by large amplitude waves intermittently washing the top of the tube with smaller amplitude waves in between. Large amplitude waves often contain entrained bubbles. The top wall is nearly continuously wetted by the large amplitude waves and the thin liquid films left behind. Intermittent flow is also a composite of the plug and slug flow regimes. These subcategories are characterized as follows:
  - *Plug flow.* This flow regime has liquid plugs that are separated by elongated gas bubbles. The diameters of the elongated bubbles are smaller than the tube such that the liquid phase is continuous along the bottom of the tube below the elongated bubbles. Plug flow is also sometimes referred to as *elongated bubble flow*.
  - *Slug flow.* At higher gas velocities, the diameters of elongated bubbles become similar in size to the channel height. The liquid slugs separating such elongated bubbles can also be described as large amplitude waves.
- *Annular flow.* At even larger gas flow rates, the liquid forms a continuous annular film around the perimeter of the tube, similar to that in vertical flow but the liquid film is thicker at the bottom than the top. The interface between the liquid annulus and the vapor core is disturbed by small amplitude waves and droplets may be dispersed in the gas core. At high gas fractions, the top of the tube with its thinner film becomes dry first, so that the annular film covers only part of the tube perimeter and thus this is then classified as stratified-wavy flow.
- *Mist flow.* Similar to vertical flow, at very high gas velocities, all the liquid may be stripped from the wall and entrained as small droplets in the now continuous gas phase.

### 3.2.1. The study of Kattan, Thome, Favrat [15]

As a first step in this direction, Kattan et al. [15] proposed a modification of the Steiner map, which in turn is a modified Taitel–Dukler map, and which includes a method for

predicting the onset of dryout at the top of the tube in diabatic annular flow. This map is presented in coordinates mass velocity versus vapor quality ( $G$  vs.  $x$ ) that facilitates observation of the evolution of flow pattern transitions at fixed mass velocities with increasing vapor quality along an evaporator tube.

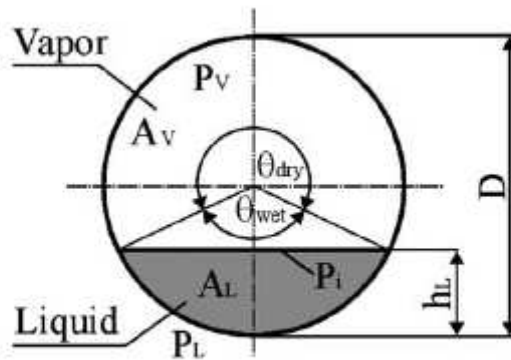
To calculate flow pattern transition curves using their method, the following six dimensionless geometrical variables must first be defined:

$$h_{LD} = \frac{h_L}{D}; \quad P_{LD} = \frac{P_L}{D} \quad (1)$$

$$P_{VD} = \frac{P_V}{D}; \quad P_{iD} = \frac{P_i}{D} \quad (2)$$

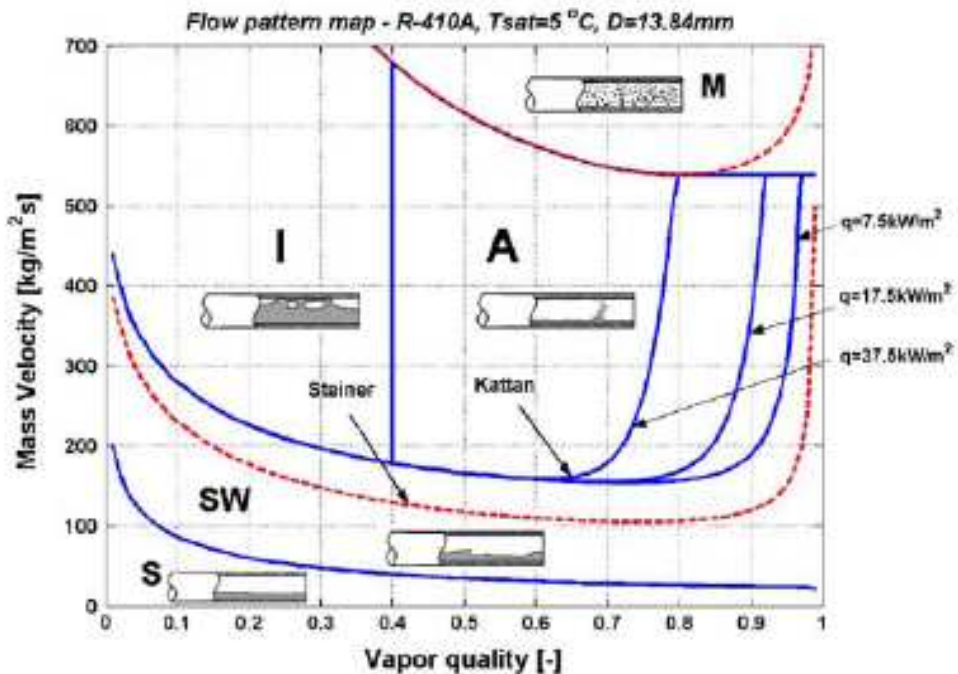
$$A_{LD} = \frac{A_L}{D^2}; \quad A_{VD} = \frac{A_V}{D^2} \quad (3)$$

As shown in Fig. 3,  $D$  is the internal tube diameter,  $P_L$  is the wetted perimeter and  $P_V$  is the complementary perimeter in contact with vapor. Similarly,  $A_L$  and  $A_V$  are the corresponding cross-sectional areas of the liquid and vapor phases,  $P_i$  is the length of the phase interface and  $h_L$  is the height of the liquid phase from the bottom of the tube. An iterative method is required to find the above dimensionless variables from the geometrical equations presented in [15]. After calculating them, the flow pattern transition curves can be determined for the defined properties of the fluid. The transition between stratified and stratified–wavy flow will be here designated as “S–SW”, between stratified–wavy and intermittent/annular flow as “SW–I/A”, between intermittent and annular flow as “I–A”, between annular and mist flow as “A–M”.



**Fig. 3. Stratified two-phase flow cross section.**

Fig. 4 shows the flow pattern map of Kattan compared to Steiner for R-410A at  $T_{\text{sat}} = 5^\circ\text{C}$ . The transition curves “SW–I/A” of Kattan (solid lines) are strongly influenced by the effect of onset of dryout compared to the adiabatic curve of Steiner (dashed line). Based on Kattan’s flow pattern observations, his curve is also raised by  $50 \text{ kg/m}^2\text{s}$ . Regarding the “A–M” transition curve, Kattan added a criterion to avoid the possibility of a mist flow reverting back again to annular flow with increasing vapor quality. Two other transition curves “S–SW” and “I–A” were not modified and are the same as those of Steiner.



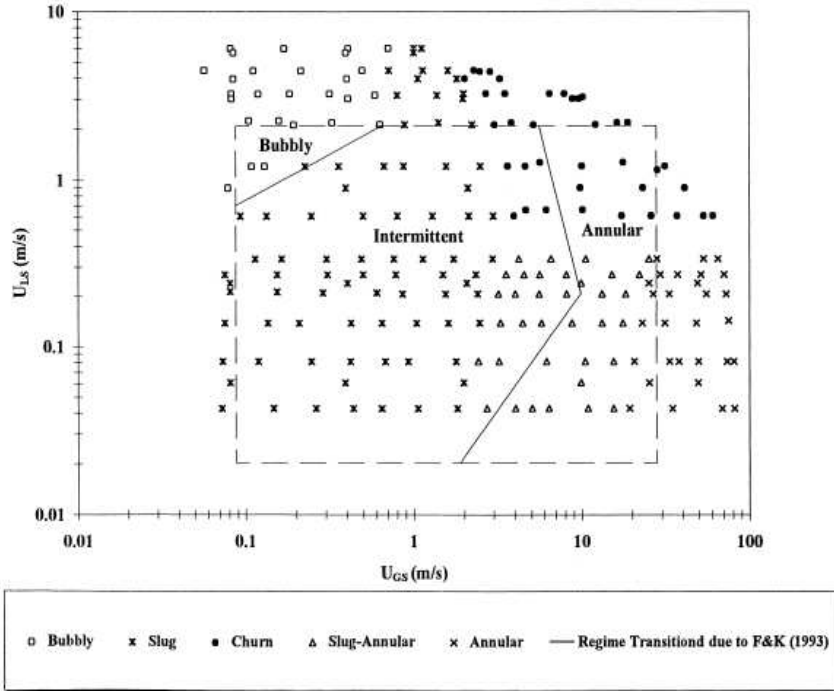
**Fig. 4.** Flow pattern map of Kattan compared to Steiner for R410A at  $T_{\text{sat}} = 5^\circ\text{C}$  in a 13.84 mm internal diameter tube at heat fluxes of 7.5, 17.5 and  $37.5 \text{ kW/m}^2$ .

Kattan verified his flow pattern map for 702 experimental points for five refrigerants tested over a wide range of pressures, vapor qualities and mass velocities representative of direct-expansion evaporator conditions.

These observations showed that 96.2% of the flow pattern data were identified correctly with his diabatic flow pattern map. It must be noted that the “A–M” transition boundary was not investigated experimentally in the work of Kattan.

### 3.2.2. The Triplett, Ghiaasiaan, Abdel- Khalik and Sadowski study [16]

Capillary gas-liquid two-phase flow occurs in increasingly more modern industrial applications. The existing relevant data are limited and are inconsistent with respect to the reported flow patterns and their transition boundaries. A systematic experimental investigation of two-phase flow patterns in microchannels was the objective of this study.



**Fig. 5. Comparison between the experimental flow patterns with the flow patterns of Fukano and Kariyasaki representing their 1 mm-diameter circular test section.**

Using air and water, experiments were conducted in circular microchannels with 1.1 and 1.45 mm inner diameters, and in microchannels with semi-triangular (triangular with one corner smoothed) cross-sections with hydraulic diameters 1.09 and 1.49 mm. The gas and liquid superficial velocity ranges were 0.02-80 and 0.02-8 m/s, respectively. Overall, flow patterns and flow pattern maps using gas and liquid superficial velocities as coordinates, were similar for all the test sections. The discernible flow patterns were bubbly, churn, slug, slug-annular and annular. The obtained data were compared with existing experimental data. They were also compared with relevant flow regime transition models and correlations, generally with poor agreement

As concluding remarks of this study, it can be said that gas-liquid two-phase flow patterns, void fraction and pressure drop in long horizontal microchannels with circular and semi-triangular (triangular with one corner smoothed) cross sections, were experimentally investigated. The test section hydraulic diameters were 1.1 and 1.45 mm for circular channels, and 1.09 and 1.49 mm for semi-triangular cross-section test sections, and the gas and liquid superficial velocity ranges were  $0.02\pm 80$  m/s, and 0.02-8 m/s, respectively.

Five major flow patterns could be distinguished in the experiments as shown in Fig. 5: bubbly, slug, churn, slug-annular and annular. These flow patterns occurred in all test sections and the flow pattern maps using gas and liquid superficial velocities as coordinates were similar overall.

The experimental data were compared with similar data with good overall agreement with the latter two test series and with inconsistencies mainly attributable to confusion in the identification of flow patterns. Available relevant flow regime transition models were compared with data, with poor agreement.

### 3.2.3. The Zürcher, Favrat, Thome study [19]

Based on extensive flow pattern observations for ammonia at 5°C in a 14.0 mm horizontal sight glass tube at the exit of the same diameter of evaporator tube, Zürcher, Favrat and Thome (2002) proposed a new version of the transition boundary curve between annular and intermittent flows to stratified-wavy flow, based on a new equation and on an in-depth analysis of the dissipation effects in a two-phase flow.

### 3.2.4. The Kawahara, Chung, and Kawaji study [21]

An experimental investigation has been carried out on two-phase flow characteristics in a 100  $\mu$ m diameter circular tube. Two-phase flow patterns were determined by video recording the flow in the transparent capillary tube made of fused silica, in which de-ionized water and nitrogen gas were injected at superficial velocities of  $j_G=0.1\text{--}60$  m/s for gas, and  $j_L=0.02\text{--}4$  m/s for liquid. Time-averaged void fraction and two-phase friction pressure drop data were also obtained and analyzed. The flow patterns observed were intermittent and semi-annular flows, but a closer study of the liquid film structure revealed gas core flows with a smooth or ring-shaped film and a serpentine-like gas core surrounded by a deformed liquid film. Bubbly and churn flow patterns were not observed. A flow pattern map was developed based on the probability of appearance of each type of flow, and compared to the existing flow pattern maps obtained for 1mm diameter channels. Void fraction remained low even at high gas flow rates, indicating large slip ratios and weak momentum coupling between the phases. The single-phase friction factor and two-phase friction multiplier data were shown to be in good agreement with the conventional correlations.

As concluding remarks of this study, it can be said that an experimental investigation has been carried out on two-phase flow characteristics in a 100  $\mu\text{m}$  diameter circular tube using de-ionized water and nitrogen gas. Two-phase flow patterns, time-averaged void fraction and two-phase frictional pressure drop data were measured and analyzed. Based on the results presented, the following conclusions can be presented:

(1) The two-phase flow patterns observed were mainly intermittent and semi-annular flows, but a closer study of the liquid film structure revealed gas core flows with a smooth or ring-shaped film and a serpentine-like gas core flow surrounded by a deformed liquid film. Bubbly flow was not observed in the present work, even at the highest superficial liquid velocity ( $j_L = 4 \text{ m/s}$ ) and lowest superficial gas velocity ( $j_G = 0.1 \text{ m/s}$ ) tested.

(2) The probability of appearance of different flow patterns revealed a gradual shift in the predominant flow pattern with increasing gas and liquid flow rates. For low liquid flow rates, gas core flows with a smooth-thin liquid film occurred most frequently at low gas flow rates, but gas core flows with a ring-shaped liquid film became more frequent at high gas flow rates. At high liquid flow rates, gas core flows with a thick liquid film, and serpentine-like gas core flows with a deformed liquid film also appeared. At high gas and liquid flow rates, all types of gas core flows appeared, and this was named a multiple flow pattern.

(3) A flow pattern map was developed based on the probability of appearance of each flow type, and compared to existing flow pattern maps obtained from 1 mm diameter channels. Similarities and differences between the microchannel and larger diameter tubes were identified.

The absence of bubbly and churn flow patterns in the microchannel results was attributed to the low liquid Reynolds numbers and laminar nature of liquid flow in the present microchannel because of the small channel diameter.

(4) Time-averaged void fraction data were obtained from the analysis of two-phase flow images captured at different flow rates. The time-averaged void fraction remained low even at high gas flow rates, indicating significantly larger slip ratios and weaker momentum coupling between the phases, compared to the flows in channels with  $D_H = 1 \text{ mm}$ . This was consistent with the occurrence of predominantly liquid-only or separated flow patterns in the microchannel.

(5) Single-phase friction factor and two-phase friction multiplier data were obtained from the pressure drop data. The single-phase friction factor was shown to be in good agreement with the conventional laminar correlation. The two-phase friction multiplier data were over-predicted by the homogeneous flow model, but correlated well (within  $\pm 10\%$ ) with the separated flow model of Lockhart and Martinelli [1]

### 3.2.5. The work of Zun [22]

Effective progress toward a better understanding of turbulent bubbly flow demands a strategy that comprises several space and time dependent phases of work priorities. The current work focuses upon experimental methods that can be used to collect the information on interfacial structures in bubbly flow and bubble to slug flow transition. Two experimental methods are analyzed in details: probe detection of phase conductivity and visualization. Although different experiments by nature, they utilize a common approach that can be described crudely as a two-part process: first, the scale information is broken into parts, and once the information is analyzed by the discrimination system lower level, it can be reassembled by the system higher level to tell us what is where in the environment. The uncertainty and applicability of phase discrimination are discussed for frozen interfacial structures as well as time-space evolution. In order to identify characteristics that are required by cascade modelling, macro-, meso- and microscales are considered. The assessment is given for 1D, 2D and 3D applications. Several attributes that are needed in spatiotemporal modelling at the reassembling stage are pointed out.

As concluding remarks of this study, it can be said that a general strategy in disassembling and reassembling of the two-phase flow structures is considered. It comprises four steps for disassembling the processes on different scales, among those the first three for structures identification space and time dependent and the fourth for the statistical relevance. The fifth step is considered to reassemble the sequences of events in phenomenological cascade modelling.

Two decades were needed to obtain enough information on void fraction profiles that may differ from wall void peaking to void coring flow regimes which is important in two-fluid modelling (macroscale). The author believes that we are at the beginning of a new era of bubbly flow modelling and simulation in which multiscale reference plays a crucial part. The detailed results of phase discrimination in bubbly flow in a vertical pipe are presented in view of uncertainty and applicability to modelling requirements for the first three steps of the proposed strategy. To identify these characteristics, macro-, meso-, and microscales are considered. The assessment is given for 1D, 2D and 3D applications. Two experimental techniques are chosen as representative: probe detection of phase conductivity and visualization. Pattern decomposition is divided into lower and higher levels. Some novelties of the complex based decision rules that are assorted to the far apart values are presented. Optimization procedure is introduced based on genetic algorithm in combination with man-machine interface. The uncertainty analysis revealed difficulty in obtaining reliable indicators of single bubble shape distortion in mesoscale 2. Very little (almost nothing) is known about bubble clusters, spatial relationship and time-space evolution. No general data on time-space evolution of bubble formation is possible since this phenomenon depends strongly on individual properties of injection mechanism or nucleation sites at micro- and

mesoscales. We are beginning with cascade modelling with a very poor knowledge on initial conditions that are of spatio-temporal character

### 3.2.6. The study of Yu, Lin and Tseng [23]

Flow pattern and heat transfer during evaporation in a 10.7 mm diameter smooth tube and a micro-fin tube are presented. The tubes were tested in the ranges of mass flux between 163 and 408 kg m<sup>-2</sup>s<sup>-1</sup>, and heat flux between 2200 and 56000 W/m<sup>2</sup>. The evaporation temperature was 6°C. Flow maps for both the tubes are plotted in the coordinates of mass flux and vapor quality. The relations of flow pattern and local heat transfer coefficient are discussed. The heat transfer coefficients for intermittent and annular flows in both the smooth tube and the micro-fin tube are shown to agree well with Gungor and Winterton's correlation with modified constants.

As concluding remarks of this study, it can be said that flow pattern and heat transfer of R-134a in horizontal evaporator tubes are investigated experimentally.

Depending on the test conditions, wavy flow, intermittent flow, semi-annular flow and annular flow are observed in the experimental ranges of mass fluxes between 163 and 408 kg m<sup>-2</sup>s<sup>-1</sup>, and heat fluxes between 2200 and 56000 kW m<sup>-2</sup>. Different flow patterns in the tube correspond to different distribution of local heat transfer coefficient around the periphery, and on the other hand the location of flow pattern transition can be identified approximately by the distributions.

With increasing mass flux and quality, flow pattern changes from wavy, intermittent, semi-annular to annular patterns. The transitions of flow pattern occur at lower mass flux and quality in the microfin tube than in the smooth tube, since the surface roughness (spiral groove) can induce more wetted portion and promote annular flow, resulting in better heat transfer. The heat transfer can be enhanced with microfin surface up to 200% at low mass flux and high quality where annular flow dominates in the microfin tube while wavy flow occurs in the smooth tube.

With the average liquid film thickness as the characteristic length in calculating heat transfer coefficients by Gungor and Winterton's correlation, the heat transfer data agree well with the calculated values for intermittent and annular flow patterns, with an average mean deviation of 19% for both the smooth tube and the microfin tube.

### 3.2.7. Flow pattern map of Thome and El Hajal [24]

As a practical option and for consistency between the flow map and heat transfer model, an easier to implement version of the map was proposed by Thome and El Hajal [24]. In the previously presented flow pattern map, dimensionless variables  $A_{LD}$ ,  $A_{VD}$ ,  $h_{LD}$  and  $P_{ID}$  were calculated in an iterative way using the stratified flow void fraction model of Taitel–Dukler [8] illustrated in Fig. 1. On the other hand, the flow boiling heat

transfer model of Kattan et al. [15] uses the Steiner [10] version of the Rouhani–Axelsson drift flux model for horizontal tubes for the cross-sectional void fraction  $\varepsilon$ :

$$\varepsilon = \frac{x}{\rho_V} \left[ (1 + 0.12(1 - x)) \left( \frac{x}{\rho_V} + \frac{1 - x}{\rho_L} \right) + \frac{1.18(1 - x)[g\sigma(\rho_L - \rho_V)]^{0.25}}{G\rho_L^{0.5}} \right]^{-1} \quad (4)$$

This drift flux void fraction model is easy to apply and gives the void fraction as an explicit function of total mass flux, which the method of Taitel–Dukler does not. Hence, it makes sense to use the same void fraction model in both the flow pattern map and heat transfer model, for which the Rouhani–Axelsson model is a better choice as a general method. This was later proven experimentally by making 238 void fraction measurements for R-22 and R-410A in Wojtan et al. [30] in stratified types of flow. Then, from the sectional area of the tube  $A$ , the values  $A_{LD}$  and  $A_{VD}$  are directly determinable as:

$$A_{LD} = \frac{A(1 - \varepsilon)}{D^2} \quad (5)$$

$$A_{VD} = \frac{A\varepsilon}{D^2} \quad (6)$$

The dimensionless liquid height  $h_{LD}$  and the dimensionless length of the liquid interface  $P_{iD}$  can be expressed as a function of stratified angle  $\theta_{strat}$ :

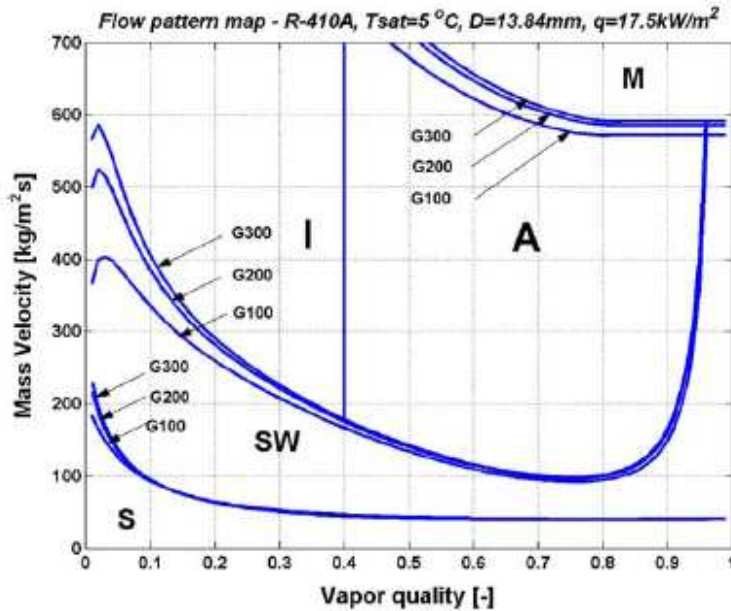
$$h_{LD} = 0.5 \left( 1 - \cos \left( \frac{2\pi - \theta_{strat}}{2} \right) \right) \quad (7)$$

$$P_{iD} = \sin \left( \frac{2\pi - \theta_{strat}}{2} \right) \quad (8)$$

To avoid completely any iteration, the geometrical expression for the stratified angle  $\theta_{strat}$  can be calculated from an approximate expression, evaluated in terms of void fraction, as follows:

$$\theta_{strat} = 2\pi - 2 \left\{ \frac{\pi(1 - \varepsilon) + \left(\frac{3\pi}{2}\right)^{1/3} [1 - 2(1 - \varepsilon) + (1 - \varepsilon)^{1/3} - \varepsilon^{1/3}]}{-\frac{1}{290}(1 - \varepsilon)\varepsilon[1 - 2(1 - \varepsilon)][1 + 4((1 - \varepsilon)^2 + \varepsilon^2)]} \right\} \quad (9)$$

As the void fraction is a function of mass velocity, in the Thome–El Hajal map it influences the position of the transition curves. The minor effect of mass velocity on flow regime transitions is shown in Fig. 6.



**Fig. 6.** Flow pattern map of Thome-El Hajal for R410A at  $T_{\text{sat}}=5^{\circ}\text{C}$  in a 13.84 mm internal diameter tube with its equations evaluated at three fixed mass velocities:  $G=100, 200, 300 \text{ kg/m}^2\text{s}$ .

The strongest effect of mass velocity is observed for the “SW–I/A” transition curve for vapor qualities below 0.1, where the transition curve goes up with increasing mass velocity.

This divergence becomes less significant as the vapor quality increases. The boundary curve “A–M” also moves up marginally with increasing mass velocity.

### 3.2.8. Flow pattern map of Revellin and Thome [31]

Some authors describe microchannel two-phase flow using additional flow pattern designations, such as Tripplet et al. [16] using both rectangular and circular channels. Considering the general research on flow pattern conducted till now, it can be found that the dominant and most common flow pattern are four: Plug flow, Slug flow, Wavy-annular flow and Annular flow. Garimella et al. [29] proposed a correlation for during flow transition condensation of R-134a in circular channels (0.5 to 4.91 mm) with the hydraulic diameter (in mm) as parameter to determine the transition between intermittent and non-intermittent flow as shown in Eq. (1).

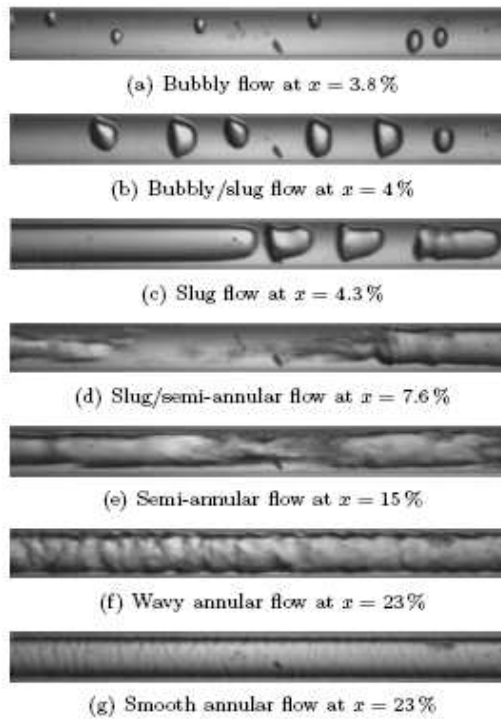
$$x = \frac{a}{G + b} \quad (1)$$

with

$$a = 69.5673 + 22.595 \exp(0.2586 D_1) \quad (2)$$

$$b = -59.9899 + 176.8137 \exp(0.3826 D_1) \quad (3)$$

The difficulty of identifying flow regimes and their transitions comes from the difficulties in obtaining good high speed images, in the interpretation of the flow (subjectivity and pattern definition depending on the author), and also in choosing the channel size that determines either macro or microscale or the transition between them. Thome et al. [33, 34] proposed the first mechanistic heat transfer model to describe evaporation in microchannels with a three-zone flow boiling model that describes the transient variation in the local heat transfer coefficient during sequential and cyclic passage of (i) a liquid slug, (ii) an evaporating elongated bubble and (iii) a vapor slug when film dryout has occurred. The new model illustrates the strong dependency of heat transfer on the bubble frequency, the lengths of the bubbles and liquid slugs and the liquid film thickness and is so far only applicable to the slug flow regime.



**Fig. 7.** Flow patterns and transitions for R245fa,  $D= 0.5\text{mm}$ ,  $L=70.7 \text{ mm}$ ,  $G=500 \text{ kg/m}^2\text{s}$  and  $T_{\text{sat}}=35^\circ\text{C}$ .

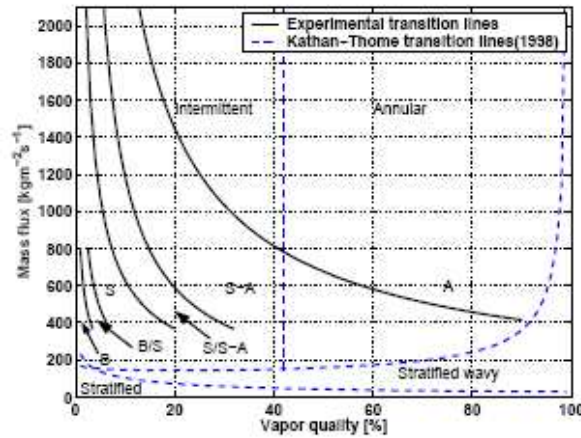
For these reasons, it is opportunistic to apply an optical measurement technique to quantitatively characterize flow pattern transitions and to measure the frequency, velocity and length of vapor bubbles in microchannels, in particular at the exit of microevaporators in which the flows are formed. Such an optical measurement technique has been developed here and implemented in a new multi-purpose microchannel test facility and is presented in this article together with the new results.

As concluding remarks of this study, it can be said that an optical measurement method was used to characterize flow pattern transitions of two-phase flow in micro-tubes. It consists of shining two micro laser beams through a glass tube and the fluid at two different locations, using two lenses to focus the laser beams to the middle of the microtube, and using two photodiodes to recuperate the intensity of the light, whose signals are used to distinguish whether liquid, vapor, or liquid and vapor are present in the cross section. Bubble frequency, lengths of bubbles and flow pattern transitions are parameters that are able to be determined by this technique. Mean vapor velocity is also calculable from the measurements at some test conditions.

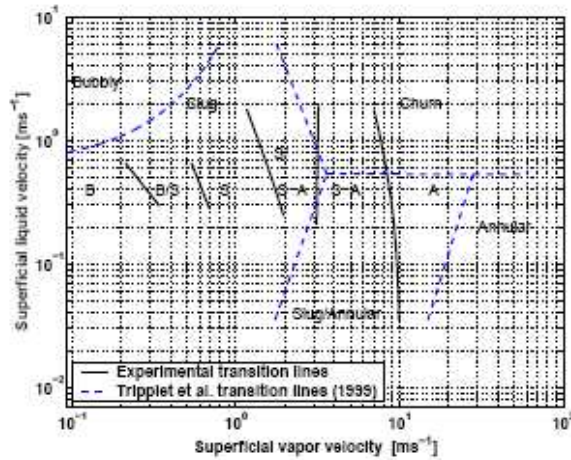
Four principal flow patterns (bubbly flow, slug flow, semi-annular flow and annular flow) with their transitions (bubbly/slug flow and slug/semi-annular flow) were observed in the present experiments with R-134a and R-245fa in 0.50 mm and 0.80 mm circular channels, as shown in Fig. 7.

Many observations have been made on the transitions between flow regimes. The two-phase flow pattern transitions observed with R-134a (Fig. 8) did not compare well to a leading macroscale flow map for refrigerants nor to a microscale map for air-water flows. No significant influence of the inlet subcooling nor the saturation pressure has been observed on the flow pattern transitions. A shorter heated length did not influence the locations of the transition lines.

The diameter effect did not show any difference, although bubbly/slug flow is present over a wider range of mass flux. The transitions between flow regimes are less influenced by the mass flux for R-245fa than for R-134a; however, the two-phase flow transitions for R-245fa are quite similar to those of R-134a.



(a) Comparison between present experimental transition lines from laser 1 and Kattan-Thome-Favrat macroscale map in a mass flux vs. vapor quality format for R-134a,  $D = 0.5$  mm,  $L = 70.70$  mm,  $T_{sat} = 30^\circ\text{C}$ ,  $\Delta T_{sub} = 3^\circ\text{C}$ . (B=Bubbly flow, B/S=Bubbly/slug flow, S=Slug flow, S/S-A=Slug/semi-annular flow, S-A=Semi-annular flow, A=Annular flow)



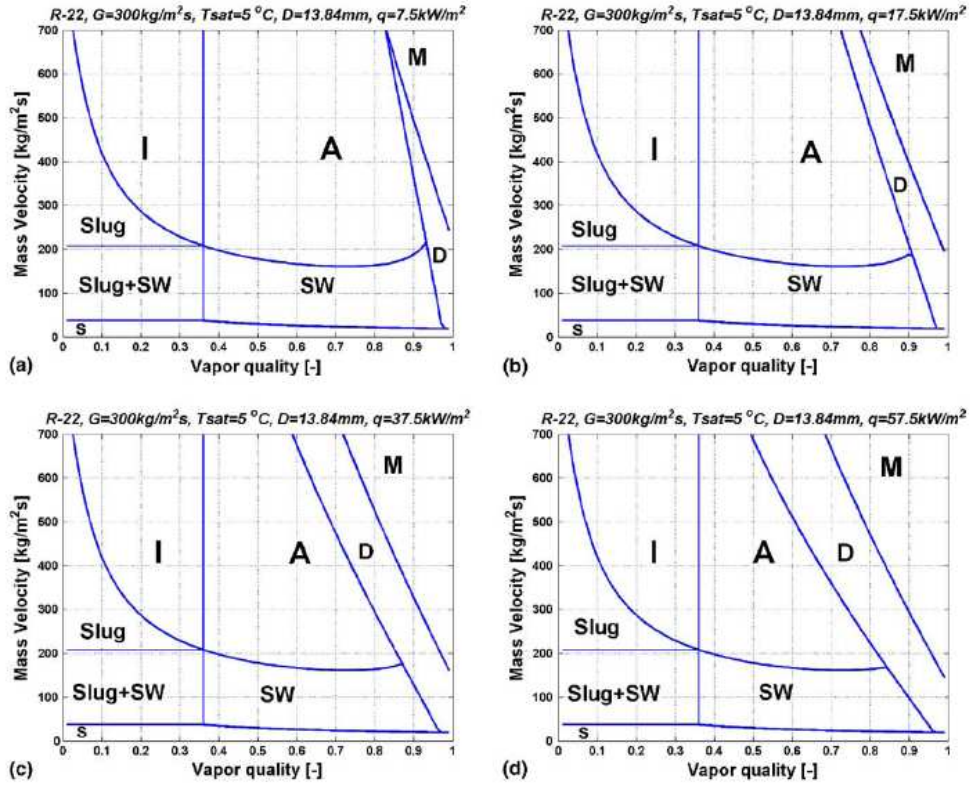
(b) Comparison between present experimental transition lines from laser 1 and Tripplet et al. transition lines available for air-water flow in a 1.097 mm tube diameter.

**Fig. 8. Flow pattern maps with experimental transition lines for R134a,  $D=0.5$  mm,  $L=70.7$  mm,  $T_{sat}=35^\circ\text{C}$ .**

### 3.2.9. The work of Wojtan, Ursenbacher and Thome [33]

Several important modifications to the flow pattern map of Kattan–Thome–Favrat [15] made, resulting in a significantly new version of the map. Based on the dynamic void fraction measurements described in [30], the stratified–wavy region has been subdivided into three subzones: slug, slug/stratified–wavy and stratified–wavy. Furthermore, annular-to-dryout and dryout-to-mist flow transition curves have been

added and integrated into the new flow pattern map, identified by distinct trends of the heat transfer coefficient as a function of vapor quality and by flow pattern observations to determine (and then predict) the inception and completion of dryout in horizontal tubes.



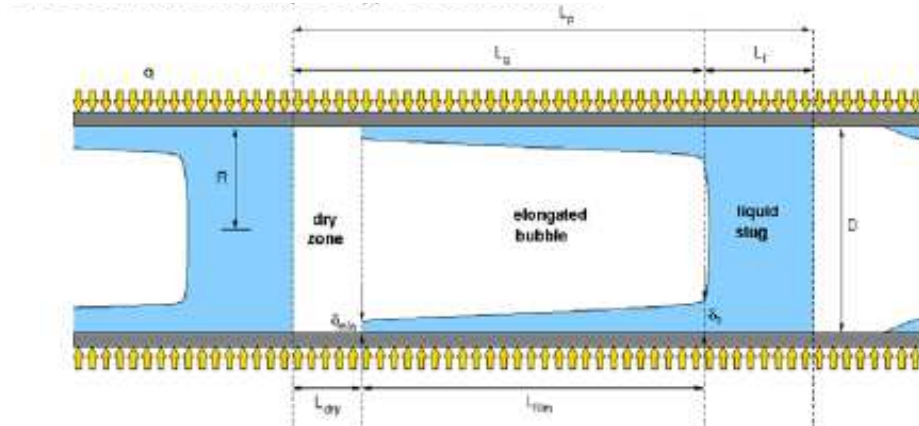
**Fig. 9.** New flow pattern maps for R22 at  $T_{\text{sat}}=5^\circ\text{C}$  and  $D=13.84\text{ mm}$  at  $G=300\text{ kg/m}^2\text{s}$  and four initial heat fluxes: (a)  $7.5\text{ kW/m}^2$ , (b)  $17.5\text{ kW/m}^2$ , (c)  $37.5\text{ kW/m}^2$ , (d)  $57.5\text{ kW/m}^2$ .

New transition curves have been found (Fig. 9) to define annular–dryout and dryout–mist flow transitions based on our new heat transfer measurements and observations. The curves have been integrated into the Thome–El Hajal [28] version of the Kattan–Thome–Favrat flow pattern map. Based on measurements and trends observed in the dynamic void fraction, the stratified–wavy region has been subdivided into three zones: slug, slug/stratified–wavy and stratified–wavy. Furthermore, the transition curve stratified/stratified–wavy flow has been adjusted for vapor qualities below  $x_A$ . These modifications provide a more accurate prediction of the flow regimes below  $G$ -wavy and significantly improve the identification the inception of dryout. All procedures to calculate the new flow pattern map have been presented.

The new flow pattern map does not require any iterative calculations and it can be easily used for flow regime identification in the flow boiling heat transfer model.

### 3.2.10. The study of Revellin and Thome [37]

Flow pattern data and bubble measurements for two small diameter sight glass tubes are used to propose a new type of flow pattern map for evaporating flows in microchannels. Rather than segregating the observations into the traditional flow regimes and an adiabatic map, the new diabatic map classifies flows into three types: (i) the *isolated bubble* regime, where the bubble generation rate is much larger than the bubble coalescence rate and includes both bubbly and slug flows, (ii) the *coalescing bubble* regime, where the bubble coalescence rate is much larger than the bubble generation rate and exists up to the end of the coalescence process and (iii) the *annular* regime, whose extent is limited by the vapor quality at the onset of critical heat flux. This formulation is more useful for phenomenological modelling the processes controlling boiling heat transfer and also visually defines the feasible operating limit of microchannel heat spreaders. The database covers two refrigerants (R-134a and R-245fa) and two channel diameters (0.509 and 0.790 mm). An image of the scheme used for the study is reported in Fig. 10.



**Fig. 10. Schematic of three zone evaporation model.**

The micro-evaporator length was varied from 20 to 70 mm, the inlet subcooling from 2 to 15°C, the mass flux from 200 to 2000 kg/m<sup>2</sup>s and heat fluxes up to 597 kW/m<sup>2</sup>.

Three different saturation temperatures were tested: 26, 30 and 35°C.

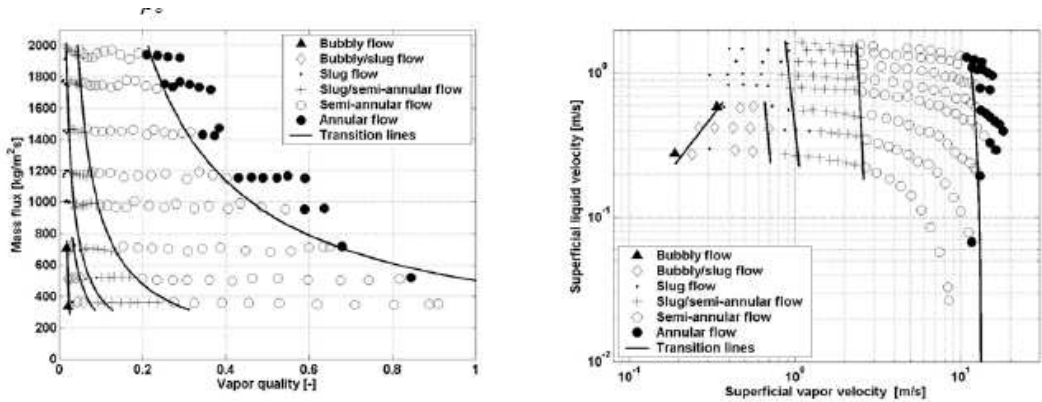
The optical setup consisted of two laser beams, with a power less than 1mW, directed through the glass visualization tube and the fluid inside at two different locations, separated by a distance of 70.63 mm. Two lenses focused the laser beams to the middle of the microtube sight glass and two photodiodes on the opposite side captured the intensity of the light at a scan rate of 10 kHz. The signal processing of the resulting voltage signals from the two diodes to identify the flow patterns and bubble statistics consisted of several steps and is detailed in Revellin [31] and Revellin et al. [39].

Two-phase flow pattern observations based on the above definitions from both laser signals and are presented in Fig. 11 as mass flux versus vapor quality and superficial liquid velocity versus superficial vapor velocity formats, which are calculated from the test results from their definition:

$$J_l = \frac{(1-x)\dot{m}}{\rho_l} \quad (2)$$

$$J_g = \frac{x\dot{m}}{\rho_g} \quad (3)$$

Notably, the higher the mass flux, the earlier annular flow is reached.



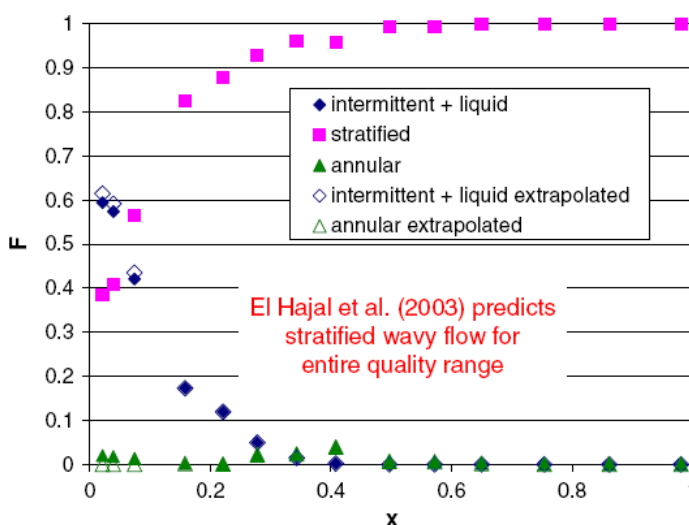
**Fig. 11. Flow pattern maps with experimental transition lines for R134a, D=0.509mm, L=50mm, T<sub>sat</sub>=30°C.**

The observations in annular flow in Fig. 11 (left diagram) do not reached vapor qualities of the onset of the critical heat flux, the latter which were measured separately in the study by Wojtan et al. [33, 34]. Bubbly flow is more or less nonexistent for mass fluxes greater than 1000 kg m<sup>-2</sup>s<sup>-1</sup>. Their transitions are controlled primarily by the rate of coalescence in Revellin et al. [39] which is not recognized as a contributing factor by previous microscale (nor macroscale) flow pattern maps.

### 3.2.11. Probabilistic flow pattern map of Jassim-Newell-Chato [42]

Probabilistic two-phase flow map data (Fig. 12) is experimentally obtained for R134a at 25.0, 35.0, and 49.7°C, R410A at 25.0°C, mass fluxes from 100 to 600 kg/m<sup>2</sup> s<sup>-1</sup>, qualities from 0 to 1 in 8.00, 5.43, 3.90, and 1.74 mm I.D. single, smooth, adiabatic, horizontal tubes in order to extend probabilistic two-phase flow map modelling techniques to single tubes. A new web camera based flow visualization technique utilizing an illuminated diffuse striped background was used to enhance images, detect

fine films, and aid in the automated image recognition process developed in the present study. This technique has an average time fraction classification error of less than 0.01.



**Fig. 12. Probabilistic two-phase flow regime map data for R410A, 100 kg/m<sup>2</sup>s, 25°C, 3.9 mm I.D. tube.**

As concluding remarks of this study, it can be said that probabilistic two-phase flow maps are found in the literature to be useful in the modelling of two-phase flow in multi-port microchannels. A two-phase flow loop was constructed and a new web camera based image recognition technique was developed in order to obtain the flow visualization images necessary to obtain probabilistic two phase flow map data for smooth, horizontal, adiabatic, single channel tubes.

The flow visualization technique utilizes a new optical method consisting of an illuminated striped diffuse background to enhance the images and aid in the image recognition process. Nearly, one million flow visualization images were obtained for R134a at 25.0, 35.0, and 49.7°C, R410A at 25.0°C, mass fluxes from 100 to 600 kg/m<sup>2</sup> s<sup>-1</sup>, qualities from 0 to 1 in 8.00, 5.43, 3.90, and 1.74 mm I.D. smooth, horizontal, adiabatic tubes in order to provide the flow visualization data necessary to create a generalized probabilistic flow regime map. Image recognition software is developed to classify the flow regime present in each image and formulate the time fraction of each flow regime for each flow condition. The time fraction error associated with the image recognition software is found to be a maximum of  $\pm 0.04$  and an average of  $\pm 0.01$  for the intermittent and liquid flow regimes and an average of  $\pm 0.01$  with a maximum of  $\pm 0.152$  for the stratified and annular flow regimes. Jassim developed curve fits of the present probabilistic two-phase flow map data in order to generalize the time fraction information using physically meaningful parameters. The time fraction information represented as continuous functions can be utilized to model single tube pressure drop,

void fraction, and heat transfer with a common two-phase flow map basis in a similar manner as Jassim and Newell demonstrated for multi-port microchannels.

### **3.3.General Considerations about the results found in the literature**

It is possible to have a satisfactory panoramic view of the results presented in the literature considering the Fig. 4 and Fig. 6 for what regards the two-phase flow in macro or conventional channels and Fig. 8 and Fig. 11 for the minichannels and microchannels.

It comes immediately clear how the flow in the microchannels is much more interested to be studied compared to the flow in the bigger tubes: in the smaller condition more flow patterns are visible and there is a very fast transition to one regime to another. In the macrochannels the transition is more smooth, and easier to be studied, and not all the main flow patterns can be observed.

From Fig. 4 and Fig. 6 it is clear that in the literature there is quite a good agreement on the location of the flow regimes on the maps and on their transition lines.

In particular, there is a common shift on the transition lines as function of the heat flux imposed to the flow and of the mass flux, but the modification of the map is not substantial and is in good agreement between all the researchers.

Going down with the dimension of the channels, considering Fig. 8 and Fig. 11 it is immediately visible how the low vapour quality region is dominated by a very fast transition of the flow pattern. Bubbly flow, difficult to be observed with the standard experimental technique, changes very rapidly to the slug and the annular regime, and this is something very different from the normal macro condition.

For the construction of the flow pattern map at the smaller scale there are several disagreements between the researchers about the transition lines and the regimes identified. Especially at the micro scale it is very difficult to maintain a very high objectivity in the flow pattern identification, and this is the reason why the researchers sometimes create flow pattern map quite different one from the other. Then, working at small dimensions, the importance of the relative errors of the measurements on the final results is higher, together with the difficulty in the definition of a precise flow pattern map.

These are the reasons why the experiments on the two-phase flow characterization at the micro scale are still being conducted; a huge amount of data from independent laboratories is necessary to obtain objective results.

### 3.4. Void fraction

#### 3.4.1. The study of Triplett, Ghiaasiaan, Abdel-Khalik, LeMouel, McCord [16]

Void fraction and two-phase frictional pressure drop in microchannels were experimentally investigated. Using air and water, experiments were conducted in transparent circular microchannels with 1.1 and 1.45 mm inner diameters and in microchannels with semi-triangular (triangular with one corner smoothed) cross-sections with hydraulic diameters 1.09 and 1.49 mm. Gas and liquid superficial velocities were varied in the 0.02-80 m/s and 0.02-8 m/s ranges, respectively, and void fractions were calculated by analyzing photographs taken from the test sections with circular cross-section.

Measured void fractions were compared with several correlations. The homogeneous flow model provided the best prediction of the experimental void fractions in bubbly and slug flow patterns.

The homogeneous flow model and all other tested empirical correlations significantly over predicted the void fractions in annular flow pattern, however.

Void fractions were estimated by analyzing photographs taken from the centre of the test section. Each photograph typically covered a 6 mm-long segment of the test section.

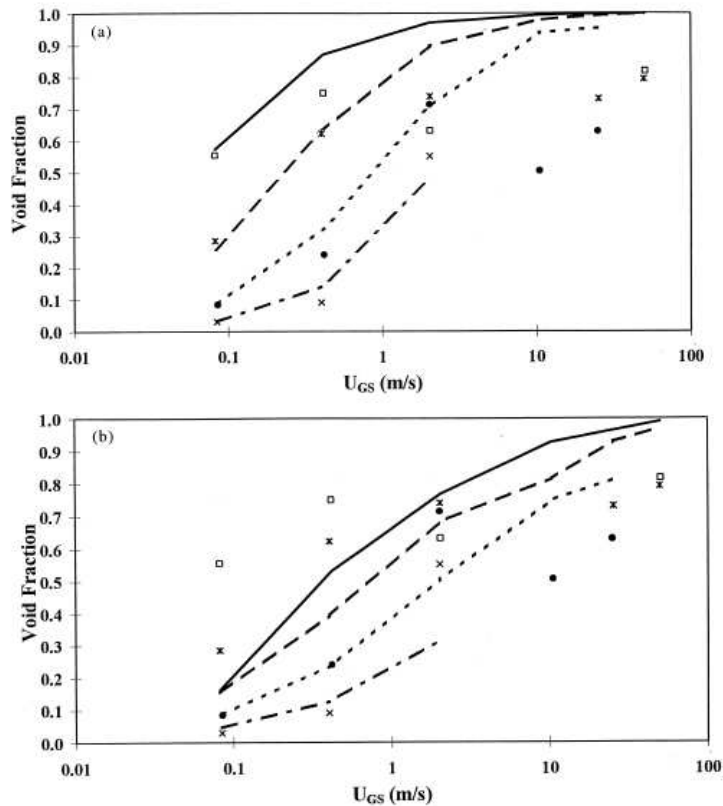
In the bubbly flow pattern, individual bubbles were assumed to be spheres or ellipsoidal, depending on their shape. In slug flow, the Taylor bubbles were divided into cylinders and spherical segments. In bubbly flow each photo typically covered a large number of bubbles, thus providing a reasonable volume-averaged estimate of the void fraction. In slug flow the flow pattern is relatively regular and average Taylor bubble and liquid slug lengths were calculated from multiple photos and used for void fraction calculation.

In the annular flow pattern the vapor core was divided into several cylinders and the channel average void fraction was calculated accordingly. Slug-annular and churn flow patterns were the most difficult flow regimes to analyze. The void fractions associated with slug-annular flow patterns are not included in the analysis due to their high uncertainty. In churn flow, an average of 0.5 local void fraction was assumed in segments of the flow field where the gas phase was dispersed.

As concluding remarks of this study, it can be said that void fraction and two-phase pressure drop were measured in transparent long horizontal microchannels with circular and semi-triangular (triangular with one corner smoothed) cross-sections. The test section hydraulic diameters were 1.1 and 1.45 mm for circular channels, and 1.09 and 1.49 mm for semi-triangular cross-section test sections. The gas and liquid superficial velocities were varied in the 0.02-80 m/s and 0.02-8 m/s ranges, respectively. Flow patterns were discussed in part I of this paper.

Measured void fractions were compared with predictions of the homogeneous mixture model, the correlation of Butterworth [7] representing the empirical correlation of Lockhart and Martinelli [1] the CISE correlation [4]. A one-dimensional model based on the numerical solution of mass and momentum conservation equations was used for calculating the channel pressure drops utilizing various two-phase friction models. The two-phase friction factors based on the homogeneous mixture assumption and the empirical correlations of Chisholm [5] and Friedel [9] were examined.

Void fraction and channel pressure drop (Fig. 13) were best predicted by the homogeneous mixture assumption. The tested models and correlations all over predicted the channel void fraction and pressure drop in the annular flow pattern, suggesting that the annular flow liquid&gas interfacial momentum transfer and wall friction in microchannels may be significantly different from similar processes in larger channels. Systematic experiments addressing the hydrodynamics of the annular flow pattern in microchannels are thus recommended.



**Fig. 13. Comparison of measured void fractions with predictions of various correlations. (a) homogeneous model; (b) Chexal et al.**

### 3.4.2. The study of Wojtan, Ursenbacher, Thome [30]

A new non-intrusive computerized image analysis and optical observation method for accurately measuring dynamic void fraction has recently been developed by Thome and co-workers. This technique is applied to circular horizontal sight glass tubes using a monochromatic laser sheet to illuminate the two-phase flow coupled with image processing to measure cross-sectional void fractions and dry angles in stratified types of flow. The refraction effects on the cross-sectional images are overcome by reconstructing the video images by computer. From these, the shape at the vapor-liquid interface is detected and the void fraction is accurately determined (to an estimated accuracy of about  $\pm 0.01$ ) over a wide range of void fraction values (from 0.05 to 0.95). In addition, the dry angle around the upper perimeter of the tube is also obtained. The system has been coupled to a flow boiling test facility to obtain dynamic and time-averaged void fractions in a horizontal tube for two refrigerants: R-22 and R-410A. About 227,000 images were analysed so far in this study for a 13.6 mm tube to provide the same number of dynamic void fraction measurements and 238 time averaged void fraction values (Fig. 14). A summary of the technique is described here with additional analysis of the previous results and new results (based on processing 83,000 new images) are presented here for void fractions in an 8.0 mm sight glass tube with R-22 at mass velocities of 100 and 150 kg/(m<sup>2</sup> s). The new method also has the potential to measure interfacial wave contours and other pertinent geometrical characteristics of stratified two-phase flows.

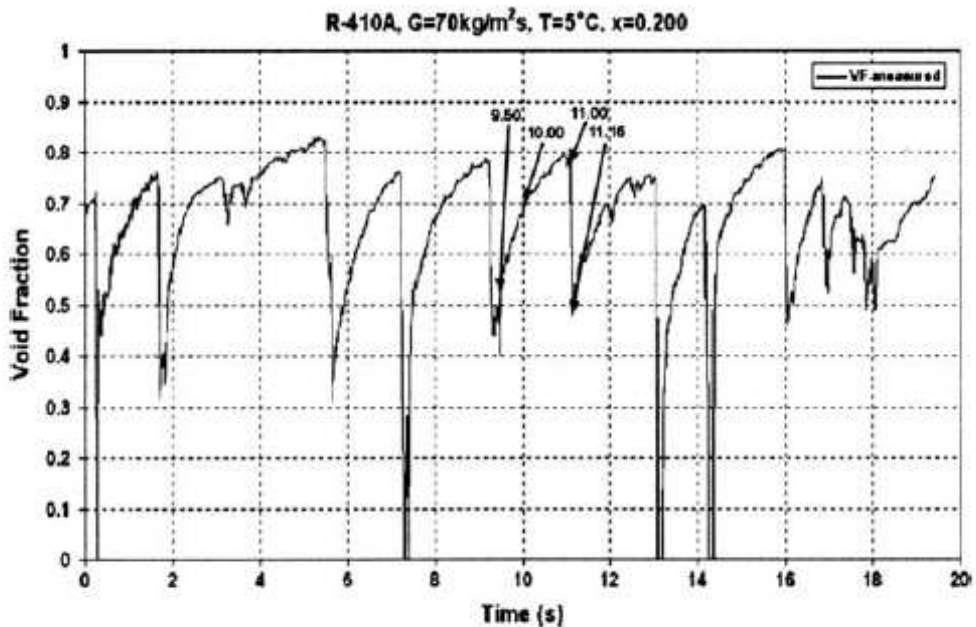


Fig. 14. Void fraction evolution for stratified-wavy/intermittent flow.

As concluding remarks of this study, it can be said that a recently developed optical measurement technique to dynamically measure the location of the vapor–liquid interface in two-phase stratified flows in horizontal tubes is described and some new results for an 8.0 mm sight glass tube are shown in comparison to the previous results for 13.6 mm. The new method is non-intrusive and allows measurements of the dry angle and void fraction through a glass tube in a cross-sectional view perpendicular to the flow. This technique has been optimized for stratified types of flow and some slug flows, all without entrained bubbles, and yields void fractions with a measured precision in absolute value on the order of  $\pm 0.01$  over the range from 0.05 to 0.95. As shown in this study, the technique is more difficult to apply to small diameter tubes than larger ones.

Based on a statistical comparison, the drift flux model of Rouhani and Axelsson [15] as modified by Steiner [3] for horizontal flows is the best of the four models tested and accurately predicts the stratified flow void fraction data. Secondly, the Taitel and Dukler [8] stratified flow transition model for liquid height gives nearly as accurate results for calculating the void fraction. New dry angle measurements are also reported for an 8.0 mm sight glass tube and are accurate to about  $\pm 10^\circ$ .

#### 3.4.3. The study of Kawahara, Chung and Kawaji [21]

An experimental investigation has been carried out on two-phase flow characteristics in a 100  $\mu\text{m}$  diameter circular tube. Two-phase flow patterns were determined by video recording the flow in the transparent capillary tube made of fused silica, in which de-ionized water and nitrogen gas were injected at superficial velocities of  $j_G = 0.1\text{--}60$  m/s for gas, and  $j_L = 0.02\text{--}4$  m/s for liquid. Time-averaged void fraction and two-phase friction pressure drop data were also obtained and analyzed. The flow patterns observed were intermittent and semi-annular flows, but a closer study of the liquid film structure revealed gas core flows with a smooth or ring-shaped film and a serpentine-like gas core surrounded by a deformed liquid film. Bubbly and churn flow patterns were not observed. A flow pattern map was developed based on the probability of appearance of each type of flow, and compared to the existing flow pattern maps obtained for 1 mm diameter channels. Void fraction remained low even at high gas flow rates, indicating large slip ratios and weak momentum coupling between the phases. The single-phase friction factor and two-phase friction multiplier data were shown to be in good agreement with the conventional correlations.

Time-averaged void fraction data were obtained from the analysis of two-phase flow images captured at different flow rates. The time-averaged void fraction remained low even at high gas flow rates, indicating significantly larger slip ratios and weaker momentum coupling between the phases, compared to the flows in channels with  $D_H = 1$  mm. This was consistent with the occurrence of predominantly liquid-only or separated flow patterns in the microchannel.

### 3.5. Experimental measurements in two phase flow

Considering the avant-garde scientific literature regarding the experimentation in two phase flow, it is possible to find some common technique in which the studies are conducted.

This is true in particular for the visualization study. In these kind of experiments, all the data come from the adiabatic part of the glass transparent tube, because usually the heaters that are used to provide to the flow the necessary amount of power to boil are made of metal tubes.

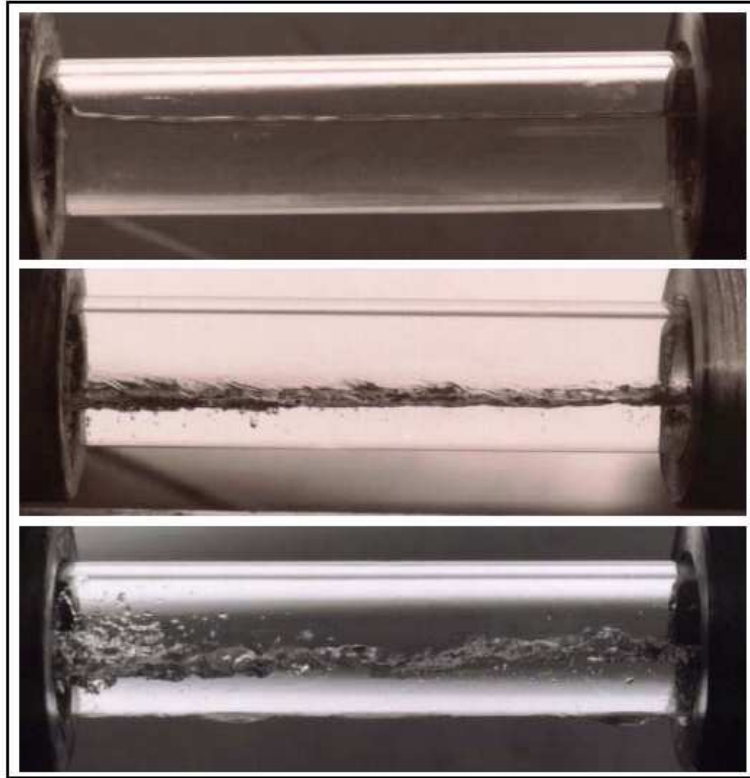


**Fig. 15. Conventional visualization windows in two-phase flow.**

This is very evident in the Fig. 15 and 16, where the most common setup for visualization experiments is presented.

The camera is usually positioned after the heater, because this is usually the only transparent part of all the system, and for this reason there is no information about what is really happening –from the point of view of bubble history- inside the diabatic zone of the tube.

This fact represents a big lack of information in the study of the two phase flows, and for this reason we oriented our work in a way that could make more complete the set of information on the onset of boiling. This was done using a completely transparent test section, including the heating part. More details about this setup will be presented in the next section.



**Fig. 16. Stratified flow regime photographs of Barbieri, Saiz-Jabardo and Bandarra. Top: stratified flow; middle and bottom: stratified-wavy flow. Tube diameter: 15.8 mm.**

### **3.6. Conclusions**

Many studies now exist on two-phase flow in microchannels.

Many of them (not all presented here) are adiabatic two-phase flow experiments, i.e. liquid and gas flowing in the same pipe without any heating, generated by a gas injector or liquid- vapor mixer. The resulting flow pattern and bubble characteristics are probably imposed or influenced by the design of the injector or mixer (none of those studies addressed this issue).

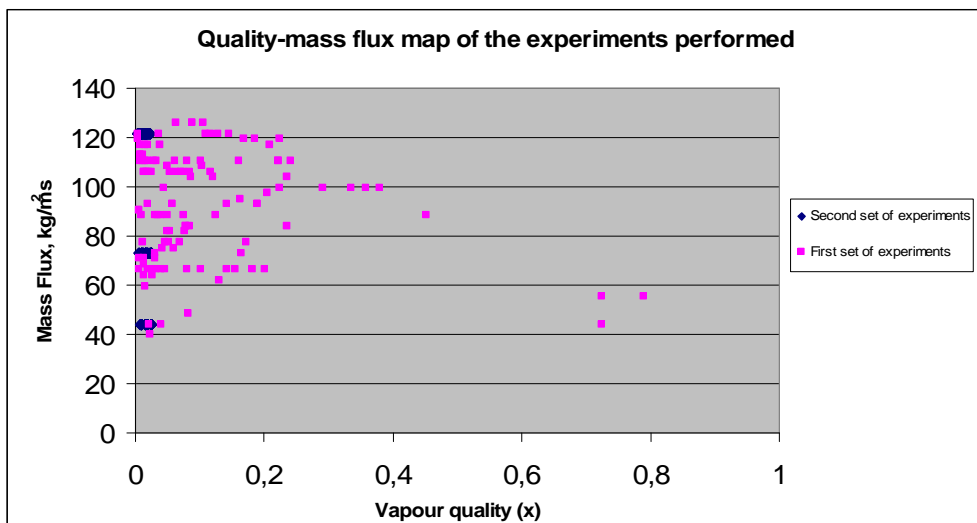
Only few studies were for diabatic experiments (with evaporation or condensation). Based on the present summary of existing experimental work, one can conclude that only three principal flow patterns can be used to describe two-phase flow in microchannel: bubbly flow, confined bubble flow and annular flow. No stratified flow is observed in microchannels due to the predominance of surface tension over gravity forces so that the tube orientation has negligible influence on the flow pattern. Too many regime designations lead to too much complexity when trying to develop a model based on these flow regimes.

The subjectivity related to the flow pattern observation and their transition determination is another difficulty. How to say if a bubble is isolated or not? How can one determine the transition from wavy-annular to annular many questions and uncertainties arise due to this lack of objectivity in the identification of the flow patterns. Thus, an objective method should be used to create a correct flow pattern map starting point for building heat transfer and pressure drop models.

Multiple geometries can lead to a new difficulty of fundamentally studying two-phase flow in microchannels, and some researchers found that the characteristics of two-phase flow are the same for single and multiple channels. The choice of the channel size can also be a problem because that determines either macro or microscale or the transition between them.

Thome et al. [33, 34] proposed the first mechanistic heat transfer model to describe evaporation in microchannels with a *three-zone* flow boiling model that describes the transient variation in the local heat transfer coefficient during sequential and cyclic passage of (i) a liquid slug, (ii) an evaporating elongated bubble and (iii) a vapor slug when film dryout has occurred. Fig. 10 depicts a schematic of their three-zone heat transfer model. The new model illustrates the strong dependency of heat transfer on the bubble frequency, the lengths of the bubbles and liquid slugs, and the liquid film thickness but is so far only applicable to the slug flow regime.

For these reasons, it is opportunistic to apply an optical measurement technique to simultaneously and quantitatively characterize flow pattern transitions, and measure the frequency, velocity and length of vapor bubbles in microchannels, in particular at the exit of microevaporators in which the flows are formed.



**Fig. 17.** Mass flux vs. vapour quality map showing the experiments performed during the thesis.

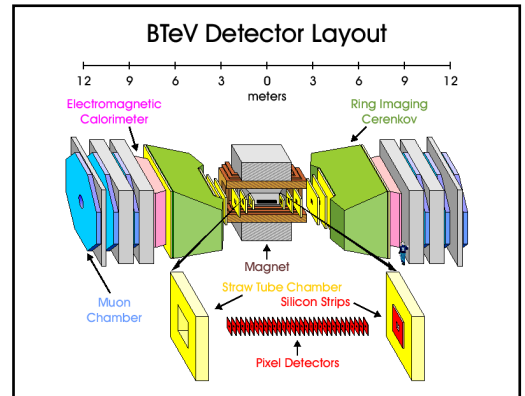
In the present work, all the boiling phenomena will be analyze from the visualization point of view, and to give an idea of which part of the flow pattern map has been considered, Fig. 17 has been reported. It becomes clear that during the first set of experiments a good portion of the vapour quality has been considered, arriving almost at the annular flow condition, while in the second set of experiments much more relevance has been given to the bubbly flow regimes that are visible at the very low vapour quality.

## 4. EXPERIMENTAL APPARATUS

In this section a detailed description of the experimental test rig optimized for two phase flow analysis will be presented. The main innovation is in the completely new transparent heating system applied to the test section that allows two phase flow visualization not only in the adiabatic part of the glass tube, but also in the diabatic.

### 4.1. Starting point

In 2005 the University of Bergamo was involved in the project BTeV regarding the construction of one part of the particle detector at Fermilab, Chicago. For our unit, the object of the work was to design and build a polymeric mini-channel system for the cooling of a CARBON high-energy strip of the particle detector.



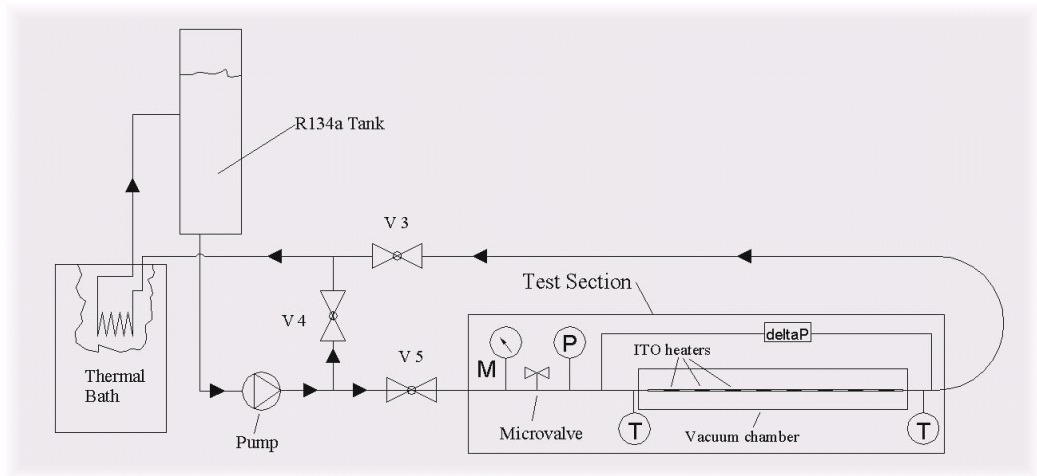
**Fig. 18.** The first version of the test rig built to make experiments regarding the cooling of a strip of a particle detector at FERMILAB, Chicago.

The experimental system shown in Fig. 18, working with R134a, was created, and after one year, before the first tests were run, the project was closed and the test rig remained at the University of Bergamo.

## 4.2. The experimental test-rig

The existing test rig was improved according to the new set of two phase flow experiments that had to be done. A schematic view of the improved experimental apparatus is given in Fig. 19. It works with R134a and consists of two main loops: the test section loop and a secondary loop, where the fluid is thermally controlled and all the vapor formed in the test section is condensed.

A helix type heat exchanger is inserted into an external cooling unit, which maintains propylene glycol at a constant pre-imposed temperature (down to  $-40^{\circ}\text{C}$ ). This unit is necessary to define the operating experiment temperature and to condense the fluid coming from the testing section as wet vapour.



**Fig. 19. Experimental test rig scheme**

A start-up procedure, consisting on closing the test loop and circulating the fluid into the secondary loop, is necessary. This procedure is necessary to assure all the fluid inside the tank at the desired pressure and temperature, in general between  $0^{\circ}\text{C}$  and  $30^{\circ}\text{C}$ .

The mass flow rate can be adjusted by working on the micro regulation valve positioned at the inlet of the test section, by closing the bypass valve or by changing the pump speed, so that the resulting flow rate is a consequence of the interaction of the regulation of these features.

After these steps, being all the system at the required condition, it is possible to open the test section loop and heat the fluid inside the test section, visualize and record the images coming from the camera and acquire and store the data coming from the sensors.

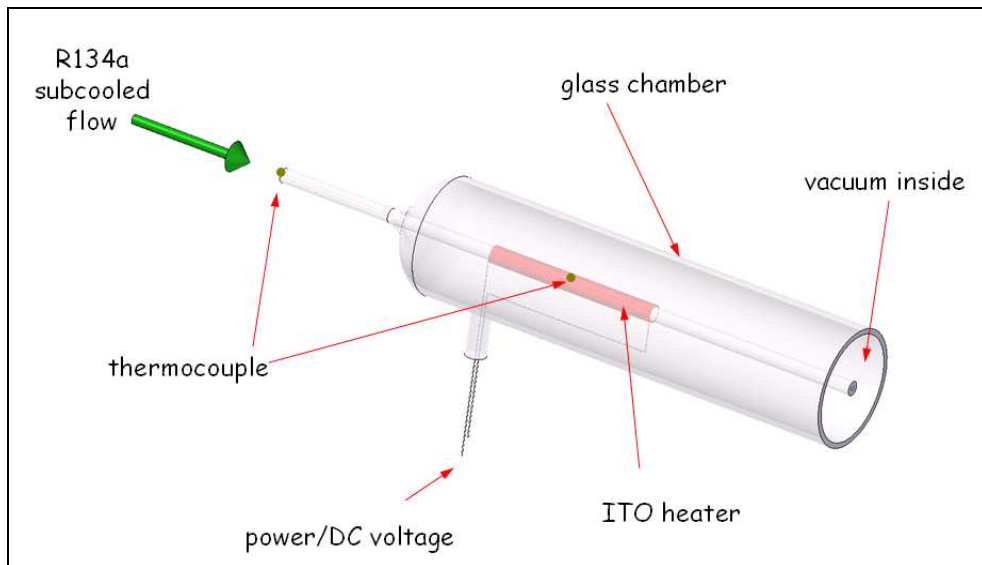
The new test section is made up of the elements presented in Fig. 23. The liquid refrigerant comes from the pump to the mass flow meter, and then enters the test

section passing from a micro-regulation valve, after which temperature and pressure are measured.

#### 4.3. The new test section

The test section is a high precision glass (DURAN) tube having different internal diameters, from 4 to 0.4 mm and lengths, typically from 1000 to 500 mm, and the heating system consists of ITO (Indium Tin Oxide) coating on the outer surface of the tube.

The coated tube is enclosed in a co-axial vacuum chamber made by a glass tube of larger diameter, in order to eliminate, in the global heat transfer rates, the convection losses consider only the radiation losses of the heaters between the environment and the test section (Fig. 20).

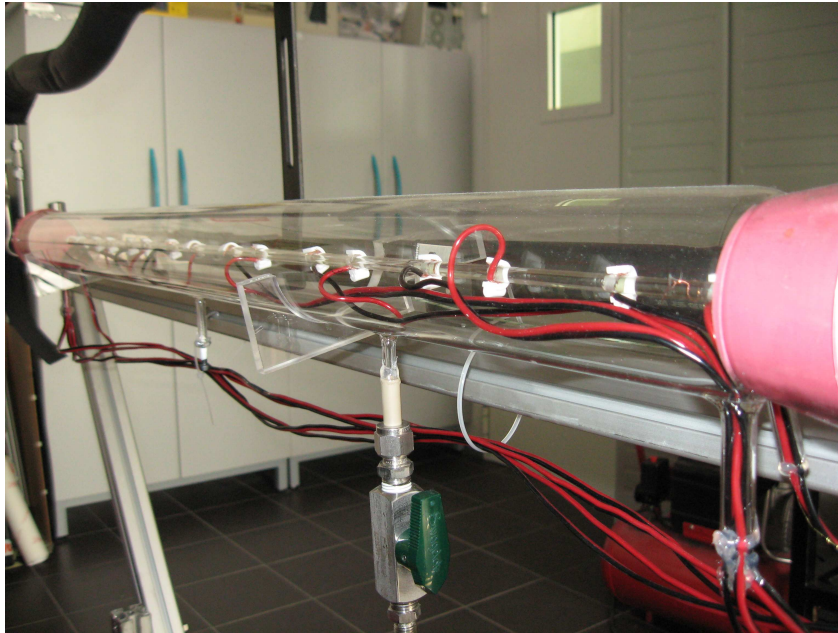


**Fig. 20. Schematic view of the basic unit of the test section: the glass tube, the heaters and the glass chamber that encloses the tube.**

The versatility of the whole system is due to the possibility to easily change the tube of the test section with tubes of smaller diameter and different distribution of coating length. For this reason, the present system can work with tubes with an internal diameter from 4 to 0.4 mm, and with heat fluxes from 0.5 to 300 kW/m<sup>2</sup>. This can be done by easily changing the test tube, and substituting it with one with a smaller internal diameter.

The vacuum deposited ITO film is used to electrically heat the glass surface allowing observing the boiling mechanisms taking place inside the tube. In the present test

section, 4 mm internal diameter there are eight heaters on the outer surface of the glass tube, making it possible to reach heat fluxes from 2 to 40 kW/m<sup>2</sup>.



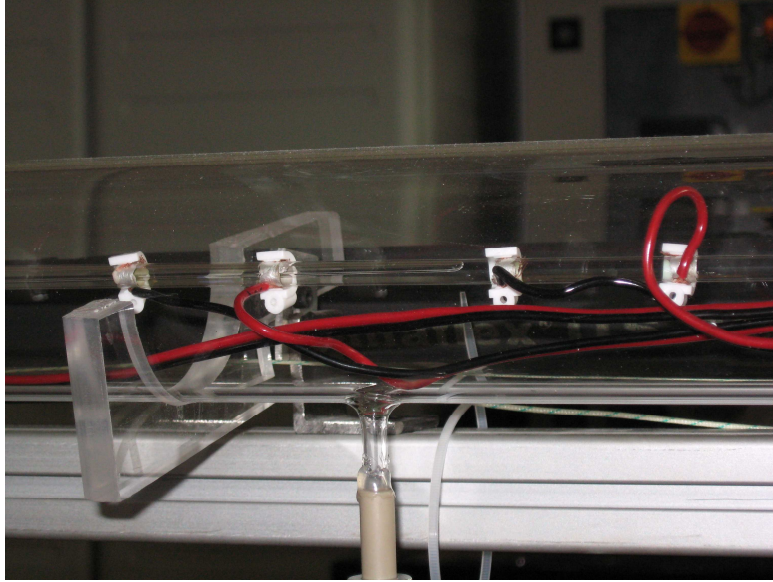
**Fig. 21. Test section in the operating condition.**

The heater is actually made by a certain number of layers of ITO and this number has been chosen according to the total final amount of heat power that could be given to the flow, and to the possibility to regulate it more precisely.

In this way low vapor quality flows are easily obtained and a slow and precise increasing in heat flux is obtained. An image of the test section is visible in Fig. 21.

#### **4.4. The new heating system**

Indium tin oxide layers with variable length, characterized by a mean electric resistance of 50 Ohm/square have been coated on the outer surface of different internal and external diameter glass tubes (**Errore. L'origine riferimento non è stata trovata.**2). Typically, the ranges of the final resistance of each heater is between 65 and 300  $\Omega$ . ITO thin films are electrically conductive and have the characteristics of high optical transmittance (in our case around 85%) over the visible wavelength region, and excellent adhesion to glass substrates.



**Fig. 22. Image of the test section showing the electrical wires that provide power to the ITO heaters and the white connectors that fix the wires at the borders of the coating.**

Indium tin oxide is a conductive oxide that has the benefit of being simultaneously electrically conductive and transparent to visible light. When ITO is vacuum deposited on an appropriate transparent surface it provides the opportunity to observe - from a new perspective - boiling through the electrically heated surface.

The resistivity of a coating is inversely proportional to its thickness, since the layer has a bulk resistivity  $\rho_b$  ( $\Omega \text{ m}$ ) and final resistance  $R_{ITO}$  ( $\Omega$ ) which are found from:

$$R_{ITO} = \left( \frac{\rho_b}{t} \right) \left( \frac{L}{W} \right) \quad (4.1)$$

where  $L$ ,  $W$ ,  $t$  are, in the case of a tube, the axial length, the circumference and the thickness of the coating, respectively.

It is important that the coating has a resistance that is low enough to ensure that sufficient power can be applied to the surface with practical, readily available power supplies.

From Ohm's law

$$V_{ITO} = \sqrt{P_{ITO} * R_{ITO}} \quad (4.2)$$

where  $V_{ITO}$  is the voltage and  $P_{ITO}$  is the heating power, therefore, for a given heating power  $P_{ITO}$ , to minimize the required voltage potential  $V_{ITO}$  to safe and practical levels,  $R_{ITO}$  needs to be low.

#### 4.5. Data acquisition devices

To control the flow characteristic at the inlet and outlet of the test section, there are several devices that measure many physical quantities of the refrigerant. All these instruments are visible in the Fig. 23. At the entrance of the test section there is a rotameter that measures the flow rate till a maximum of 5,5 kg/h, then there is a micro regulation valve that is needed to have very precise regulation of the flow and to stabilize the flow itself. Subsequently refrigerant temperature and relative pressure are measured in sequence respectively with a thermocouple and a pressure sensor.

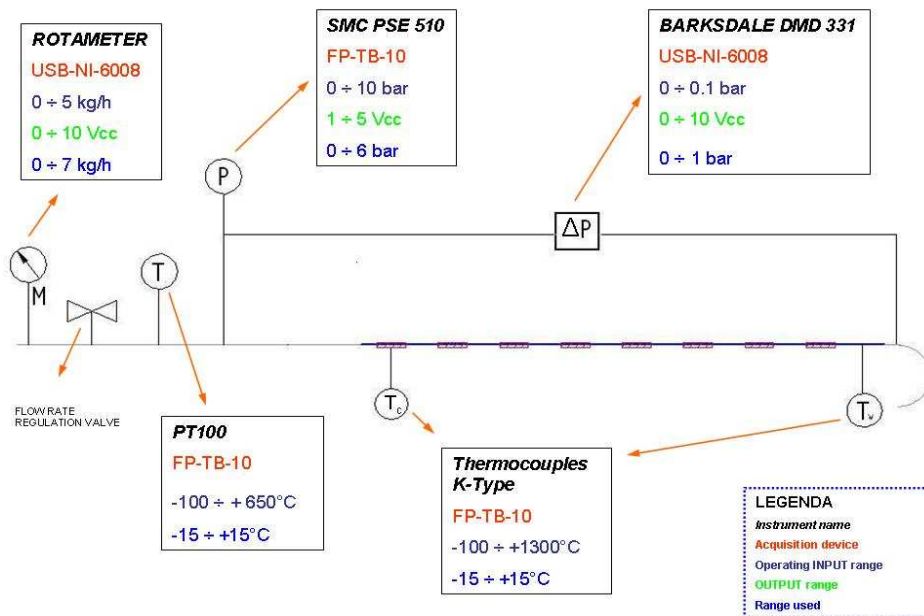


Fig. 23. Test section instrumentation scheme.

Between the entrance and exit of the test section a differential pressure meter is positioned to measure the pressure drop during flow boiling.

From the temperature point of view, in this configuration a thermocouple is positioned on the first coating and one on the outer surface of the glass tube at the exit of the test section. From the value of the temperature measured for the first heater, the temperatures of the other heaters are obtained considering a direct proportional temperature governing law.

ITO coatings power is controlled by the PC through several NI® (National Instrument) USB-6008/9 acquisition and control devices and the specifically designed electronic boards (one for each heater), which are supplied with a 56V DC power supplier, as sketched in Fig. 25.

Every electronic board (Fig. 24) applies the correct value of voltage to each heater in order to reach the desired electrical power and amplifies the coating voltage and current



(proportional-integral-derivative) control, which is easy-to-handle and adaptable to all different coatings, with no need for specific tuning. As preliminary tests have shown that the coatings start to deteriorate at relatively low temperatures ( $\sim 80^{\circ}\text{C}$ ), the control module checks if the temperatures stay sufficiently below the limit and stops power supply if the threshold is exceeded. Furthermore, a sub-module estimate the heat losses due to heat conduction and radiation.

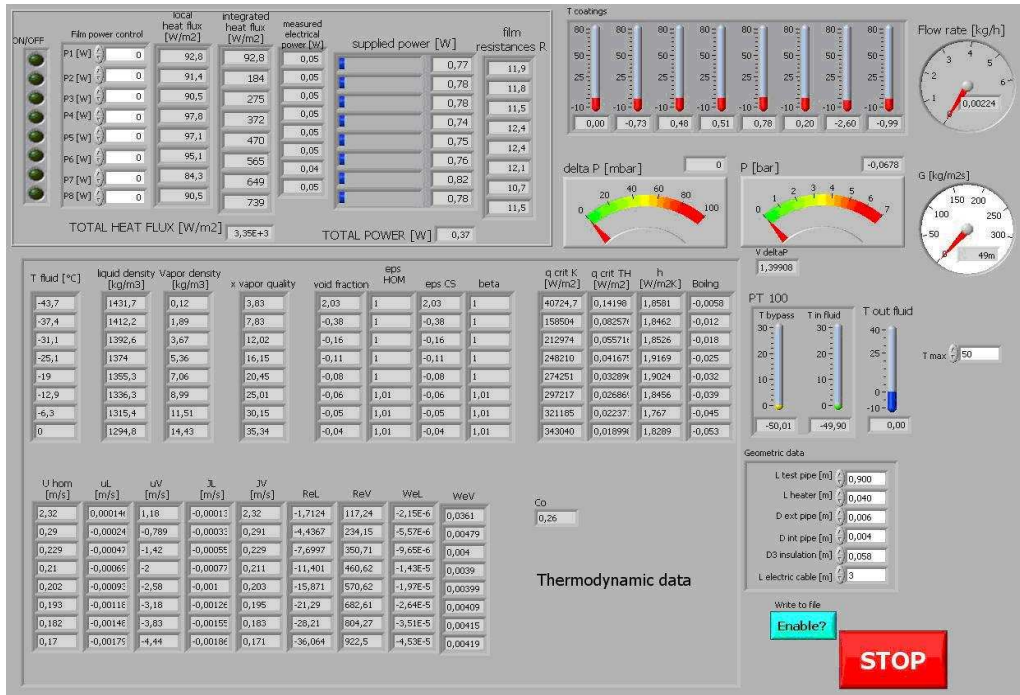


Fig. 26. LabVIEW control panel interface.

All the most significant acquired data, of which a detailed list is provided in the next paragraph, are acquired with a frequency of around 20Hz, which is considered adequate for stationary flow. The data are periodically averaged ( $\sim 1\text{Hz}$ ), so that mean values (and optionally standard deviations) are available and stored for future post-processing.

#### 4.6. The experimental condition and the flow visualization

During experiments the configuration of the test section is showed in Fig. 28 and 29. As can be seen from the image, there are three main components working simultaneously to perform the visualisation and heat transfer experiments. First of all the high speed camera, that allows the recording of videos of the flow configuration inside the test section, both in the diabatic and in the adiabatic zones. Usually the

camera works at a speed of 1000 frames/s to have well defined bubble contours in the frames of the videos.

The second important part is made up on one side by the light and on the other by the infrared filter together with the light diffuser.

The time rate set for the experiments presented in the next paragraphs is 1000 fps, but the camera has the possibility to work also at a faster acquisition speed. As luminous source one or two continuous current lamps of 65W are used.

Due to the big amount of heat radiation produced by the lamp, and in order to eliminate this additional power in the heat transfer calculations, a special infrared (IR) filter has been positioned between the lamp and the test section. Some tests have been carried out to check the efficiency of this filter and the results are shown in Fig. 27.

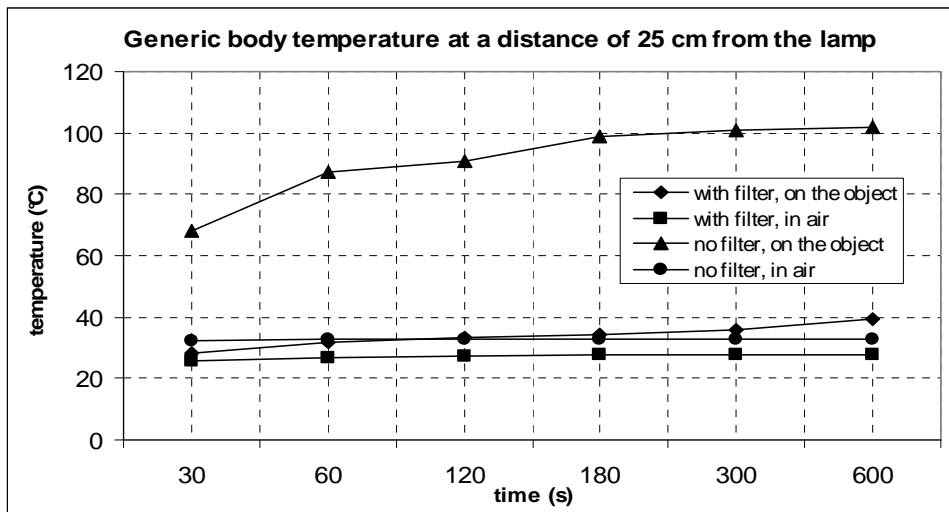
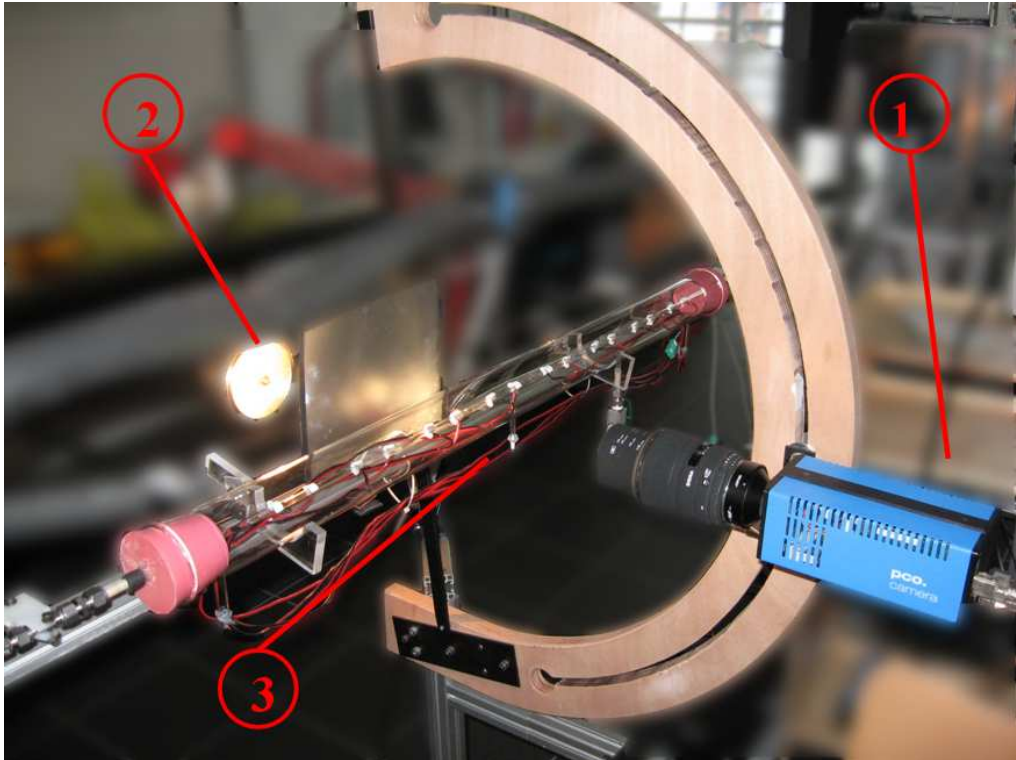


Fig. 27. Temperatures with and without the IR filter.

During these tests four different configurations were considered: with and without the IR filter and with the thermocouple in air or positioned on a black body. The presence of an object was necessary to simulate the presence of the surface that is involved in the mechanism of the radiative heat transfer from the lamp, and the results obtained in the two configurations with and without the object underlined the importance of such a choice: if the body is neglected a large amount of radiation is not taken into account, making a large error in evaluating the real radiative power. In the end it is possible to conclude that the IR filter is able to stop the 90 % of the total amount of power produced as radiation by the lamp.

The remaining quantity is taken into consideration in the calculations involved during the data acquisition process.

The distance of the light from the glass tube is of about 35 cm, and the filter is positioned 10 cm far from it. The camera on the other side is fixed with a specific

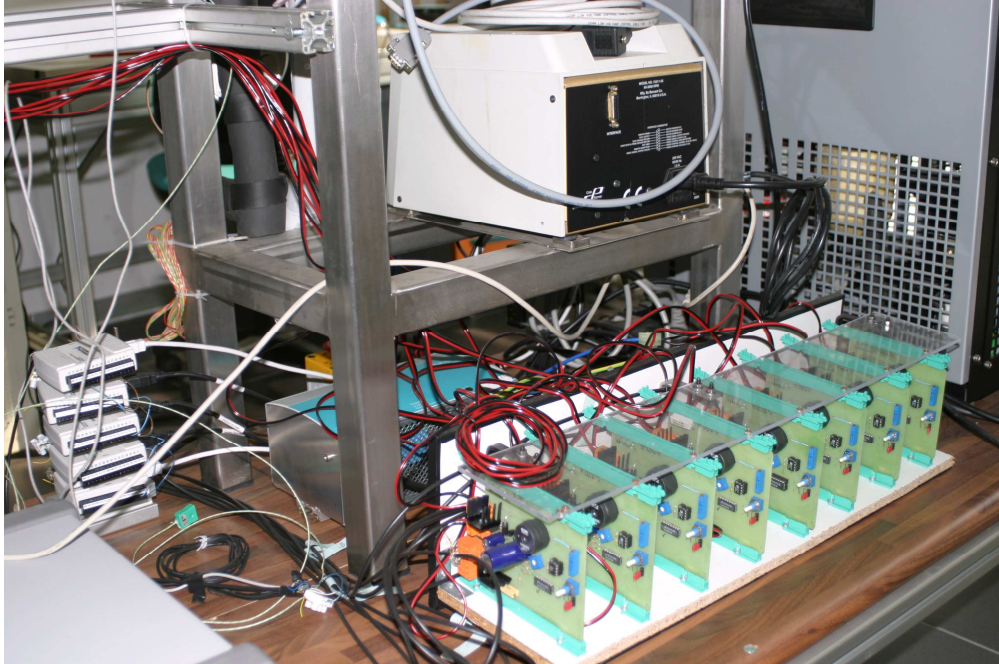


**Fig. 28.** Image of the test section, where it is possible to notice the high speed camera (1), the light source (2) and the test section (3).

support on a semi-circular structure to ease its movement around the test section and to acquire images from every angulations respect to the horizontal requiring only small regulations on the focus.

The dimensions mentioned before were qualitatively determined to best enhance the detection of fine films for the 4.00 mm diameter tube, and are varied according to pipe diameter to maintain approximately the same stripes per pipe diameter length and the same stripe width and spacing per pipe diameter length.

The peculiarity of the technique that was adopted is that, thanks to the completely transparency of the test section, it is possible to study the evolution of the flow pattern established at the beginning of the tube and also after the introduction of more power in different positions along the tube.



**Fig. 29. Electronic boards to control the amount of power given to each heaters.**

#### **4.7. Conclusions**

In the present section a detailed and complete presentation of the new experimental apparatus was presented. The new test rig has the innovating characteristic of having a completely transparent test section. This result was obtained using some ITO layers as heaters instead of the traditional stainless steel heating tubes.

The experimental apparatus is very versatile and presents a good reliability of the measurements.

## 5. PREDICTION OF THE HEAT FLUXES IN THE TEST SECTION

When an electrical power is supplied to the ITO heaters the heat transfer mechanism begins in the test section. In the next paragraphs a detailed description of the different kind of heat fluxes within one basic unit of the test section will be presented.

### 5.1. Global heat fluxes

To evaluate the net heat flux that is entering the fluid we can focus the calculation on one basic unit of the test section (Fig. 30), a part made of the glass tube including one complete heater, the glass part before and after the coating, the relative glass enclosure and the environment.

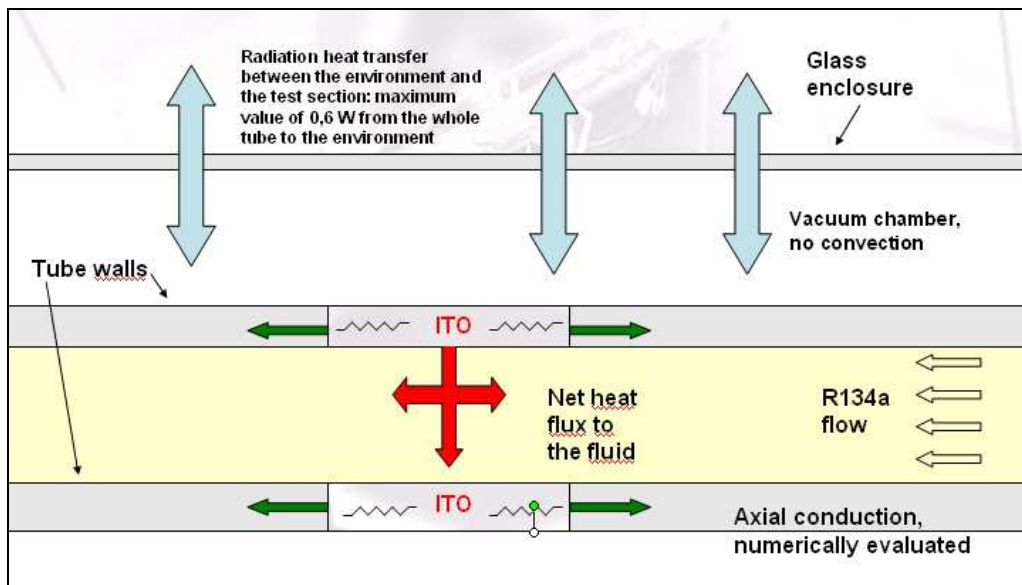


Fig. 30. Scheme of the heat fluxes in one basic unit of the test section.

For the kind of test section considered in this thesis, the maximum power that one heater can provide is around 20 W at a temperature between 35 and 45°C respectively in the case of the maximum and minimum mass flux, considering the fluid at a temperature of 20°C.

Making this first consideration, within the test section it is possible to consider several heat exchanges between the coating and the glass, the fluid and the environment.

In particular we can identify the following heat fluxes:

- a convective heat transfer between the outer surface of the heater and the surrounding air;
- a convective heat transfer between the glass enclosure and the environment;
- a radiative heat flux between the coating and the environment and the uncoated glass and the environment;
- an axial conduction in the tube starting in the confining region between the heater and the uncoated tube;
- a convective heat flux from the heater to the fluid.

Thanks to the design of the test section, the first contribution can be neglected because the test section is enclosed into a glass chamber with vacuum inside. This characteristic assures that the convection on the outer surface of the test section is zero.

For estimating the second contribution, the correlation for the convective heat transfer between a tube and quiescent air has been used, and the values found have been very small compared to the other quantities. This amount of heat transfer has been anyway considered in the global behaviour of the test section.

To evaluate the third contribution, the coated and uncoated areas have been considered differently, because each of them is at a different temperature while the experiments are running. Radiation has been evaluated according to the standard electrical analogy theory of the heat transfer between two gray surfaces at different temperatures.

The axial conduction in the glass tube has been evaluated numerically and a specific study is presented in the next paragraph.

Evaluating all the different heat fluxes around every single heater, it has been possible to consider only the net amount of heat entering the flow, having subtracted the heat losses listed above. According to this, inside the LabVIEW control panel that is used to set the value of power given to the flow, a routine has been included so that it is shown on the display the net real amount of heat going to the flow. In this way, when a certain power is imposed to one heater, the number visualized in the LabVIEW control panel is the real value of power going to the flow.

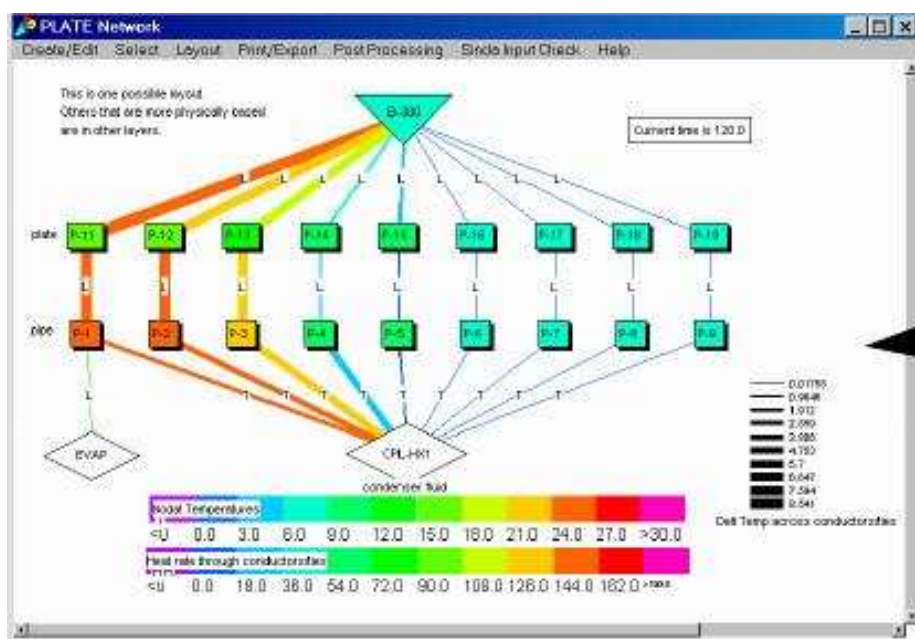
#### 5.1.1. Heater numerical simulation-axial conduction

A numerical activity, using the lumped parameter code called SINDA/FLUINT, has been carried out in order to estimate the heat release to the environment and the axial conduction along the tube.

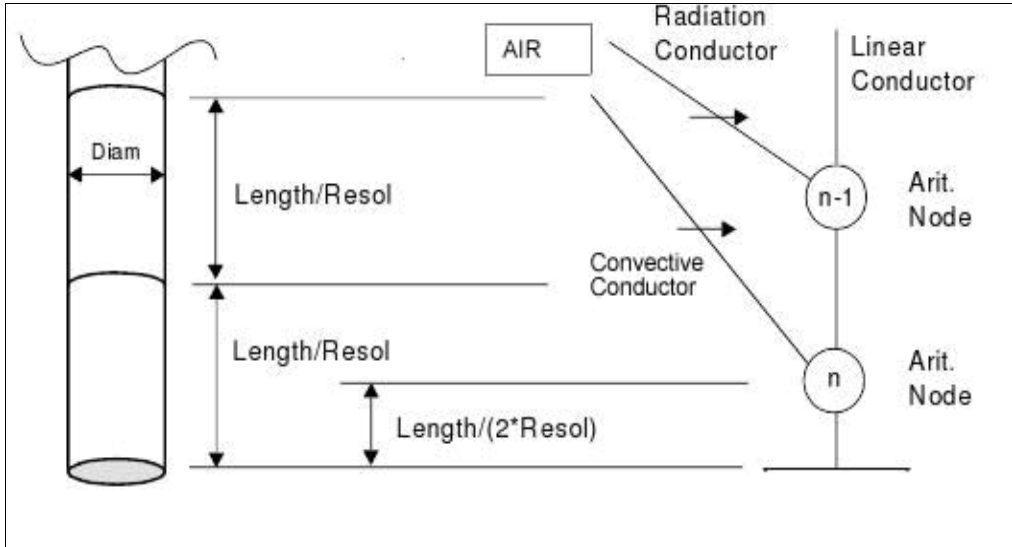
From the point of view of the ITO coating, while there is a very high precision in the total electrical power provided to the flow inside the tube, the uncertainty in the evaluation of the heat flux can vary a lot according to the power. This is mainly due to the axial conduction in the glass tube of the power produced by the heaters.

For this reason, the problem of defining the real heat flux provided to the fluid has been solved numerically.

### 5.1.2. Lumped thermal simulation: SINDA/FLUINT



The user poses a problem by creating an arbitrary network of thermodynamic points (*lumps*) connected by fluid flow passages (*paths*). The user may also define heat transfer routes (*ties*) between SINDA nodes and FLUINT lumps to simulate convection. In two-phase flows, in bubbly and slug flow regimes the predicted pressure drops are based on the McAdam's formulation for homogeneous flow. When the regime is determined to be annular, the Lockhart-Martinelli correlation is used.



**Fig. 32. Radiative and convective heat transfer between the tube and the air modelled with SINDA/FLUINT.**

Considering the modelling of a portion of the test section, the heat power and the conductances to the ambient and between the two tubes simulate the convective and radiative heat losses (Fig. 31 and Fig. 32).

In particular, the convective heat transfer is present only on the outer surface of the vacuum chamber and is calculated by the Churchill and Chu equation that is usually used for the horizontal, isothermal cylinder in the case of free convection:

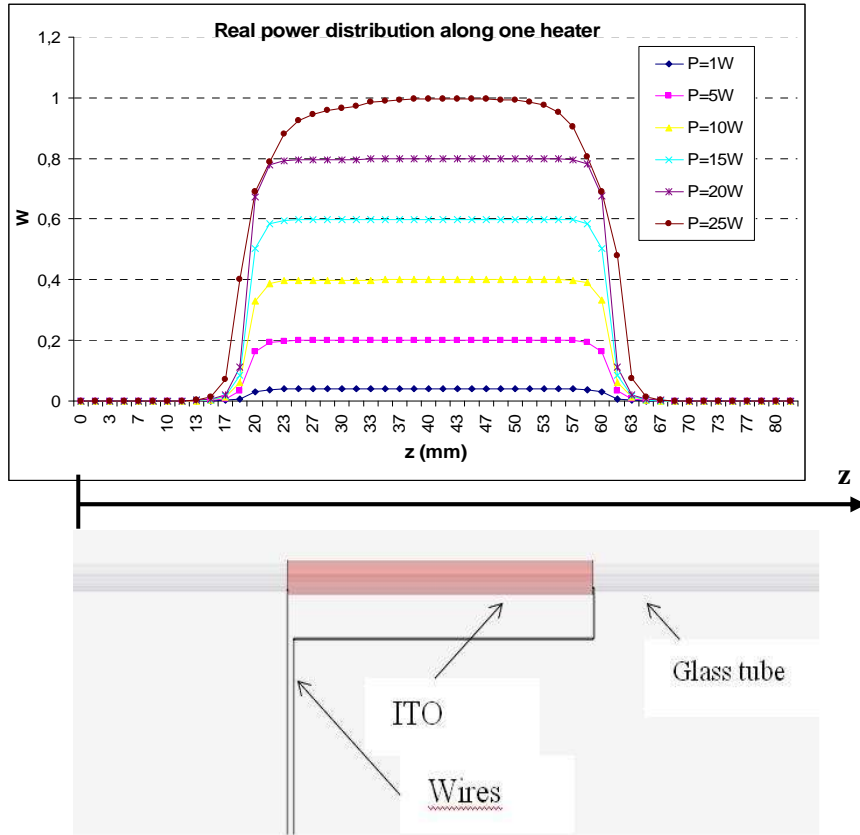
$$Nu_D = \left\{ 0.6 + \frac{0.387 Ra_D^{1/6}}{\left[ 1 + (0.559/Pr)^{9/16} \right]^{8/27}} \right\}^2$$

where  $Nu$  is the Nusselt number,  $Ra$  is the Rayleigh number and  $Pr$  is the Prandtl number.

To evaluate the amount of the radiative losses from the test section to the vacuum chamber and the environment, the radiation heat exchanges have been evaluated applying the classical theory for radiation between grey bodies. Both these two heat losses are included in the two models that will be presented in the next paragraph.

### 5.1.3. Results

Two numerical models have been implemented, each calculating the local value of mass flux, power provided by the coating, vapor quality, pressure and heat transfer coefficient.



**Fig. 33. Simulation of the power distribution in a portion of the test section including the heater and two parts of uncoated glass. The importance of axial conduction can be noticed.**

A special attention has been given to the local value of the power, resulting from considering not just the conduction in the radial direction and the losses for radiation, but also the axial conduction in the glass tube.

In particular, the first model simulates the global behavior of one heater and two parts of tube on both the sides of the ITO layer, and the results are present in Fig. 33. The values of the power at each node are plotted as function of the axial coordinate  $z$ , and  $z=0$  represents a point which is 15 mm before a heater. The total length of the test section simulated is 60 mm; the heater is 30 mm long and is in the middle of the model (from  $z=15$  mm to  $z=45$  mm), while the 15 mm of tube remaining for each side are uncoated glass tube.

This model gives an idea of what is the global heat transfer behavior of one heater and of its surroundings.

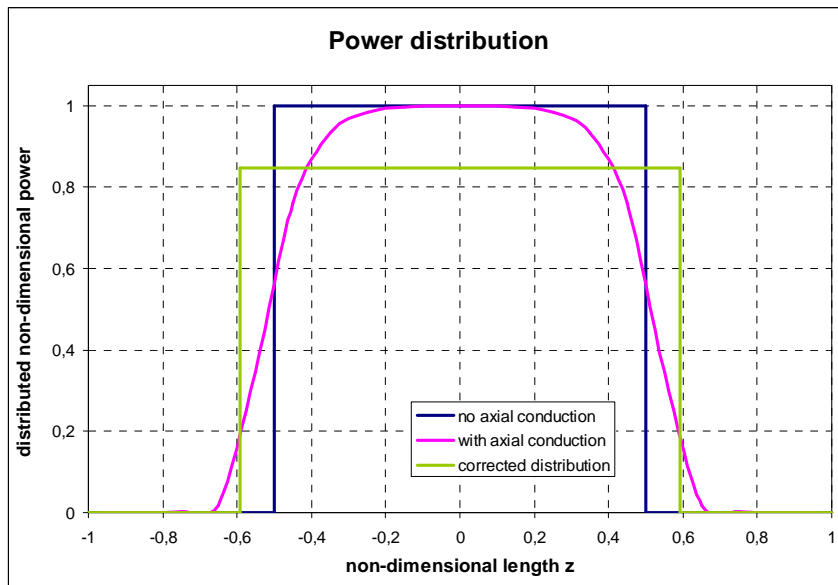
The second model analyses more deeply the heat transfer phenomena at the boundary between the heater and the uncoated glass, which will increase its temperature according to axial conduction.

The axial coordinate  $z$  represents the distance on the tube, and the modeling window is

focused on the boundary between a heater and the uncoated glass tube after this. The total length considered is of 20 mm, being from  $z=0$  to  $z=10$  mm the ITO heater part and from  $z=10$  to  $z=20$  mm the unheated tube. The images of the parts of the test section which have been discretized are presented in Fig. 33 and Fig. 34.

As can be seen from the power trend of Fig. 33, the power is almost constant inside all the heater, and at its extremes there is the most visible effect of axial conduction.

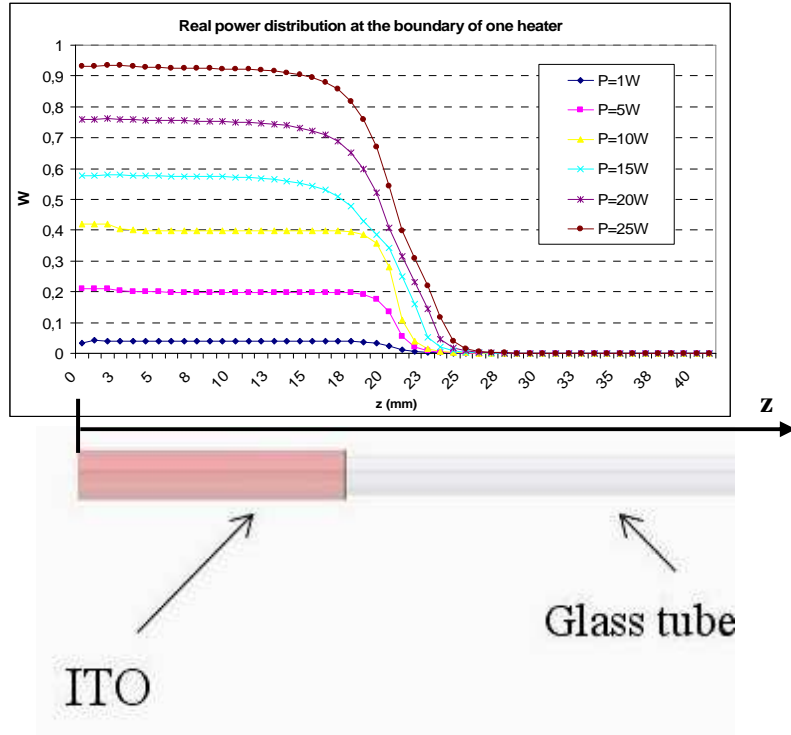
The most important effect of this heat transfer phenomena is that the real heat exchange area is different from that of the heater, with a consequential difference between the nominal and real heat flux on the inner surface of the tube.



**Fig. 34.** Comparison with the power given to the flow in each node, in the ideal case without axial conduction, with axial conduction and with the 99% value of total power that allows to define the new equivalent length of the heater. The axial coordinate  $z$  is made non dimensional referring to the heater length as unit.

Fig. 33 and Fig. 35 permit the quantification of this difference: a new equivalent coating length can be defined as the one where 99% of the total power is transferred to the flow.

Tab. 1 and Fig. 36 show graphically the trend of the power without the equivalent length, with the introduction of this corrective factor and with the threshold fixed to find it.



**Fig. 35. Simulation of the power distribution at the end of a ITO heater with different heat provided.**

Fig. 36 shows clearly the almost linear behavior of the increment of the real heating length according to the increasing of the power provided to the heater. This last result will be introduced in the global calculation model of the test section, in order to consider for each value of power the correct heat exchange area, in order to consider the phenomena taking place inside the tube associated to the correct value of heat flux.

## 5.2. Conclusions

In this section the test section has been analyzed from all the different heat transfer mode, conduction, convection and radiation. A description of all the heat flux present around one heater has been reported and a detailed numerical analysis has been conducted to estimate the axial conduction along the tube.

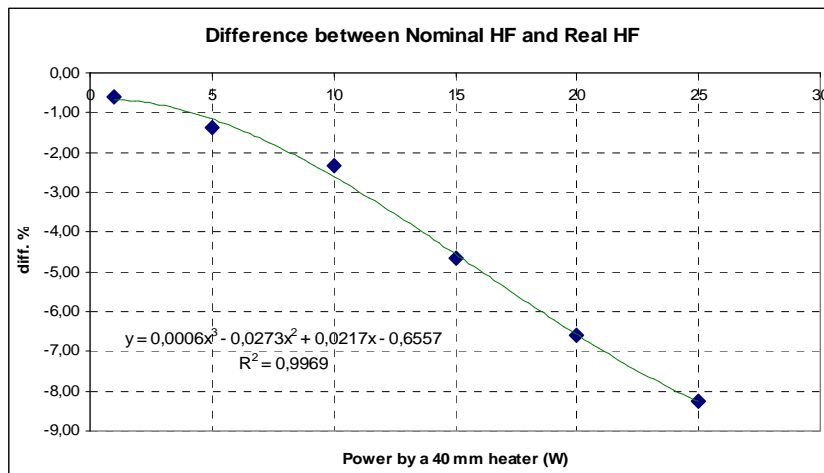
While all the other contribution can be evaluated arithmetically, this procedure is very complicated for the axial conduction, which changes the real exchange area between the coating and the flow.

Power	NOMINAL heater length	Real heat flux length	NOMINAL HF	Real HF	diff % (respect real HF)
W	mm	mm	W/m <sup>2</sup>	W/m <sup>2</sup>	%
1,00	40	40,43	1983,4	1962,4	-1,06
5,02	40	41,49	9985,1	9625,3	-3,60
8,69	40	42,97	17293,8	16099,4	-6,91
13,56	40	44,66	26982,8	24169,1	-10,43
17,20	40	45,83	34244,0	29890,0	-12,71
21,00	40	46,40	41793,0	36031,4	-13,79

**Tab. 1. Comparison between nominal and real heat flux for a 40 mm long heater with different value of power provided.**

This problem has been solved with the creation of two numerical models that are able to simulate the complete heat transfer behavior of one heater and the specific axial conduction phenomena at the boundary of the ITO layer. This permitted to define a new equivalent length of the coating according to the amount of power provided by the heater.

Together with this simulations, the first test with the new apparatus have been carried out in order to check the functionality of the instrumentation and the acquisition system.



**Fig. 36. Percentage difference between real and nominal heat flux at various value of power provided.**

## 6. MEASUREMENTS AND ACCURACY OF THE MAIN PHYSICAL QUANTITIES

### 6.1. Data measured

During the experiments several data are acquired from the test rig. In the following a list of these quantity will be presented together with a brief description of the calculation to obtain each of them.

#### 6.1.1. Pressure drop

The two-phase pressure drop across the diabatic test section is measured by a differential pressure transducer based on a piezoresistive stainless steel sensor. It can be applied on both sides with fluids and gases compatible with stainless steel and can measure pressure drops between 0 and 5 bar.

#### 6.1.2. Refrigerant thermodynamic data

The saturation temperature of the refrigerant  $T_{sat}$  is directly evaluated at the inlet of the diabatic part of the test section. The thermodynamic properties are obtained from the standard databases.

#### 6.1.3. Heat flux

The heat flux provided to the flow can be calculated as:

$$q = \frac{Q}{\pi D_{in} L_{ITO}} \quad (6.1)$$

where  $q$  is the heat flux,  $Q$  is the power entering the test section,  $L_{ITO}$  is the coating length and  $D_{in}$  the internal diameter of the tube.

In this expression the “real” flux going to the refrigerant is considered. Because the glass tube is vacuum isolated inside a glass chamber, there is only a radiative heat transfer between the ITO coating and the environment. These losses are calculated and subtracted to the value of pre-imposed power.

#### 6.1.4. Vapor quality

The vapor quality at the exit of the test section is calculated by an energy balance over the heaters of the test section:

$$x(z) = \frac{P_{tot}(z)}{\dot{m}_{ref} * h_{LV}(T)} \quad (6.2)$$

where  $P_{tot}(z)$  is the total electrical power provided by the heaters till the axial position  $z$ ,  $h_{LV}(T)$  is the vaporization enthalpy referred to the temperature of the fluid at the location  $z$ ,  $\dot{m}_{ref}$  is the refrigerant mass flow rate, respectively.

#### 6.1.5. Void Fraction

The cross sectional void fraction is calculated in two ways: with the homogeneous model

$$\varepsilon_{HOM} = \left[ 1 + \left( \frac{1-x}{x} \right) \left( \frac{\rho_V}{\rho_L} \right) \right] \quad (6.3)$$

and with the Steiner version of the Rouhani –Alexsson drift flux model for horizontal tubes[3]:

$$\varepsilon = \frac{x}{\rho_V} \left[ (1 + 0.12 (1 - x)) \left( \frac{x}{\rho_{V1}} + \frac{1 - x}{\rho_L} \right) + \frac{1.18 (1 - x) [g \sigma (\rho_L - \rho_V)]^{0.25}}{G \rho_L^{0.5}} \right]^{-1} \quad (6.4)$$

Where  $x$  is the vapor quality,  $\rho_V$  and  $\rho_L$  are the vapor and liquid density respectively,  $\sigma$  is the viscosity and  $G$  is the mass flux.

## 6.2. Experimental accuracies

In the next paragraph the uncertainty of all the components composing the test section and of the main measurement and data acquisition devices is reported. All the

calculation have been performed according to the error propagation method.

#### 6.2.1. Diameter of the tube

The diameter of the evaporator (D) is made of DURAN glass. At the moment the only available information is given by the product datasheet. In future the internal and external diameters will be precisely measured in order to provide a better accuracy in the experimental results.

$$D_{\text{int}} = 4 \pm 1\%$$

$$D_{\text{ext}} = 6 \pm 2\%$$

#### 6.2.2. Coating/evaporator length

The length of each coating can vary for less than one millimeter for each side. This means:

$$\Delta L_{ITO} = \pm 4\%$$

The coating length in this case is of 40 mm.

#### 6.2.3. Pressure drop

The PSE pressure transducer is used to measure the pressure at the inlet of the test section. It is connected to a National Instrument USB 6008 device.

During the experiments the pressure range is between 4 and 8 bar. This means:

$$P = 4 \text{ bar} \pm 2\%$$

$$P = 8 \text{ bar} \pm 1.25\%$$

#### 6.2.4. Mass flux

The definition of mass flux  $G$  is:

$$G = \frac{4\dot{m}}{\pi D_{\text{int}}^2}$$

where  $\dot{m}$  is the refrigerant mass flow rate.

The mass flow rate measurement accuracy is:

$$\dot{m} = 1 \text{ kg/h} \pm 6\%$$

$$\dot{m} = 5 \text{ kg/h} \pm 3\%$$

With the present configuration the mass flux ranged from 22 to 110 kg/m<sup>2</sup>s, which means that the uncertainties are:

$$G = 22 \text{ kg/m}^2\text{s} \pm 6.3\%$$

$$G = 110 \text{ kg/m}^2\text{s} \pm 3.5\%$$

From this point of view, it must be underlined that the actual flow meter should be substituted with a more precise one, in order to drastically reduce the uncertainties on the mass flow rate measurement.

#### 6.2.5. Temperature

All the thermocouples are K-type (Chromel-Alumel) and come from the Research center ENEA. They are connected to a Agilent acquisition system and they were calibrated to have an absolute error of 0.4%/°C. Being the range of fluid temperatures in experiments between 10 and 30°C, it is possible to conclude that:

$$\Delta T = \pm 0.1^\circ\text{C}$$

#### 6.2.6. Power supply

The electrical power supplied to the ITO coating is calculated from the measured value of voltage and current:

$$P_{ITO} = V_{ITO} I_{ITO}$$

As  $\Delta V/V = \pm 0.28\%$  and  $\Delta I/I = \pm 0.87\%$ , it results:

$$\Delta P_{ITO} = \pm 0.91\% P_{ITO}$$

#### 6.2.7. Heat flux

The contribution of the power, diameter and the coating length are  $\pm 0.91$ ,  $\pm 2\%$  and  $\pm 4\%$ , respectively.

Heat fluxes ranges from 2 to 40 W/m<sup>2</sup> K. The resulting uncertainties are:

$$q = 2 \text{ kW/m}^2 \pm 4.6\%$$
$$q = 40 \text{ kW/m}^2 \pm 4.6\%$$

The vapor quality is calculated at the outlet of a certain evaporator corresponding to the z axial position.

Considering for example a T<sub>ref</sub> of 20°C (at which h<sub>LV</sub>=182kJ/kg) and a total power of 20 W, the result is:

$$x(z) = 0.395 \pm 6.1\% \quad \text{at } \dot{m} = 1 \text{ kg/h}$$
$$x(z) = 0.079 \pm 3.1\% \quad \text{at } \dot{m} = 5 \text{ kg/h}$$

### 6.3. Conclusions

A complete analysis of the accuracy characteristics of each instrument of the test section has been conducted. It is possible to affirm that the results coming from the test section present a good accuracy, and that in the future there will be an improvement of the part that present a higher level of possible error.

## 7. IMAGE ANALYSIS TECHNIQUE

In this chapter the basic concept of image analysis will be presented, together with the automatic flow pattern identification method based on image processing.

### 7.1. Introduction to image analysis

To reach such results, a predominant role is played by image processing. In the following a brief description of what is an image and which are the ways in which an image can be analyzed is reported.

An image is a visual representation of an object or group of objects. Image processing manipulates information within an image to make it more useful. Digital image processing is a specific type of image processing performed with a computer.

People are probably most familiar with photographic images; however, photographic images do not lend themselves to computer analysis because computers work with numerical rather than pictorial information. In order to process an image with a computer, the image must be converted into numeric form. This process is known as image digitization.

#### 7.1.1. Image digitisation

The digitization process divides an image into a horizontal grid, or array, of very small regions called "picture elements," or "pixels".

In the computer, the image is represented by this digital grid, or bitmap. Each pixel in the bitmap is identified by its position in the grid, as referenced by its row (x) and column (y) number. By convention, pixels are referenced from the upper-left position of the bitmap, which is considered position 0,0 (row 0, column 0).

When a source image, such as a photograph, is digitized, it is examined in grid fashion. That is, each pixel in the image is individually sampled, and its brightness is measured and quantified. This measurement results in a value for the pixel, usually an integer, which represents the brightness or darkness of the image at that point. This value is stored in the corresponding pixel of the computer's image bitmap.

When the image is digitized, the width and height of the array are chosen and fixed. Together, the bitmap's pixel width and height are known as its spatial resolution.

#### 7.1.2. Pixel depth

Depending upon the capability of the measuring hardware and the complexity of the image, anywhere from 1 to 32 bits might be used to store each pixel value.

Pixel values for line art images, which contain only black and white information, can be easily represented by a single bit: 0=black, 1=white.

However, a photographic-like image contains much more information...it takes 24 bits to represent all the possible colours that might occur in a true colour image. Given 24 bits, over 16 million colours, far more than the human eye can differentiate, can be represented.

The number of bits used to represent the pixel values in an image is referred to as its pixel depth, or bits-per-pixel (BPP). The number of bits per pixel used to represent each pixel value determines the image's class.

### 7.1.3. Image-Pro® Plus 4.5.1

Image-Pro® Plus 4.5.1 is a powerful scientific image analysis software package that combines the latest tools for scientific and industrial image analysis into one intuitive software.

Image-Pro Plus has many tools that allows the user to operate many operations on the images or the video that are under process.

A wide set of specialized *filters* and *operators* can provide image enhancement. These include a wide variety of edge and detail enhancement strategies, ways of separating structures through *erosion* and *segmentation* so that they can be counted and methods for subtracting uneven backgrounds from images. *Fast Fourier Transformations* (FFT) can remove repetitive patterns that obscure image information. *colorization* allows manipulation of the pixel intensity level to convert the different shades of grey of a black & white image to false colours with, for example, dark grey becoming blue and light grey becoming red.

The *calibrate* button allows the correct calibration to be selected for the image's scale or magnification. The calibration is set via the dialogue at *measure/calibrate/spatial*. *Count and measure* allows automated gathering of data with specified parameters and manual *measurement* allows individual manual measurements to be made.

The measurement tool box has tools for analyzing and obtaining quantitative information from the images. These information regard the selection, deletion, deletion of all, point, line, circle, rectangle, polygon, trace, best fit line, best fit circle, best fit arc, distance between, angle, angle between features, horizontal thickness, vertical thickness and curve thickness. The use of each will allow capture of a variety of data which can later be edited to that which is relevant. When a tool is selected you will be prompted as to how to click in the image to make each measurement.

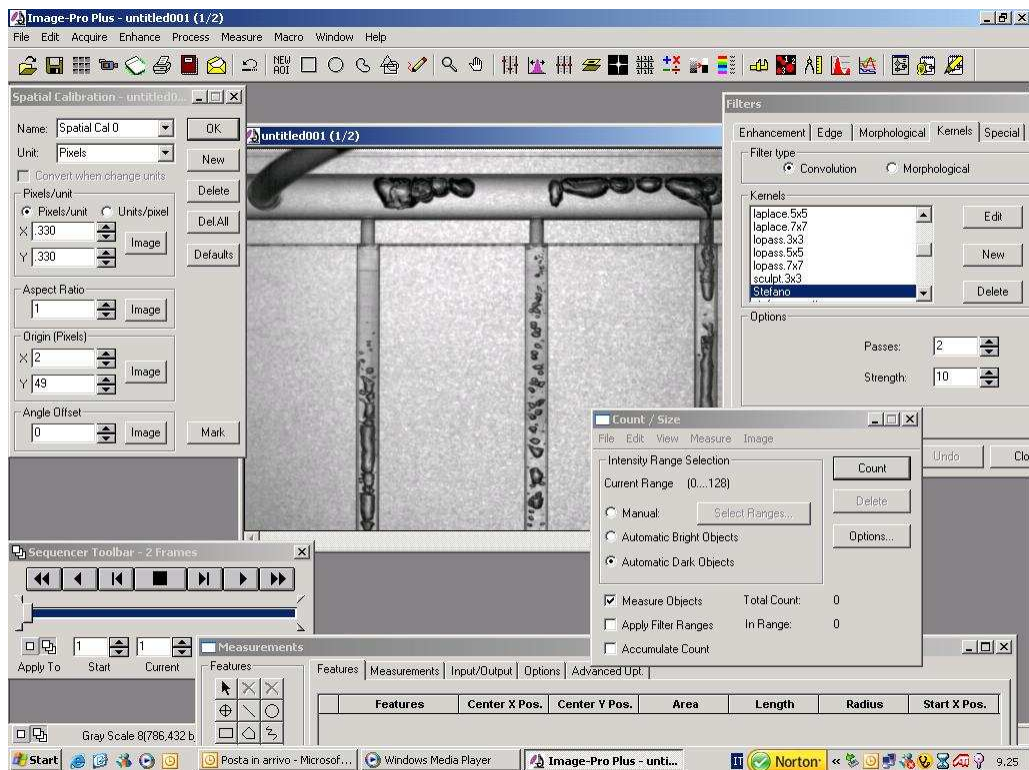


Fig. 37. Image-Pro® Plus 4.5.1 usual working window.

As each measurement is made it will be labelled within the image and the result will appear on the *measurement* tab. When finished, these can then be exported to a spreadsheet or stats program via the *input/output* tab. An image of the normal working window is reported in Fig. 37.

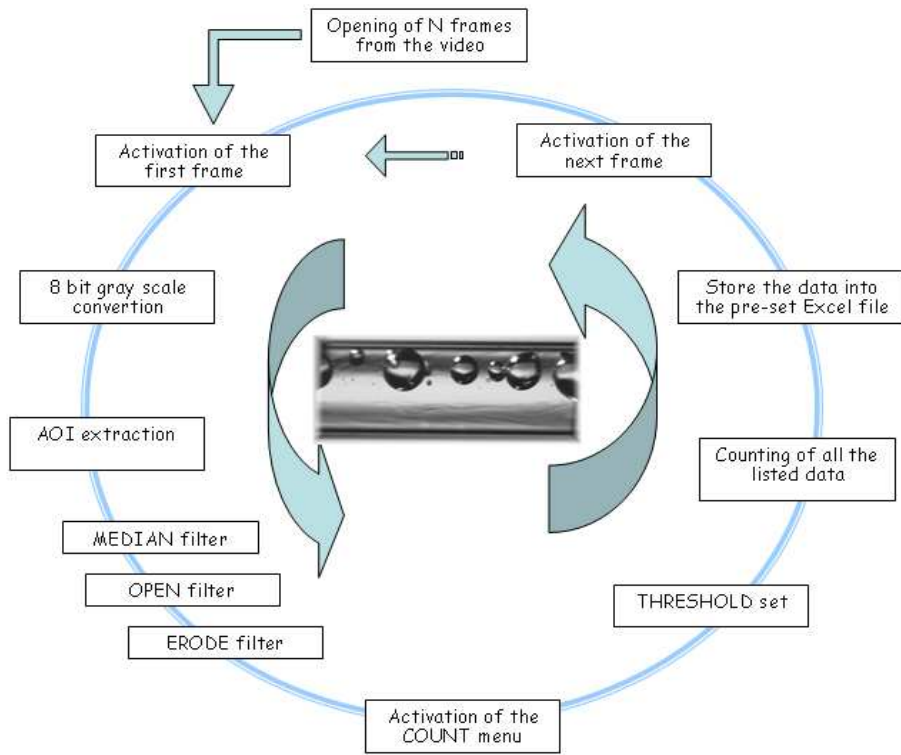
#### 7.1.4. Main steps of the automated bubble recognition routine

Several routines were developed within the commercial software to automatically perform the image analysis of a selected number of frames from a recorded movie, and to give as a final result many geometrical and statistical information about the identified bubbles and the two-phase flow pattern.

The main routine steps are shown in Fig. 38 and Fig. 39 and can be summarized as follows: starting from a number of frames selected by the user and taken from a video sequence, the routine analyzes each of the frame, it stores the measured data to a pre-structured file, and then it gives the final output by identifying the most probable flow pattern of the recorded images.

Before running the routine, a spatial calibration is run.

For each frame an “area of interest” preselected by the user is extracted and only this area is then converted in a 8 bit gray scale mode.



**Fig. 38. Cyclic procedure to perform the flow pattern identification of several images.**

The next step consists in the application respectively of the median, open and erode filters, that are necessary to clean and uniform the image and to better define the bubble contours.

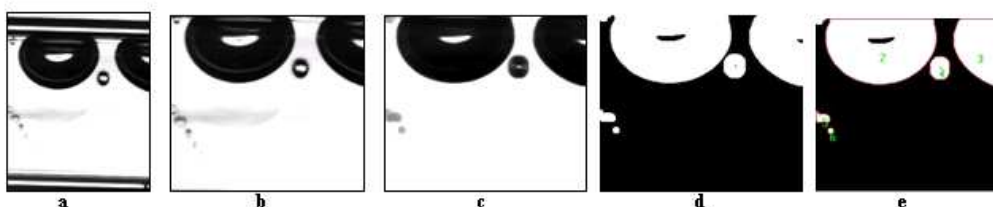
These filters can be applied more than once according to the input image and the final result that will be obtained.

Then a threshold on the gray level of the images is preset to decide whether an area must be included in the measuring procedure or not.

The main geometrical data of the objects identified in the active window such as bubbles diameter, area and main axis lengths are successively collected and stored for post-processing purposes in text files as the one shown in Fig. 40. After one frame is analyzed the program activates the next frame and the same procedure is repeated. There is no limitation in the number of frames that can be processed.

The complete procedure for the analysis is schematically represented in Fig. 38.

To show the operations performed on an image, a real case is reported in Fig. 39.



**Fig. 39. Effect of the automatic image analysis steps visible in a frame.**

From the input image (a), not so smooth and with some parts to be neglected, the area of interest (b) is extracted, then it follows the image cleaning (c) and the final step of the data acquisition (d and e).

The data file obtained at the end of the procedure contains numerical data like the ratio between the maximum and the minimum radius of each bubble, the length of the main axis of the ellipse equivalent to the bubble, the area of each bubble, the longest calliper length of the bubbles and the ratio between the area of the bubble to that of the entire area of the image.

	N° of bubbles	Area of each bubble	$R_{max}/R_{min}$		2D void fraction for the single object
1	2.919294	2.666281	2.586543	2.356730	.1196006
1	2.945290	2.696998	2.620101	2.387418	.1206656
1	2.972536	2.733435	2.608292	2.424927	.1217819
1	2.995282	2.767256	2.629719	2.444818	.1227138
1	3.023028	2.797520	2.652386	2.472711	.1238505
1	3.042025	2.822340	2.701131	2.486770	.1246288
1	3.075020	2.857416	2.641621	2.536848	.1259805
1	3.091767	2.882466	2.687726	2.582922	.1266667
1	3.102515	2.891459	2.703952	2.605225	.1271070
1	3.089517	2.871092	2.678643	2.550047	.1265745
1	3.096516	2.87160	2.678643	2.566394	.1268612
1	3.097516	2.869041	2.678970	2.543918	.1269022
1	3.093517	2.865501	2.675842	2.536144	.1267384
1	3.093517	2.868602	2.672664	2.544304	.1267384
1	3.085768	2.866891	2.672664	2.547669	.1264209
1	3.090267	2.872262	2.688470	2.546096	.1266052
1	3.090267	2.876303	2.688470	2.572674	.1266052
2	.0162474	.3132697	.3003929	6.989127	.0006656
1	3.079269	2.870673	2.688144	2.579874	.1261546
2	.0474925	.5905639	.5375452	7.915699	.0019457
1	3.075270	2.865569	2.678643	2.558722	.1259908

**Fig. 40. Example of datasheet obtained from the image analysis of one video.**

The number of frames taken into account in the analysis is chosen a priori according to the final statistic needed and to the number of available frames. In the present case, after some tests of reliability and repeatability of the results, a number of 500 frames for each movie was chosen.

### 7.1.5. Mathematical processing of the bubbles geometrical features

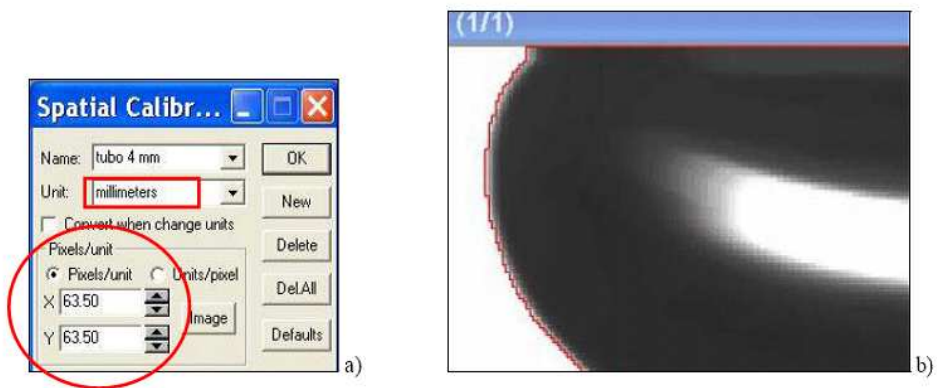
The data files obtained by the application of the previous procedure need to be processed to extract the parameters that will be at the basis of the flow regime classification. The statistical classification is based on three main bubbles characteristics: the mean diameter of each bubble, the 2D void fraction of each frame and the  $\tau$ , which is an index of the elongation of the bubble .

Considering all the data coming from the experiments and referring to one of the already mentioned bubble characteristic it was possible to obtain a large database containing data on bubble diameters, number of bubbles and 2D void fraction for each frame, supported by more than 100000 images.

Such a huge amount of frames was necessary because of the probabilistic nature of the flow pattern identification procedure.

## 7.2. Error in the bubble identification process

In the bubble identification process it is possible to commit an error because a threshold on the gray level must be set to identify the contour.



**Fig. 41.** a) relationship between pixels and the unit length; b) zoom on the bubble contour during the segmentation process in order to find the relative error of the area measurement.

Setting the threshold for the bubble area recognition first to the value of the darker limit and then to the higher value that allow the detection, it was possible to evaluate the error for the area identification of each bubble. The inaccuracy was found to be around 1%, and the small magnitude of this value is mainly due to the fact that the grey scale level changes at the borders of the bubble, while remains constant in its remaining area (Fig. 41).

### 7.3. Parameters considered for the flow pattern identification

To study the flow patterns and to obtain the automatic flow pattern identification, some parameters were chosen and their rule in the flow pattern classification was tested.

These parameters are all geometrical features of the bubbles present in the video analyzed, and they are mainly three.

First of all the theoretical bubble diameter. It is obtained from the bubble area, supposing that each bubble has a spherical shape. This hypothesis is sometimes very far from what happens in reality, but it is a good index to compare the bubble between each other. This value is obtained for all the bubbles of one video as

$$D_i = \sqrt{\frac{4A_i}{\pi}} \quad (7.1)$$

Where  $D_i$  is the single bubble diameter and  $A_i$  is the single object area.

The second parameter is the 2D void fraction. One of the geometrical data coming directly from the image processing is the percentage of area occupied by the single bubble over the total visualization window area. This value is calculated for all the single bubble of one frame, and then the global value of 2D void fraction for one frame is obtained automatically.

This is an important value that is an index of what is the magnitude of the occupation of the visualization window area by the gas phase.

The last value,  $\tau$ , is a parameter related to the shape of each bubble, meaning that it gives an idea of how far the bubble is from the spherical shape. This value is obtained considering the ratio between the maximum and minimum diameter for each object, value recorded by the automatic routine.

If

$$\beta = \frac{R_{\max}}{R_{\min}} \quad (7.2)$$

then

$$\tau = \frac{D_{\max} - D_{\min}}{D_{\max}} = \frac{\beta - 1}{\beta} \quad (7.3)$$

where  $R$  and  $D$  are one dimension of the bubble.

Having defined  $\tau$  in this way, it means that when its value is closed to zero the shape of the bubble is very close to the spherical one, while for bigger values, the shape tends to be more and more elongated. This parameter, for example, is very useful to classify the elongated bubble regime according to the magnitude of the distortion of the bubbles (which is proportional to  $\tau$ ).

This value is calculated for each bubble of each frame of the videos.

#### **7.4. Automatic flow pattern identification**

One of the novelty of this work is the attempt to obtain a method that is able to provide an objective and automated way to perform the flow pattern characterisation of a two phase flow. This method has flow visualization and two phase flow image recording has the key elements.

##### **7.4.1. Identification criteria**

The approach to the flow pattern identification that has been followed in this article is different, for example, from the one adopted by [38] where the classification was mainly based on the deformation of a black lines mask positioned on the test section tube.

Such method may not be completely objective, since there was a different approach in the investigation according to the macroscopic features of the analysed flow pattern. In the present case, the discriminating criteria are both based on the physical characteristics of the flow regime and on statistical features.

It must be underlined that the statistics comes only as an help in the flow pattern classification, because the main discriminating criteria is the physical characteristics.

A criterion based on the mean or nominal diameter of each bubble (calculated from the bubble area), on the number of bubbles contained in each frame and on the 2D void fraction of each frame can be objective and useful in the flow pattern identification, together with the help of some statistical properties that allow (and justify) the distinction between two different flow patterns.

##### **7.4.2. Statistical tools to operate and validate flow pattern identification**

This paragraph reports about a method that allows the flow pattern identification and about the procedure that will be used for all the three discriminating parameters. As an example, in order to explain the procedure, the diameter of a single bubble is considered as discerning parameter, but the steps followed are the same both for the single frame number of objects and the single frame 2D void fraction.

The equivalent (or nominal) diameter of each bubble contained in one frame is defined as:

$$D_i = \sqrt{\frac{4A_i}{\pi}} \quad (7.4)$$

where  $D_i$  is the diameter of the  $i$ -th bubble,  $A_i$  is the area of the  $i$ -th bubble. Then it is possible to evaluate the mean and the variance of  $D_i$  in one movie as:

$$\bar{D} = \frac{1}{N} \sum_{i=1}^N D_i \quad (7.5)$$

$$\sigma^2 = \frac{1}{N-1} \sum_{i=1}^N (D_i - \bar{D})^2 \quad (7.6)$$

where  $\bar{D}$  is the mean diameter of the bubbles in a movie,  $N$  is the total number of bubbles in the chosen 500 frames and  $\sigma^2$  is the variance. The difference from two regimes is defined by the different values of  $\bar{D}$ , and the value of  $\sigma$  allows the calculation of the standard error of the mean (indicated as SEM)

$$\sigma_M = \frac{\sigma}{\sqrt{N}} \quad (7.7)$$

This parameter allows to evaluate the reliability of the method from the point of view of the flow pattern identification capacity and of the transitory periods by means of the 3D criterium.

It must be underlined that in this work the flow pattern identification and transition will be studied mainly from the graphical point of view. The recognition steps will be based on the observation of the trends of the physical parameters mentioned before and by the application of the statistical tools presented.

## 7.5. Conclusions

In this chapter a complete description of the image processing technique used to identify the flow patterns has been presented. The procedure starts from the analysis of

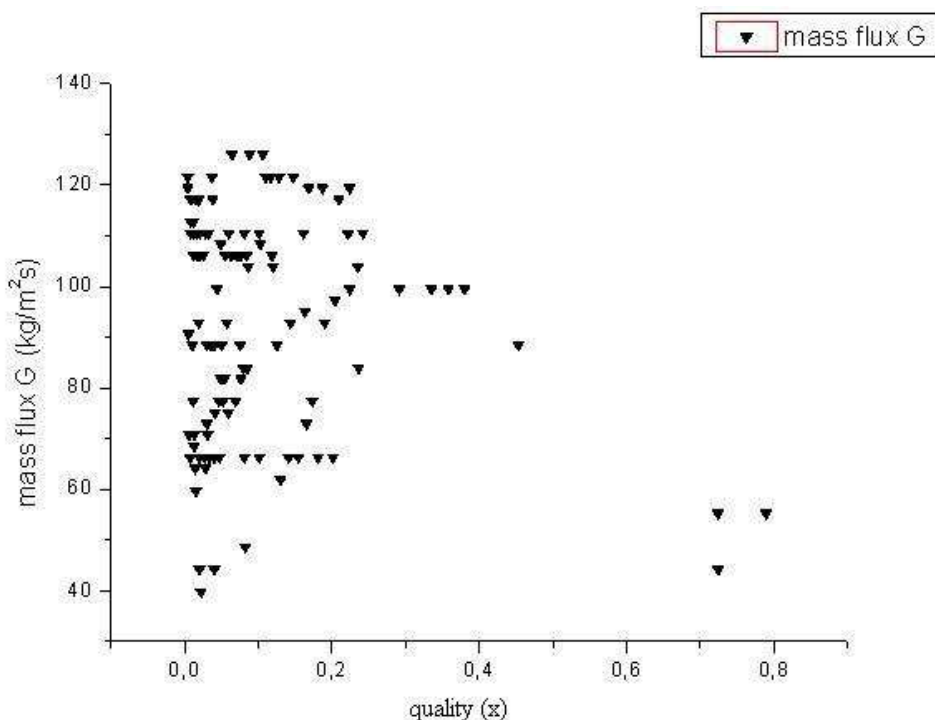
each frame of each video considered, from which an automated procedure inside a commercial code extracts the main geometrical characteristics of each bubble. Then, according to the statistical behaviour of these features, the flow pattern and the transition zones can be identified and studied.

## 8. EXPERIMENTS PERFORMED

To check the reliability of the results obtained from the acquisition system, some preliminary tests were run. After this, two experimental sets were performed to apply the image analysis based automatic flow pattern identification.

### 8.1. First group

The first part of the experiments regarded the vapor quality between 0 and 0.8, with a deeper focus between 0 and 0.4. Seven mass fluxes have been considered, from 20 to 120 kg/m<sup>2</sup>s, and in some experiments more than one heater has been turned on to reach the total power to the fluid. This is because in the present configuration, each heater is able to provide to the fluid a maximum power of 20 W. In the Fig. 42 all the points analyzed are represented in the mass flux-vapor quality.



**Fig. 42.** Vapor quality-mass flux graph to show the thermodynamic characteristics of the experiments performed in the first group.

Around 120 videos and 60000 frames were analyzed, and the frames refer to the adiabatic part of the test section in the middle of two heaters. the recording position along the axial dimension of the tube varies from video to video according to the total power provided to the flow. The aim of the experimental campaign was to analyze an important amount of frames to set which of the geometrical bubble characteristics is more suitable and reliable for the flow pattern identification, and observe their trend.

## 8.2. Second group

The second part of the experiments was focused on the bubbly flow regime (vapor quality between 0 and 0.025).

This choice is due to the fact that the incipient boiling/bubbly flow region (compared to the elongated bubble and to the stratified flow regimes, Fig. 43) is the most interesting both from the visualization and the heat transfer coefficient, having from this point of view the highest value compared to the other regimes.

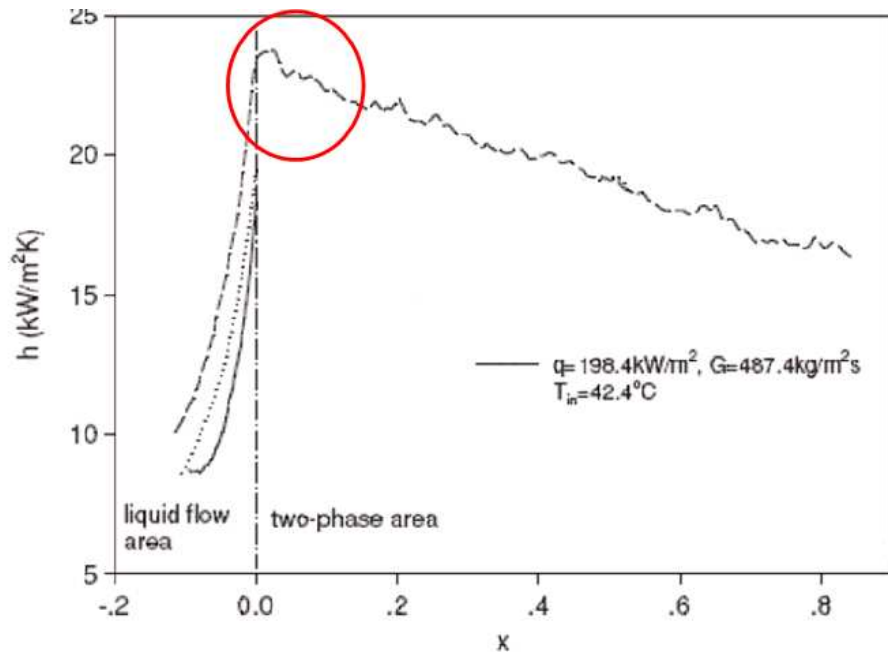
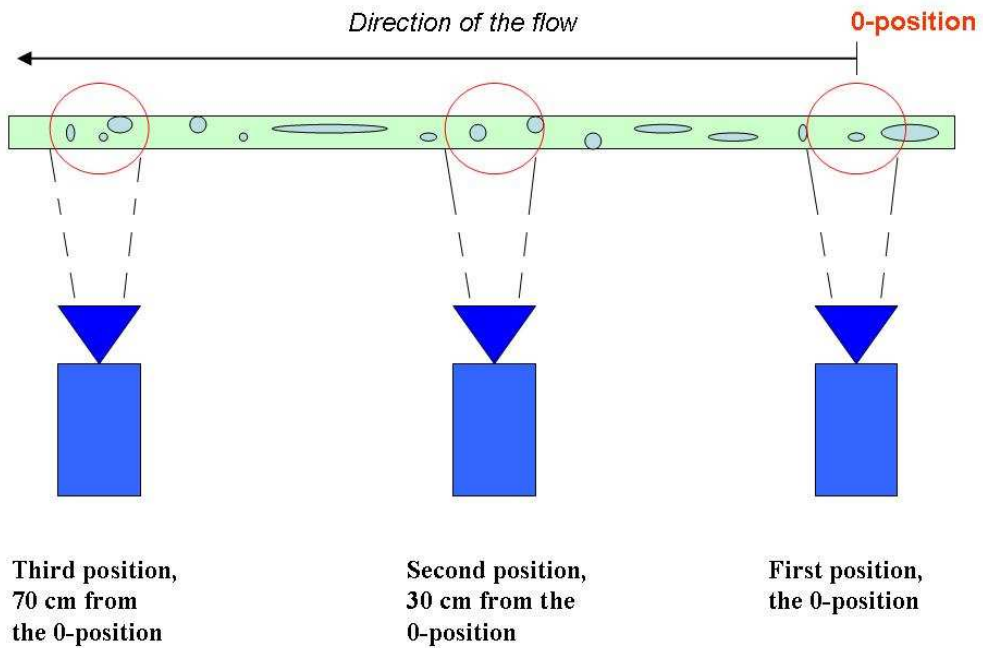


Fig. 43. Convective heat transfer coefficient as a function of the vapour quality.

Actually, not many scientific data exist in the literature for the incipient boiling, and no one from the visualization side. For this, the experiments performed within this thesis will be likely the first to consider the boiling inside a complete transparent test section, allowing the visualization of all the incipient boiling phenomena.

In this group of experiments, the videos with the same test section inlet characteristics were recorded in three different position of the tube as shown in Fig. 44: after the first heater, in the middle of the glass tube (around 30 cm ahead) and close to outlet of the glass channel (70 cm ahead). This way to conduct experiments was chosen in order to study the evolution of the flow pattern and the flow pattern transition along the tube.



**Fig. 44. Three position along the tube at which the video to study the evolution of the flow pattern have been recorded.**

The phenomena that governs this evolution is the coalescence of the bubbles, for which there are not specific visualization studies. The flows were studied with the focus on the same parameter as in the previous experimental campaign.

## 9. RESULTS

In this chapter the results of the two groups of experiments performed will be presented and explained. A series of graphs reporting the relationship between the geometrical and statistical features analyzed are presented in this paragraph. By the previously described technique it was possible to give relevance both to the flow pattern transition and to the identification of the flow pattern.

For all the graphs, each point on the diagram represents one movie, and so summarises the analysis of 500 frames. In the results, the single frame void fraction, the dimensionless bubble diameter and the  $\tau$  parameter will be considered as the main flow pattern identification parameters.

Applying the statistical analysis to these graphs it was possible to perform a probabilistic flow pattern identification.

### 9.1. First group of experiments

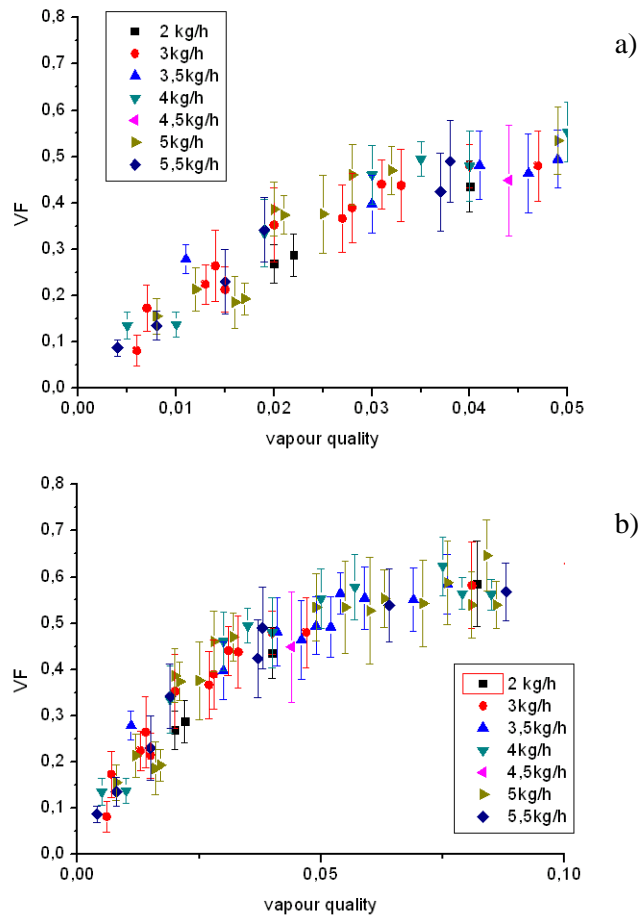
#### 9.1.1. Void fraction

The void fraction (equation 2.17) is a parameter that gives an idea of what is the percentage of the total recording window area which is occupied by the gas phase. For this reason it assumes the smallest values in the case of the bubbly flow and the highest value in the case of elongated bubble flow pattern.

In the Fig. 45 it is reported the void fraction trend as a function of the vapour quality and the flow rate.

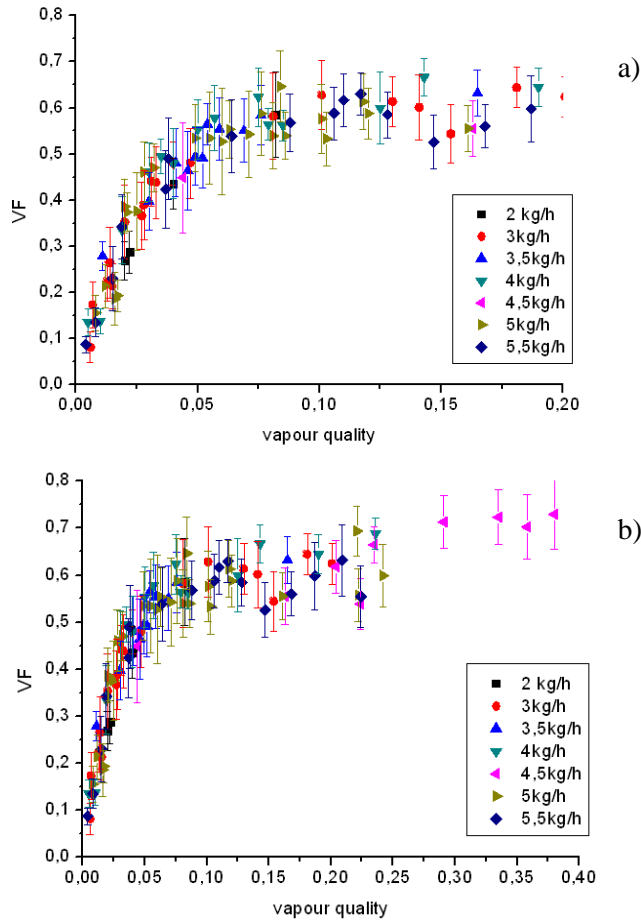
In the Fig. 45 and Fig. 46 there is a step by step enlargement of the view to have a more clear idea of what is happening at the lowest vapour quality, where the biggest changing are taking place. Together with the absolute values of the void fraction, it is reported the standard deviation for each point. This statistical tool is useful to study the transition and the stability of the flow pattern considering the oscillation of the bubble geometrical features studied.

A relatively higher value of the standard deviation is a signal of the transition of a flow pattern, an is a clear index that the point considered is in a transition zone.



**Fig. 45. Void Fraction as a function of the vapour quality and the mass flux. Fluid: R134a,  $D=4\text{mm}$ ,  $T_{\text{sat}}=22^\circ\text{C}$ ,  $G=20-120\text{ kg/m}^2\text{ s}$ .**

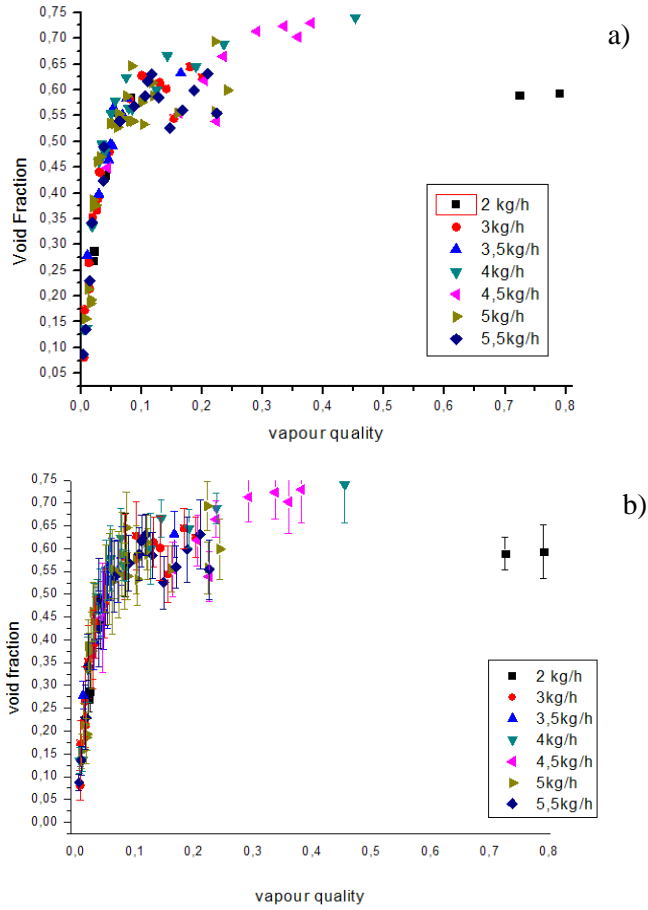
Considering Fig. 45 passing from the image a to b it is possible to see that at the lowest values of the vapour quality the void fraction assumes its minimum values. In particular in Fig. 45 a it is possible to see that these value are very stable, as can be seen from the standard deviation trend, and this means that the bubbly flow is well established for such value of flow rate and vapour quality.



**Fig. 46. Void Fraction as a function of the vapour quality and the mass flux. Fluid: R134a,  $D=4\text{mm}$ ,  $T_{\text{sat}}=22^\circ\text{C}$ ,  $G=20\text{-}120\text{ kg/m}^2\text{ s}$ .**

Increasing the power given to the fluid, there is a big region of instability as can be seen in the Fig. 45 b and Fig. 46, till a vapour quality of 0.10, and after this point the mean value of the standard deviation decreases. This means that after the transition zone, the elongated bubble regime has been reached, passing through the unstable bubbly/elongated bubble region. From this point onwards the mean value of the void fraction assumes a stable value, because the bubbles are reached their maximum dimensions inside the channels. Only few data are available for the interval of vapor quality between 0.3 and 0.4, but these results seem to confirm the trend found for the smaller values of vapour quality( Fig. 47).

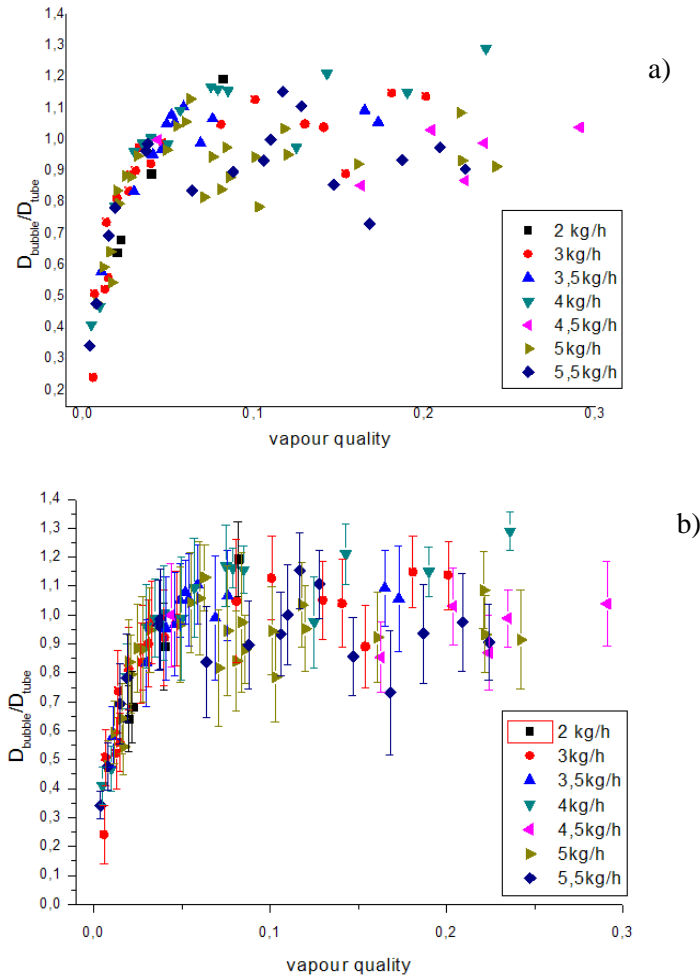
The mean void fraction seems to be independent from the flow rate, because the values reached in the different mass flux conditions are very similar to each other.



**Fig. 47. Void Fraction as a function of the vapour quality and the mass flux. Fluid: R134a,  $D=4\text{mm}$ ,  $T_{\text{sat}}=22^\circ\text{C}$ ,  $G= 20\text{-}120 \text{ kg/m}^2 \text{ s}$ .**

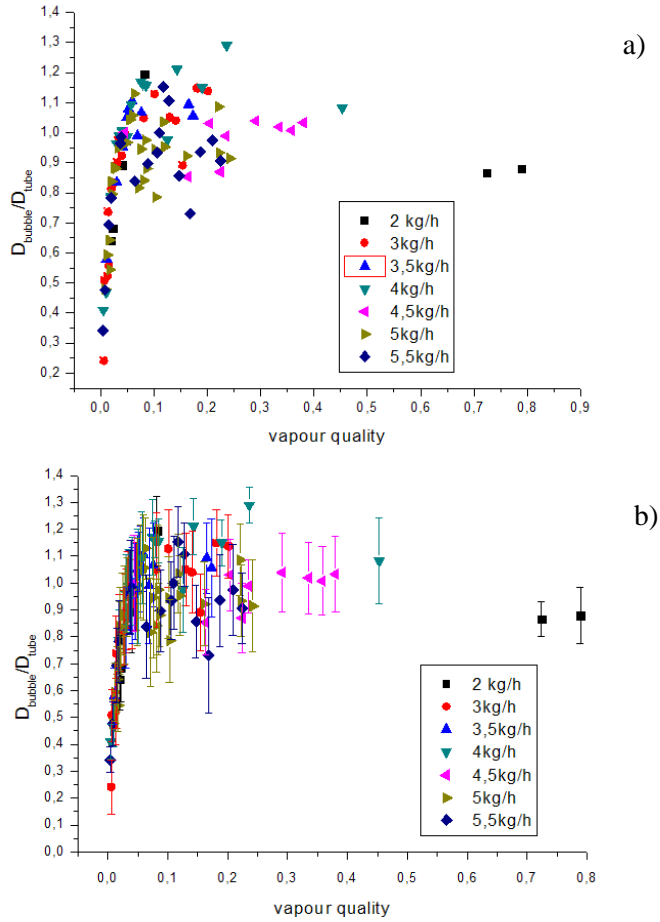
### 9.1.2. Bubble diameter

The same consideration for the void fraction are valid also in the case of the bubble diameters as function of the mass flux and of the vapour quality (Fig. 48 and Fig. 49). The results refer to the bubble diameter divided by the tube diameter, so it is possible to see the trend of the dimensionless bubbles diameter.



**Fig. 48. Dimensionless bubble diameters as a function of the vapour quality and the mass flux. Fluid: R134a,  $D=4\text{mm}$ ,  $T_{\text{sat}}=22^\circ\text{C}$ ,  $G= 20\text{-}120\text{ kg/m}^2\text{ s}$ .**

Also in this case it is possible to see the same trend found for the void fraction. The bubbly flow pattern is well established for the lowest value of the vapour quality, then there is the transition region and the final stabilization at the higher values of the bubble diameter. In this case it is not possible to see an almost asymptotic trend for the high vapour quality (Fig. 49), but the diameters remain in a spread interval around the value 1. This characteristic shows that increasing the power given to the flow there is not the possibility to find a stable and reproducible flow, because the diameters can assume a range of values.



**Fig. 49. Dimensionless bubble diameters as a function of the vapour quality and the mass flux. Fluid: R134a,  $D=4\text{mm}$ ,  $T_{sat}=22^\circ\text{C}$ ,  $G= 20\text{-}120\text{ kg/m}^2\text{ s}$ .**

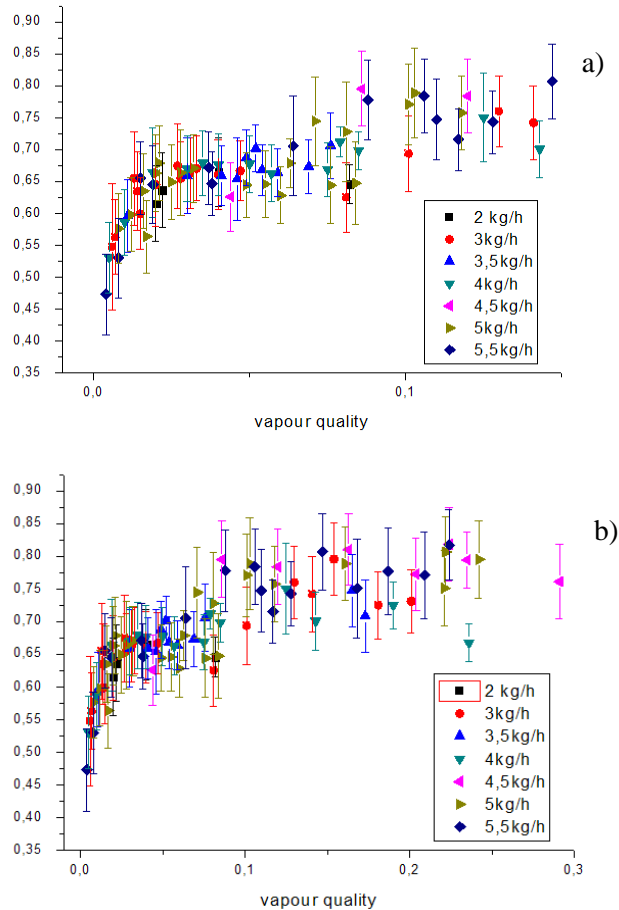
### 9.1.3. The $\tau$ parameter

The  $\tau$  parameter (equation 7.3) is an index of the shape of the bubble. In the following the same graph showed in the two previous paragraphs for the void fraction and the bubble diameter are reported.

It is immediately visible from Fig. 50 that it is almost impossible to see spherical bubbles, because in the bubbly flow pattern the value of  $\tau$  is already around 0.45. This is mainly because in this group of experiments, it has not been conducted a specific study of the bubbly flow, which requires a more detailed and deep analysis of the very low vapour quality zone.

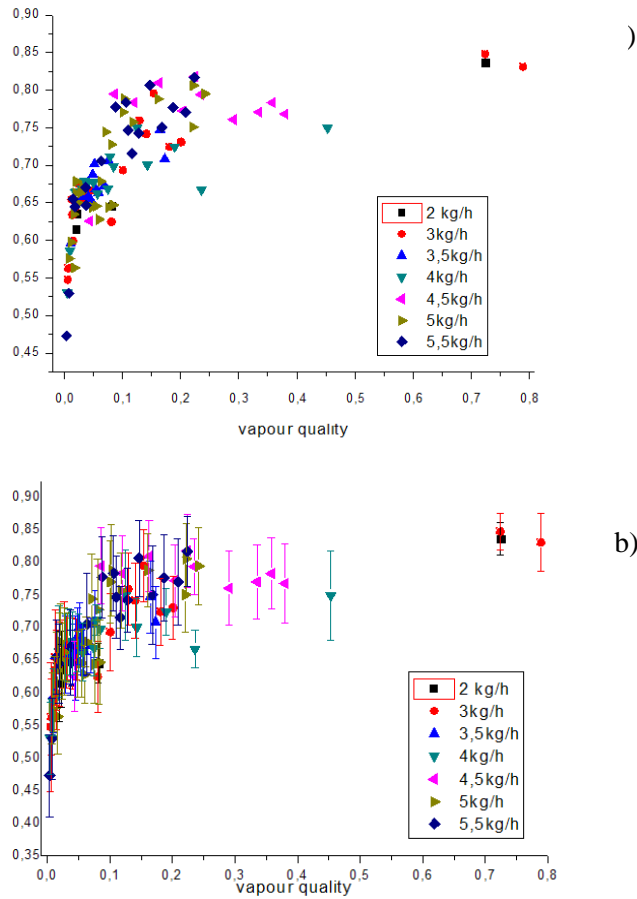
From the analysis of Fig. 50 and 51 it is possible to have once again the confirmation of what was seen for the other parameters. In particular, considering the Fig. 50 a and b, there are three main different values of the parameter  $\tau$  that are present from the total

liquid condition (vapour quality  $x=0.01$ ) to the vapour quality of 0.4. The bubbly region is well evident for very low vapour quality, even if the standard deviation is very high, meaning that the transition zone is very close.



**Fig. 50.**  $\tau$  parameter as a function of the vapour quality and the mass flux. Fluid: R134a,  $D=4\text{mm}$ ,  $T_{\text{sat}}=22^\circ\text{C}$ ,  $G=20\text{-}120\text{ kg/m}^2\text{ s}$ .

Then between vapour quality of 0.025 and 0.09 the transition zone occurs, in which the bubbles begin to be more elongated and all with the similar shape. This is the bubbly/elongated bubble transition zone. Then, at around vapour quality of 0.09 there is a very evident step in the trend of the graph, and the value of  $\tau$  becomes very similar to its asymptotic value that will be maintained till the higher power zones. Also in this case the mass flux seems not to influence the variation of the bubble shapes.

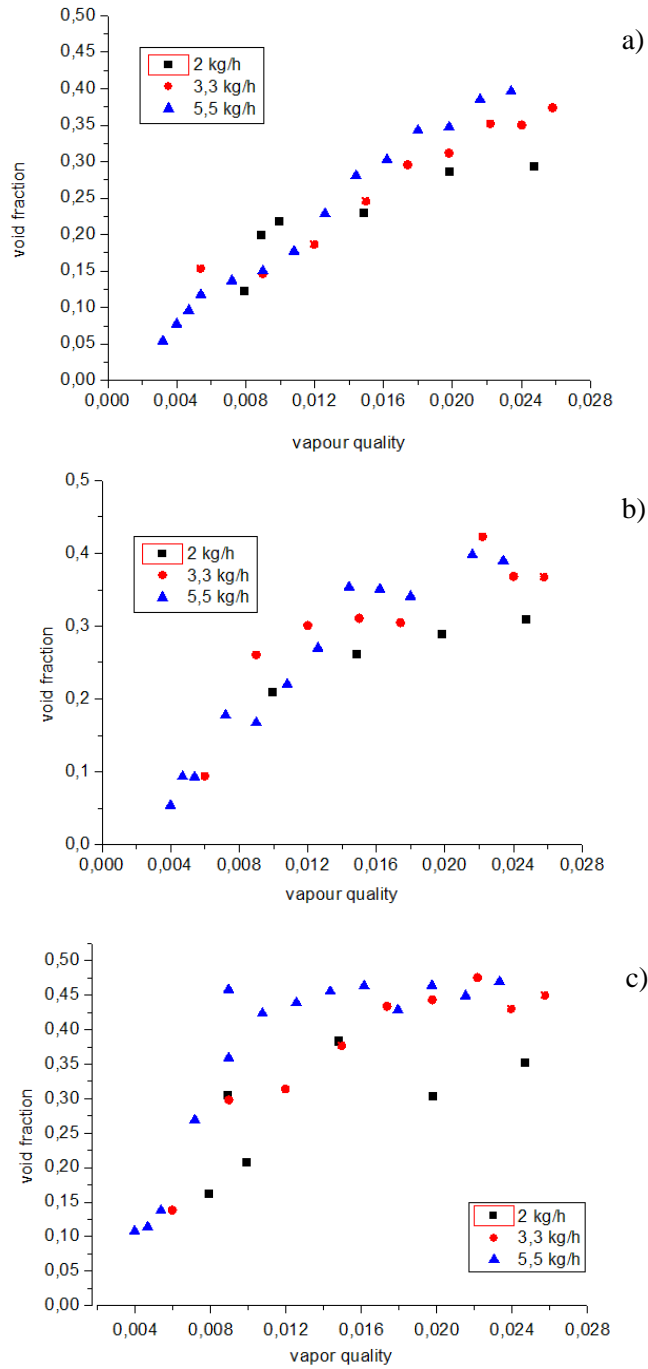


**Fig. 51.  $\tau$  parameter as a function of the vapour quality and the mass flux. Fluid: R134a,  $D=4\text{mm}$ ,  $T_{\text{sat}}=22^\circ\text{C}$ ,  $G= 20\text{-}120 \text{ kg/m}^2 \text{ s}$ .**

## 9.2. Second group of experiments

### 9.2.1. Void fraction vs vapour quality

In the following graphs the trend of the void fraction as a function of flow rate and vapour quality will be presented. For these set of experiments it is useful to compare the graph of each parameter coming from the videos taken at different position along the glass test section in order to see the evolution of the flow pattern along the tube due mainly to coalescence. In particular, three recording positions have been considered. From the Fig. 52a, it is very evident as the trend of the void fraction is not a function of the flow rate, because the three groups of value grow remaining within a very small interval. This characteristic is visible only in Fig. 52 a, which means right after the heater, while in the Fig. 52 b and c this trend is not maintained because of the coalescence of bubble and the consequent modifications of the flow patten.



**Fig. 52. Void fraction evolution along the test section tube. a) after the first heater, b) 30 cm ahead of the first position, c) 70 cm ahead of the first position.**

In the case shown in Fig. 52b, it is visible a shift in the vapour quality at which the void fraction assume the mean asymptotic values of the elongated bubble regime, which is present starting from 0.035 of vapour quality. This happens because the coalescence is beginning to play a more and more important role along the tube, and the main effect is that the bubbles are less in number but bigger in shape. It is very interesting to notice that the relative trend of the void fraction according to the mass flux remain in the same order in all the three position.

In Fig. 52 c the effect of coalescence is that the data appear very disordered, but with the same trend shown in the previous graph which is mainly maintained.

Fig. 52 c underlines that coalescence is a function of the velocity of the flow, and so the situation with the higher mass flux-and the higher fluid speed- is the one that reaches the regime condition of elongated bubble faster than the other cases. In this situation the differences between the mass flux become more important than before.

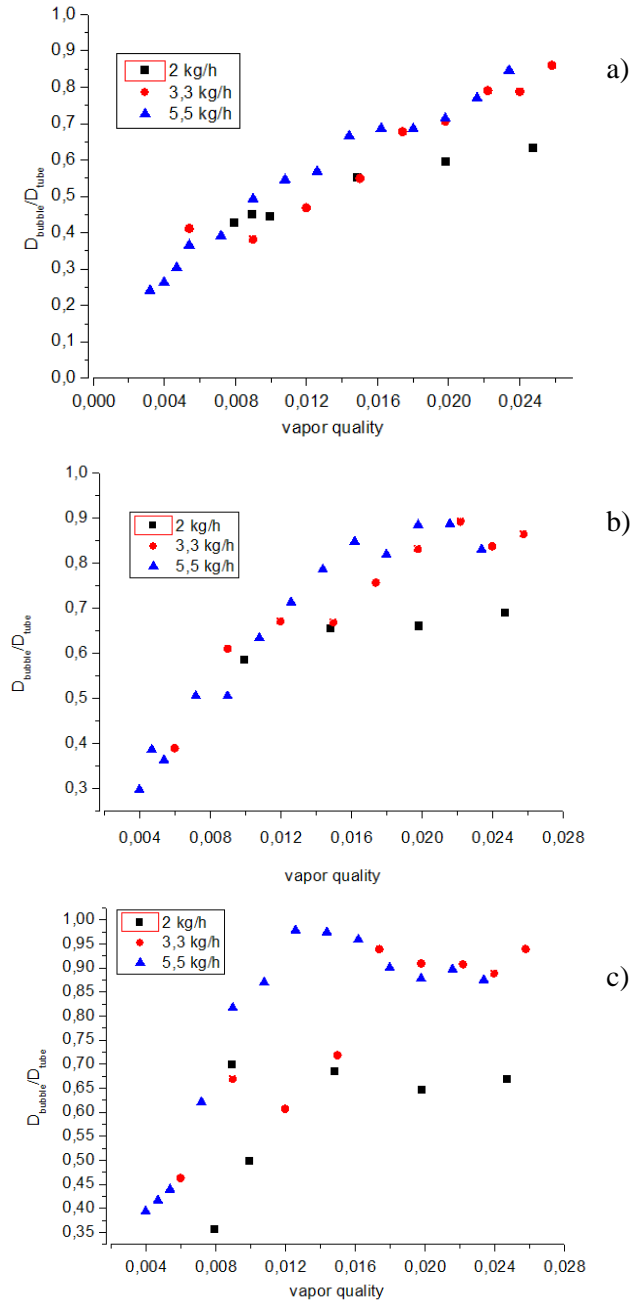
#### 9.2.2. Dimensionless Bubble diameter vs vapour quality

The trends shown in Fig. 53 a, b, c respect exactly what was said before for the void fraction. The main trends are the same and also here in the more far position from the inlet, the higher mass flux reaches before than the others the diameter value of the elongated bubble regime.

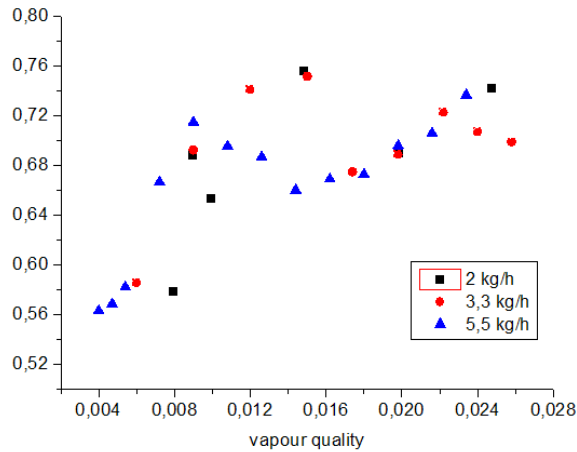
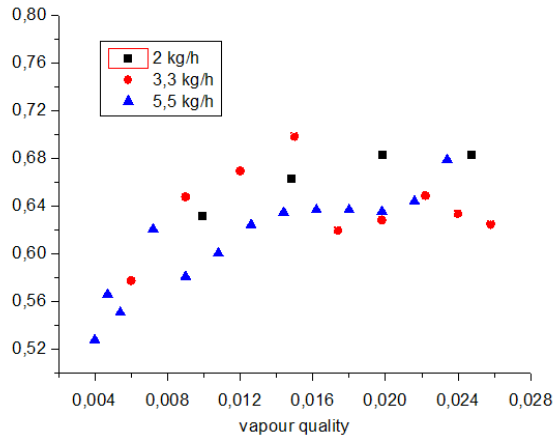
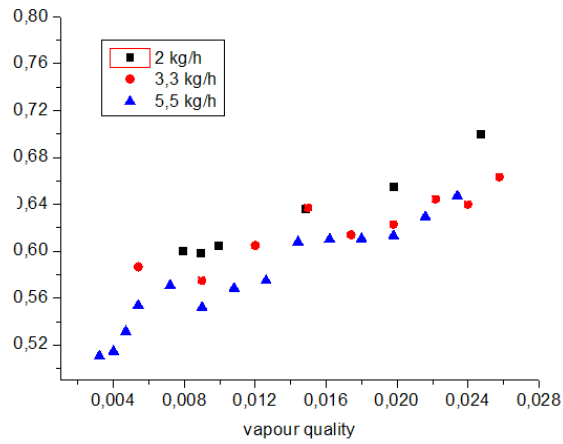
#### 9.2.3. $\tau$ parameter vs vapour quality

Fig. 54 a, b, c represents the values of the  $\tau$  parameter as a function of the mass flux and the vapour quality. The same considerations presented for the two previous cases are valid, but there is a difference.

In this case, the separation of the trend related to the mass flux is not maintained, but especially in the Fig. 54 c it is not possible to see a real separation of the three groups of values according to the mass flux. This fact is mainly due to the fact that coalescence is a statistical phenomena, and so such a variation may be accepted.



**Fig. 53. Dimensionless bubble diameter evolution along the test section tube. a) after the first heater, b) 30 cm ahead of the first position, c) 70 cm ahead of the first position.**



**Fig. 54.  $\tau$  parameter evolution along the test section tube. a) after the first heater, b) 30 cm ahead of the first position, c) 70 cm ahead of the first position.**

## **10.GENERAL CONCLUSIONS**

### **10.1. First group of experiments**

An image processing technique was developed to perform visualization of forced convection saturated R-134a boiling in a horizontal glass mini tube coated with several transparent conductive layers of Indium Tin Oxide (ITO).

In the present case, the inner diameter of the tube was 4 mm and the heated length was globally of 320 mm, distributed in 8 shorter heater of 40 mm each. A dedicated routine was created inside the commercial code Image Pro® Plus to extract the bubble contours, measure geometrical features of each frame and collect the data both analytically and statistically. This two ways of data acquisition allow a first post processing code to analyse and define the flow regime. The method is mostly based on the bubble geometrical features and the statistic analysis of such elements. The range of the flow parameters studied in this section: mass flow rate between 20 and 122 kg/m<sup>2</sup> s and the heat flux between 1200 and 45000 W/m<sup>2</sup>, at the saturation temperatures of 22 °C.

Considering the usual subjective way of flow pattern identification, in the present work with the help of flow visualization the procedure of flow pattern maps definition has been conducted in an alternative way.

Following this way, it has been possible to study the flow pattern in a more objective and statistically based manner, trying to completely avoid the subjectivity of the definition of the common flow pattern maps that can be found in the literature.

In the end, classifying the flow pattern from the statistical point of view it is possible to study the transition lines and expand them in transition zones. This concept is something very innovative in the scientific field, because the transition has always been identified by lined because there weren't the visualization instrument to study the different phases in which a transition from one flow regime to another takes place.

### **10.2. Second group of experiments**

In this section a specific study considering different axial position along the channel has been conducted to study the bubbles evolution along the tube. Due to coalescence, it is possible to see a flow pattern variation along the test section. The experiments demonstrated that coalescence is a phenomenon that can be studied from the statistical point of view, and that the flow pattern changes are not a function of the mass flux.

The effect of coalescence was underlined and shown from the variation of bubbles geometry along the tube, and the key point was also for this part the possibility to visualize the flow inside all the tube.

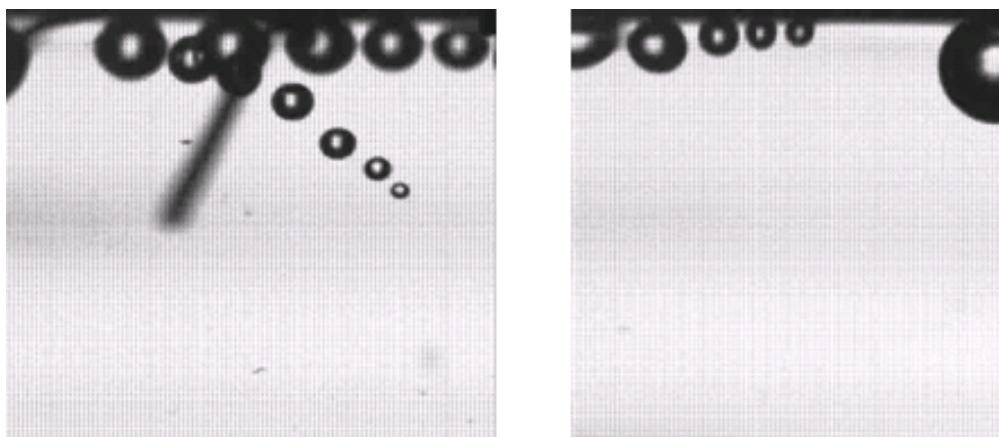
Considering all the experiments performed, it is possible to say that the geometrical data trends seem to be independent on the mass flux.

Moving along the tube from the entrance to the exit region, the flow becomes earlier the elongated bubble regime. This is mainly due to the coalescence of bubbles.

The values of the standard deviation confirm the transition trends found in the first campaign of experiments.

## 11. FUTURE WORK AND LATEST RESULTS

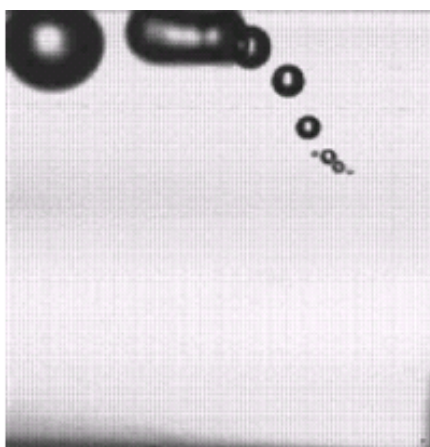
The results presented in the previous chapters and paragraphs represents the earliest stages of the research, because the next step will go down in dimensions to the micro-channels and conduct a deeper study on the diabatic part of the test section.



**Fig. 55. Bubble nucleation inside the test section. a)  $T_{in}= 21^{\circ}\text{C}$ ,  $G=125\text{ kg/m}^2\text{ s}$ , Power= 2 W, first heater; b)  $T_{in}= 21^{\circ}\text{C}$ ,  $G=125\text{ kg/m}^2\text{ s}$ , Power= 3,7 W, first heater**

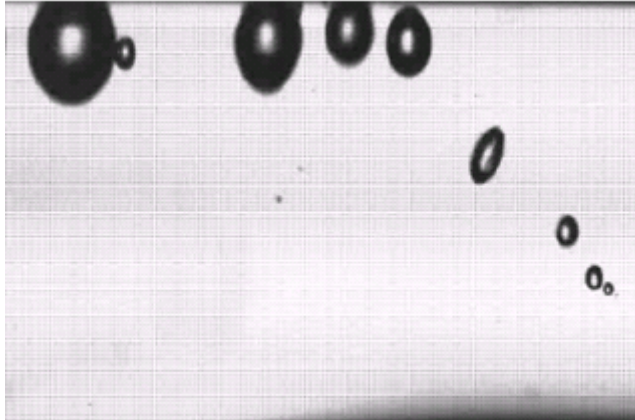
Several videos of the diabatic part of the test section have already been recorded, and in particular they refer to the nucleation point of small bubbles.

Some images taken from the videos are reported in Fig. 55, Fig. 56, Fig. 57, Fig. 58, and in the future a deep study of the nucleation is planned.



**Fig. 56.  $T_{in}= 21^{\circ}\text{C}$ ,  $G=125\text{ kg/m}^2\text{ s}$ , Power= 2 W, second heater**

This direction of the research was chosen because in the scientific literature it is not possible to find any visualization information about the incipient nucleation of bubbles inside small tubes, and so the argument is still very open to discuss.



**Fig. 57.**  $T_{in}= 21^{\circ}\text{C}$ ,  $G=125\text{ kg/m}^2\text{ s}$ ,  $\text{Power}= 2\text{ W}$ , second heater

Also from the heat transfer coefficient point of view this topic is extremely important, because at the incipient boiling condition there is a quick rise in the value of this parameter, and so being able to control and reach this point is a chief key point.



**Fig. 58.**  $T_{in}= 21^{\circ}\text{C}$ ,  $G=70\text{ kg/m}^2\text{ s}$ ,  $\text{Power}= 4\text{ W}$ , second heater

This information are also very useful from the numerical point of view. It is very tricky to simulate the nucleation of bubbles and the correct departing rate. With the help of visualization it will be more easy for the scientists to check the reliability of their codes and improve them quicker.

## BIBLIOGRAPHY

- [1] Lockhart, R.W., Martinelli, R.C., 1949. Proposed correlation of data for isothermal two-phase, two-component flow in pipes. *Chem. Eng. Prog.* 45, 39-48.
- [2] Baker O (1954) Simultaneous flow of oil and gas. *Oil Gas J* 53:185–195.
- [3] Rouhani, S.Z., Axelsson, E., 1970. Calculation of void volume fraction in the subcooled and quality boiling regions. *International Journal of Heat and Mass Transfer* 13, 383-393.
- [4] Premoli, A., Francesco, D., Prina, A., 1971. A dimensionless correlation for determining the density of two-phase mix-tures. *Lo Termotecnica* 25, 17-26.
- [5] Chisholm, D.A., 1973. Pressure gradients due to friction during the flow of evaporating two-phase mixture in smooth tubes and channels. *Int. J. Heat Mass Transfer* 16, 347-358.
- [6] Mandhane JM, Gregory GA, Aziz K (1974) A flow pattern map for gas–liquid flow in horizontal and inclined pipes. *Int J. Multiphase Flow* 1:537–553.
- [7] Butterworth, D., 1975. A comparison of some void-fraction relationships for co-current gas-liquid flow. *Int. J. Multiphase Flow* 1, 845-850.
- [8] Y. Taitel, A.E. Dukler, A model for predicting flow regime transitions in horizontal and near horizontal gas–liquid flow, *AIChE J.* 22 (2) (1976) 43–55.
- [9] Friedel, L., 1979. Improved friction pressure drop correlations for horizontal and vertical two-phase pipe flow. *3R International*, 18 Jahngrang, Hef 7.
- [10] Steiner D (1993) Heat transfer to boiling saturated liquids, *VDI-Warmeatlas (VDI Heat Atlas)*, Verein Deutscher Ingenieure, VDI-Gesellschaft Verfahrenstechnik und Chemieingenieurwesen (GCV), Dusseldorf, Chapter Hbb.
- [11] Wattelet JP (1994) Heat transfer flow regimes of refrigerants in a horizontal-tube evaporator. Ph.D. thesis, University of Illinois, Urbana-Champaign.
- [12] N. Kattan, J.R. Thome, D. Favrat, Measurement and prediction of two-phase flow patterns for new refrigerants inside horizontal tubes, *ASHRAE Trans.* 101 (2) (1995) SD-95-17-4.
- [13] N. Kattan, J.R. Thome, D. Favrat, Flow boiling in horizontal tubes. Part 2—new heat transfer data for five refrigerants, *J Heat Transfer* 120 (1998) 148–155.
- [14] N. Kattan, J.R. Thome, D. Favrat, Flow boiling in horizontal tubes. Part 3: development of a new heat transfer model based on flow patterns, *J. Heat Transfer* 120 (1998) 156–165.
- [15] Kattan, N., Thome, J.R., Favrat, D., 1998. Flow boiling in horizontal tubes: Part 1- Development of a diabatic two-phase flow pattern map. *J. Heat Transfer* 120, 140–147.
- [16] K. A. Triplett, S. M. Ghiaasiaan, S. I. Abdel- Khalik, D. L. Sadowski, Gas-liquid two-phase flow in microchannels, Part I: two-phase flow patterns, *Int. J. Multiphase Flow* 25 (1999) 377-394.

- [17] Didi MB, Kattan N, Thome JR (2002) Prediction of two-phase pressure gradients of refrigerants in horizontal tubes. *Int J Refrigeration* 25:935–947.
- [18] Zurcher O, Farvat D, Thome JR (2002a) Development of a diabatic two-phase flow pattern map for horizontal flow boiling. *Int J Heat Mass Transfer* 45:291–301.
- [19] Zurcher O, Farvat D, Thome JR (2002b) Evaporation of refrigerants in a horizontal tube: and improved flow pattern dependent heat transfer model compared to ammonia data. *Int J Heat Mass Transfer*, 45:303–317.
- [20] Nino VG (2002) Characterization of two-phase flow in microchannels. Ph.D. Thesis, University of Illinois, Urbana- Champaign, IL.
- [21] A. Kawahara, P. M. –Y. Chung, M. Kawaji, Investigation of two-phase flow pattern, void fraction and pressure drop in a microchannel, *Int. J. Multiphase flow* 28 (2002) 1411-1435.
- [22] I. Zun, Phase discrimination vs. multiscale characteristics in bubbly flow, *Exp. Thermal Fluid Science* 26 (2002) 361-374.
- [23] Ming-huei Yu, Tsun-Kuo Lin, Chyuan-chyi Tseng, Heat transfer and flow pattern during two-phase flow boiling of R-134a in horizontal smooth and microfin tubes, *Int. J. Refrigeration* 25 (2002) 789-798.
- [24] J.R. Thome, J. El Hajal, Two-phase flow pattern map for evaporation in horizontal tubes: Latest version, in: 1st Int. Conf. on Heat Transfer, Fluid Mechanics and Thermodynamics, Kruger Park, South Africa, April 8–10, vol. 1, 2002, pp. 182–188.
- [25] G. Hetsroni, A. Mosyak, Z. Segal, E. Pogrebnyak, Two-phase flow patterns in parallel micro-channels, *Int. J. Multiphase Flow* 29 (2003) 341-360.
- [26] A. Zimmermann, A. M. Holland and C.P. Garner, Indium Tin Oxide coated transparent surface for the study of nucleate boiling, *Meas. Sci. Technol.* 14 (2003) 1648-1654.
- [27] Garimella S, Killion JD, Coleman JW (2003) An experimentally validated model for two-phase pressure drop in the intermittent flow regime for noncircular microchannels. *J Fluids Eng* 125:887–894.
- [28] Thome JR, El Hajal J, Cavallini A (2003) Condensation in horizontal tubes, part 2: new heat transfer model based on flow regimes. *Int J Heat Mass Transfer* 46:3365–3387.
- [29] Garimella S (2004) Condensation flow mechanisms in microchannels: basis for pressure drop and heat transfer models. *Heat Transfer Eng* 25(3) 104–116.
- [30] L. Wojtan, T. Ursenbacher, J.R. Thome, Dynamic void fractions in stratified types of flow, Part II: Measurements for R-22 and R-410A, *Int. J. Multiphase Flow* 30 (2004) 125–137.
- [31] R mi Revellin, John R. Thome, Experimental investigation of R-134a and R-245fa two-phase flow in microchannels for different flow conditions, ECI International Conference on Heat Transfer and Fluid Flow in Microscale, Castelvechio Pascoli, 25-30 September 2005.

- [32] Leszek Wojtan, Thierry Ursenbacher, John R. Thome, Investigation of flow boiling in horizontal tubes: Part I – A new diabatic two-phase flow pattern map, *Int. J. Heat Mass Transfer* 48 (2005) 2955-2969.
- [33] Wojtan L, Ursenbacher T, Thome JR (2005a) Investigation of flow boiling in horizontal tubes: part I. A new diabatic two phase flow pattern map. *Int J Heat Mass Transfer* 48:2955– 2969.
- [34] Wojtan L, Ursenbacher T, Thome JR (2005b) Investigation of flow boiling in horizontal tubes: part II. Development of a new heat transfer model for Stratified-Wavy, dryout and mist flow regimes. *Int J Heat Mass Transfer* 48:2970–2985.
- [35] Liebenberg L, Thome J, Meyer J (2005) Flow visualization and flow pattern identification with power spectral density distributions of pressure traces during refrigerant condensation in smooth and microfin tubes. *J Heat Transfer* 127:209–220.
- [36] Revellin, R. (2005) Experimental two-phase fluid flow in microchannels, Ph. D. thesis, University of Lausanne.
- [37] R. Revellin, J. R. Thome, New diabatic flow pattern map for evaporating flows in microchannels.
- [38] Jassim EW, Newell TA (2006) Prediction of two-phase pressure drop and void fraction in microchannels using probabilistic flow regime mapping. *Int J Heat Mass Transfer* 49:2446–2457.
- [39] Revellin, R., Dupont, V., Ursenbacher, T., Thome, J.R., Zun, I., 2006. Characterization of diabatic two-phase flows in microchannels: flow parameter results for R-134a in a 0.5 mm channel. *Int. J. Multiphase Flow* 32.
- [40] Remi Revellin, John R. Thome, Experimental investigation of R-134a and R-245fa two-phase flow in microchannels for different flow conditions, *International Journal of Heat and Fluid Flow* 28 (2007) 63–71.
- [41] Experimental Heat Transfer, Pressure Drop, and Flow Visualization of R-134a in Vertical Mini/Micro Tubes, Doctoral Thesis by Wahib Owhaib, Royal Institute of Technology, KTH Stockholm, Sweden 2007.
- [42] Jassim EW, Newell TA, Chato J. (2007) Probabilistic determination of two-phase flow regimes in horizontal tubes utilizing an automated image recognition technique. *Exp. Fluids* 42:563-573.
- [43] S. Dall'Olio, M. Marengo, G. E. Cossali (2008), Flow pattern map and high speed camera observation of boiling R134a in a glass minitube heated by a ITO technique: an attempt to obtain an automatic flow pattern characterization. XXVI Congresso Nazionale UIT sulla Trasmissione del Calore Palermo, 23-25 Giugno 2008.
- [44] S. Dall'Olio, M. Marengo, S. Zinna, C. Antonini, G. E. Cossali (2008), Description, uncertainty analysis and simulation of a new test rig for refrigerant two-phase flow characterization. ECI, heat transfer and fluid flow in microscale III, sept. 2008, Canada.
- [45] S. Dall'Olio, M. Marengo, G. E. Cossali (2008), A probabilistic criterion related to bubble size for automatic flow pattern identification in R134a two-phase flow, 1st

European Conference on Microfluidics - Microfluidics 2008 - Bologna, December 10-12, 2008.

[46] Remi Revellin, Bruno Agostini, Thierry Ursenbacher, John R. Thome, Experimental investigation of velocity and length of elongated bubbles for flow of R-134a in a 0.5 mm microchannel, *Experimental Thermal and Fluid Science* 32 (2008) 870–881.

[47] K. A. Triplett, S. M. Ghiaasiaan, S. I. Abdel-Khalik, A. LeMouel, B. N. McCord, Gas-liquid two-phase flow in microchannels Part II: void fraction and pressure drop, *Int. J. Multiphase Flow* 25 (1999) 395-410.

[48] Leszek Wojtan, Thierry Ursenbacher, John R. Thome, Measurement of dynamic void fractions in stratified types of flow, *Exp. Thermal Fluid Science*, 29 (2005) 383-392.

## PUBLICATIONS

Marengo M., Rioboo R, Vou M, Dall'Olio S, De Coninck J. (2007). Devices and method for enhanced heat transfer. EP 07113887.9-1266. Université de Mons-Hainaut.

S. Dall'Olio, M. Marengo, G. E. Cossali (2008), Flow pattern map and high speed camera observation of boiling R134a in a glass minitube heated by a ITO technique: an attempt to obtain an automatic flow pattern characterization. XXVI Congresso Nazionale UIT sulla Trasmissione del Calore Palermo, 23-25 Giugno 2008.

S. Dall'Olio, M. Marengo, S. Zinna, C. Antonini, G. E. Cossali (2008), Description, uncertainty analysis and simulation of a new test rig for refrigerant two-phase flow characterization. ECI, heat transfer and fluid flow in microscale III, sept. 2008, Canada.

S. Dall'Olio, M. Marengo, G. E. Cossali (2008), A probabilistic criterion related to bubble size for automatic flow pattern identification in R134a two-phase flow, 1st European Conference on Microfluidics - Microfluidics 2008 - Bologna, December 10-12, 2008.

R. Rioboo, M. Marengo, S. Dall'Olio, M. Voue, and J. De Coninck (2009), An innovative method to control the incipient flow boiling through grafted surfaces with chemical pattern, Langmuir.

S. Dall'Olio, M. Marengo, I. Zun (2009), An analysis of R134a incipient boiling inside a transparent minichannel, ExHFT-7, 7th World Conference on Experimental Heat Transfer, Fluid Mechanics and Thermodynamics, Krakow, Poland June 28 - July 03, 2009.

S. Dall'Olio, M. Marengo (2009), A new approach of flow pattern characterization based on flow visualization, Int. J. of Heat and Mass Transfer.

Leonid Vasiliev, Marco Marengo, Stefano Zinna, Claudio Ferrandi, Stefano Dall'Olio, (2009), Advanced design of a low cost loop heat pipe with flexible polymer lines, Texas 2009.

S. Dall'Olio, M. Marengo (2009), Flow pattern evolution of boiling R134a along a transparent test section: a visualization study based on several statistical parameters, XXVII Congresso UIT - Reggio Emilia 22-24 Giugno 2009.

## **APPENDIX**

### **I. IMAGE ANALYSIS OF A TWO PHASE FLOW IN A BUNDLE OF MINI-CHANNELS USING THE COMMERCIAL CODE IMAGE PRO® PLUS R 4.5.1**

During the PhD period, I spent four months at the University of Ljubljana, Slovenia. My supervisor was Prof. Iztok Zun, and the object of this part of the work was to find the fastest and most accurate way to extract the bubbles contour in an air and water artificially created two-phase flow inside a bundle of mini-channels.

#### **I.1. The processed videos**

During this work, about 18 videos were processed using Image-Pro® Plus, and just the first 50 frames of each were considered due to the calculation capabilities of the computer used.



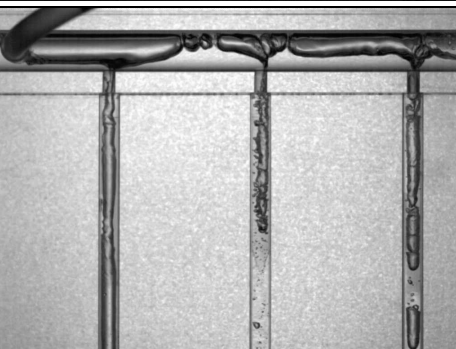
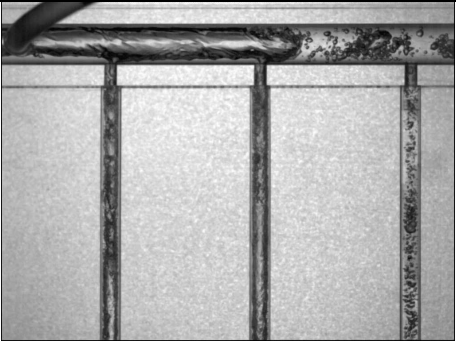
Computing with a more powerful calculator, the code can easily process all the entire videos with the same accuracy and with the same macro described in the following pages.

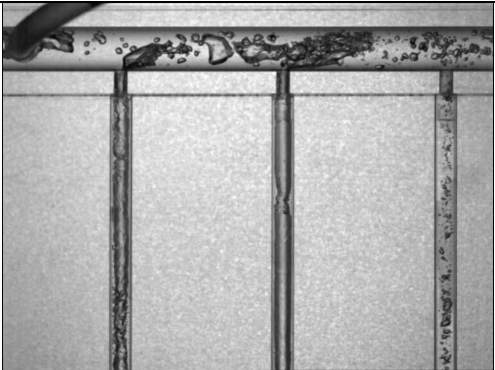
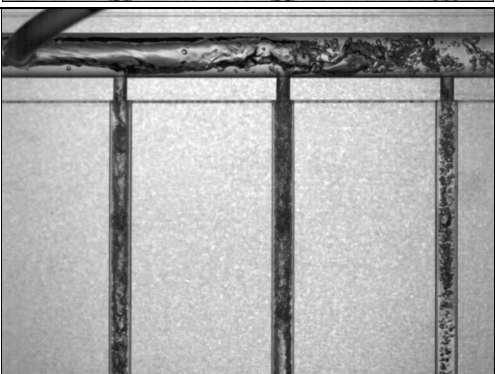


During the analysis, almost every kind of fluid patterns were encountered and considered: mainly bubbly flow, bubbly-slug flow and slug flow.





All the videos were recorded by a high speed digital camera in RGB mode and then converted into grey scale 8 bit videos.



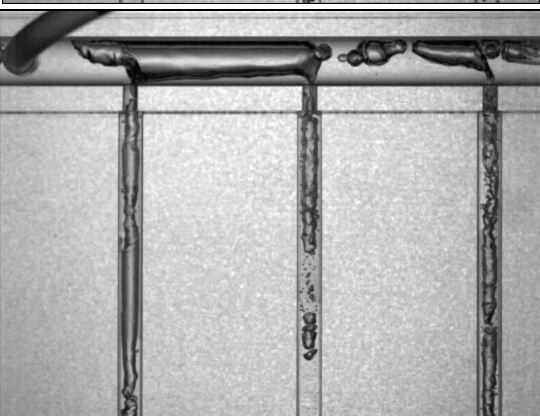
As mentioned before, about 18 videos were processed, each one with a different volumetric flow rate of the liquid phase and gas phase.


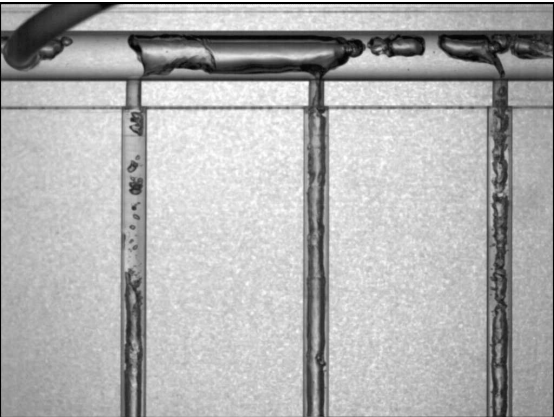
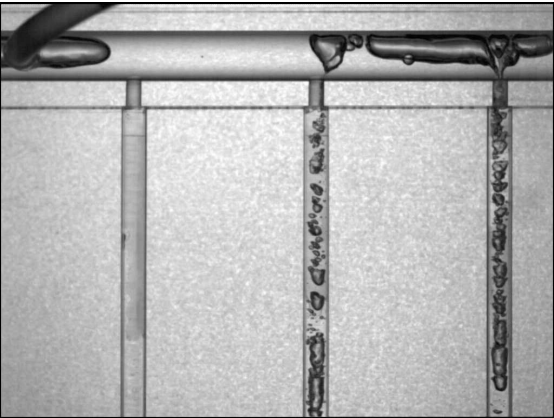
In the following table the complete range considered is reported:

Volumetric flow rate of the liquid phase l/h	Volumetric flow rate of the gas phase l/h	Image of the Flow
<i>100</i>	80	
<i>100</i>	120	
<i>100</i>	160	
<i>100</i>	400	

100	600	
100	1000	
120	80	
120	120	

120	160	
120	200	
<i>140</i>	80	
<i>140</i>	120	

140	160	
140	200	
<b>160</b>	80	

160	120	
160	160	
160	200	

**Tab. 2. Complete range of videos analysed.**

## **I.2. The main steps of bubble contour extraction**

To extract the contour of the bubble fraction from the videos recorded, many procedures have been tested in order to reach the one that could achieve the best results

with the minimum number of operations. This last characteristic of the procedure is very important, because of the speed of the analysis is obviously inversely proportional to the number of steps required to reach the final result.

After many attempts a single procedure suitable for all the flow regimes and channel diameter was identified and written as a macro, which is an executable that contains some specialized routines to run before or after capturing an image or a video.

One of the major advantages of using Image-Pro® Plus is the ability to record and use macros. Macros are programming scripts that call the programming language of Image-Pro Plus to automatically execute tasks.

To begin with the processing, we have first to open two files: the video to be analyzed and the background image with the channel full of liquid. This image is very important and the final result after applying the macro depend on the quality of the background image: it must be recorded exactly in the same position and light condition as the video, otherwise the resulting videos will have a lot of noise and the bubble contour will be less precise.

All the operations are based on the fact that the videos are first converted in a grey scale 8-bit format. With this operation, we know that the pixel values of each frame will be between 0 (completely dark image) and 255 (completely white image).

After this conversion, the pixel value absolute difference between the background image and each frame of the video is processed, and images that have an average pixel value of 3-5 out of the channels and where there is the liquid phase, and an average value of 120-255 for the gas phase, are obtained.

Now it is important to completely separate the gas from the liquid and the background, and this is achieved in two steps: first the subtraction of 7 to all the pixel of the images of the video, and then their power to 1.8.

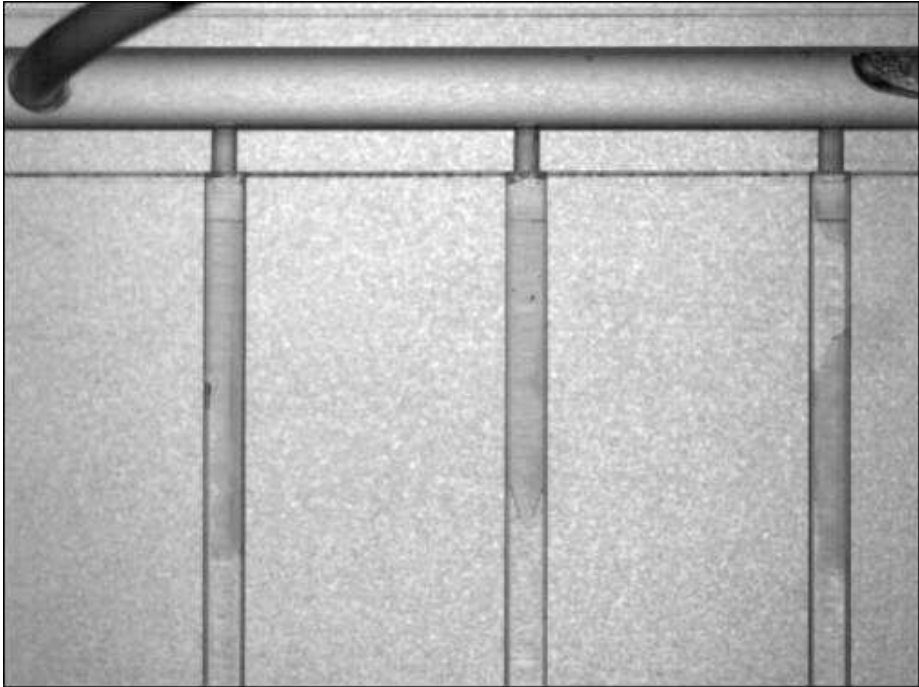
As a result, with these operations we obtain frames in which the background and the liquid phase are completely in black (0 pixel value), and the gas phase is almost completely white ( from 150 to 255 pixel value).

Having the two phases completely splitted, it is possible to extract the contour of the gas phase with other two main steps, the count/size command and the application of a particular filter created for this aim.

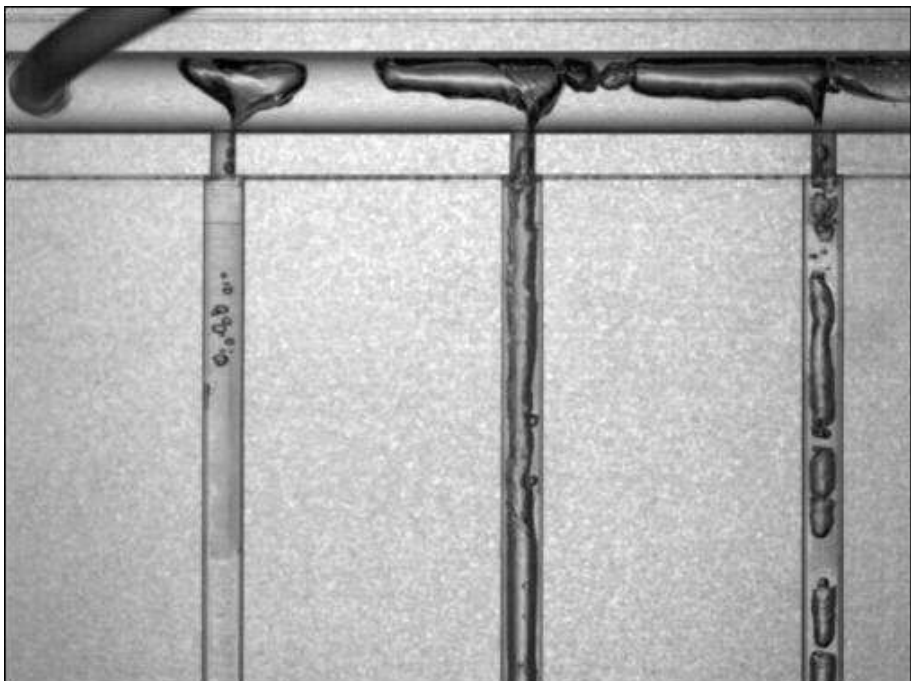
There are some intermediate steps in which the images are cleaned, but they will be just mentioned later because they are of secondary importance.

In the following, an example of the application of the procedure described before is reported step by step:

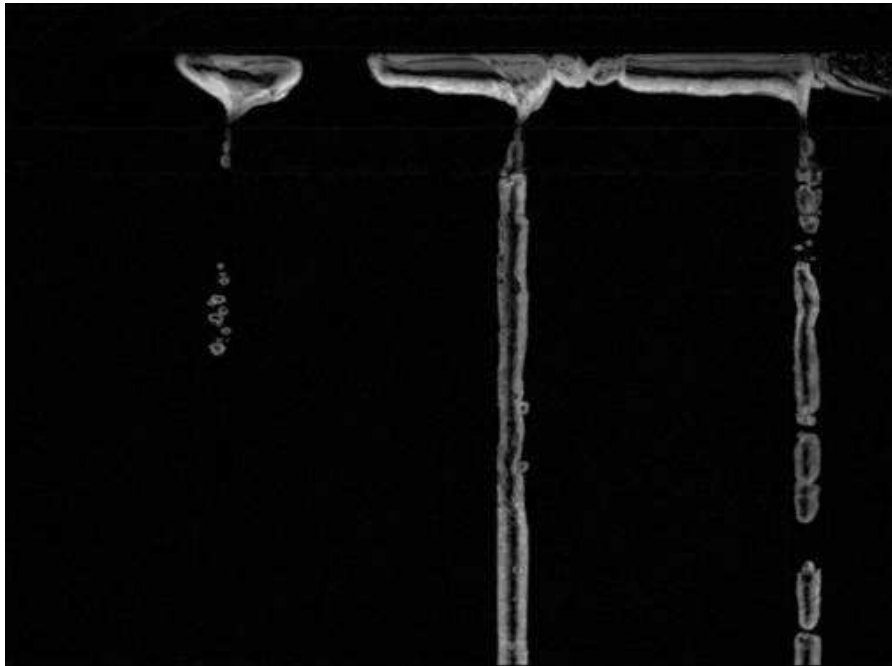
- the background image, with all the channels full of liquid:



- one frame of a video:  $v_l$  of 100 l/h and  $v_g$  of 120 l/h



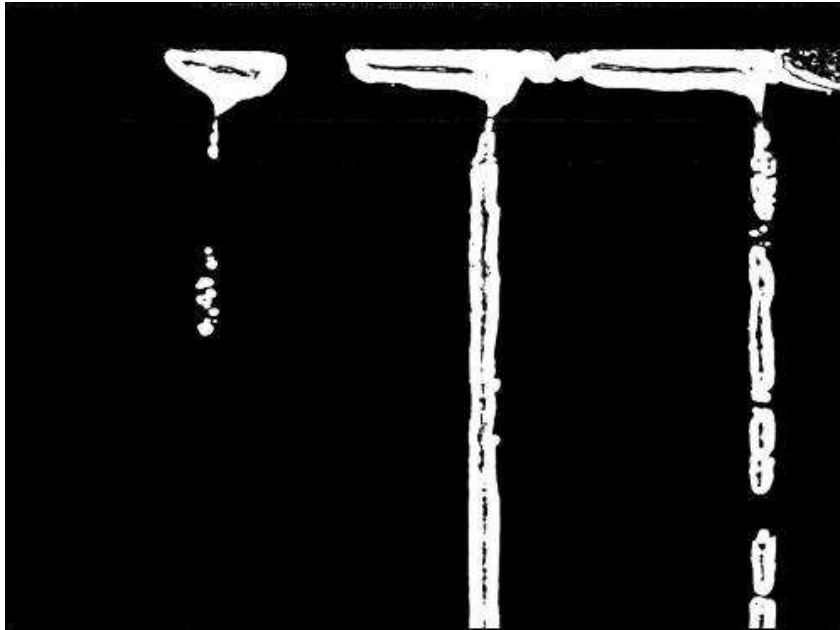
- absolute difference between the background image and the previous frame:



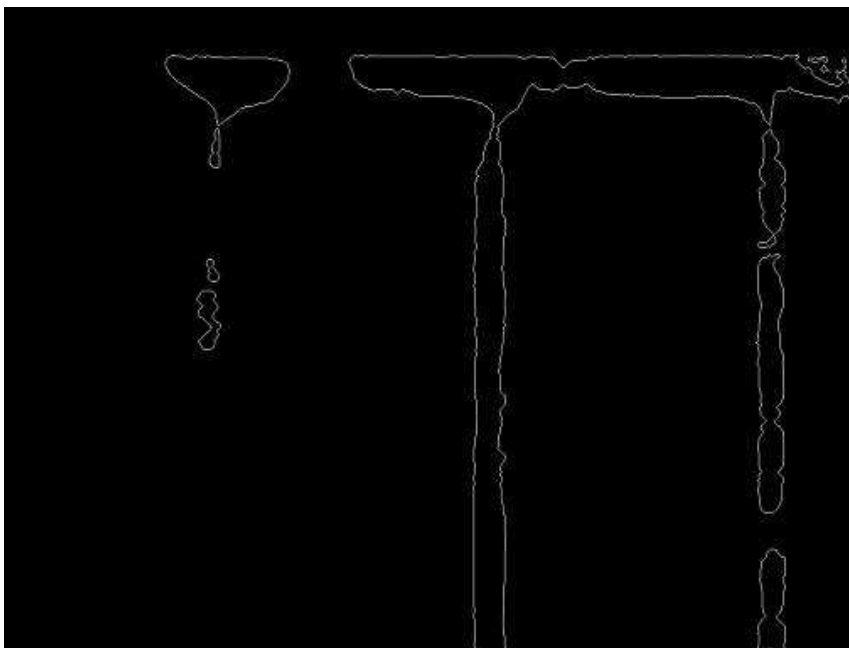
- subtraction of 7 to each pixel of the frame:



- power to 1.8 of the pixel value of the frame:



- count/size button: unfortunately this step can't be seen alone, but it is just possible to see the final result;
- final result:



- superposition of the original image and the latest result:



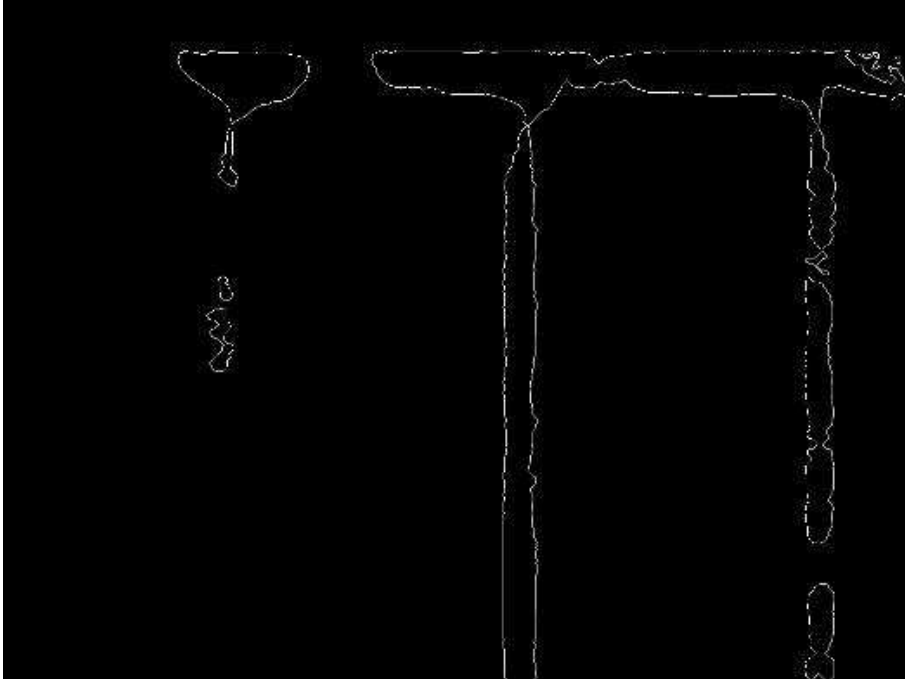
This last image is very important to prove the accuracy of the program and of the macro used to perform the analysis, and it will be discussed later in the results and conclusions sections.

### **I.3. Results**

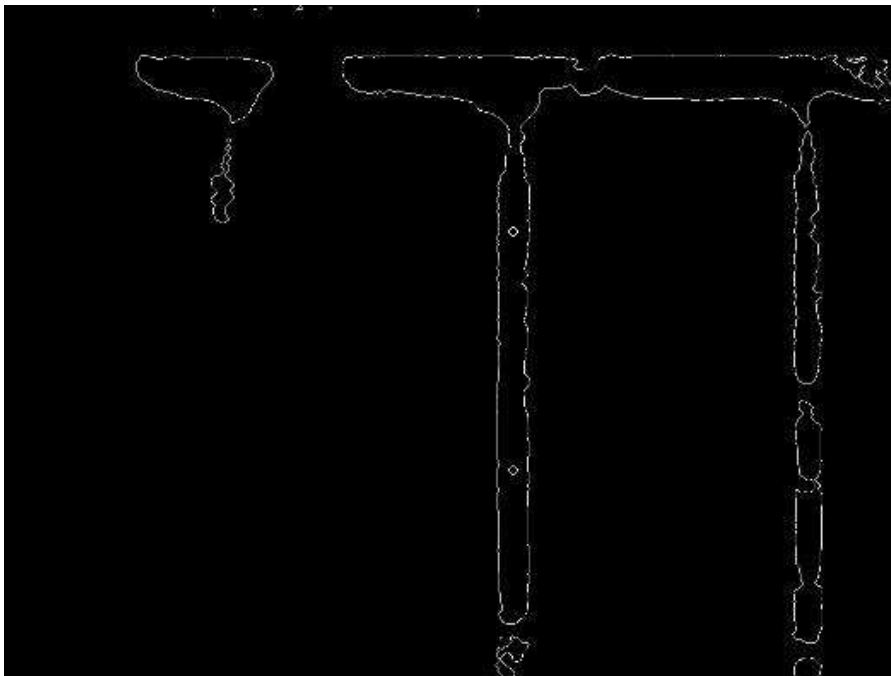
As results of the work done, some significant images are reported below in Fig. 59, Fig. 60, Fig. 61, Fig. 62, Fig. 63 and Fig. 64.

To understand the accuracy of the macro and of the commercial code Image-Pro® Plus, the processed videos can be analysed. To have a superior and more objective opinion, the superimposition between the original video and the contour video seems to be necessary.

With this second operation, it comes much more evident how the contours extracted follow the real contours of the original videos.



**Fig. 59.** Image resulting from the processing of the VI100vg120 video.



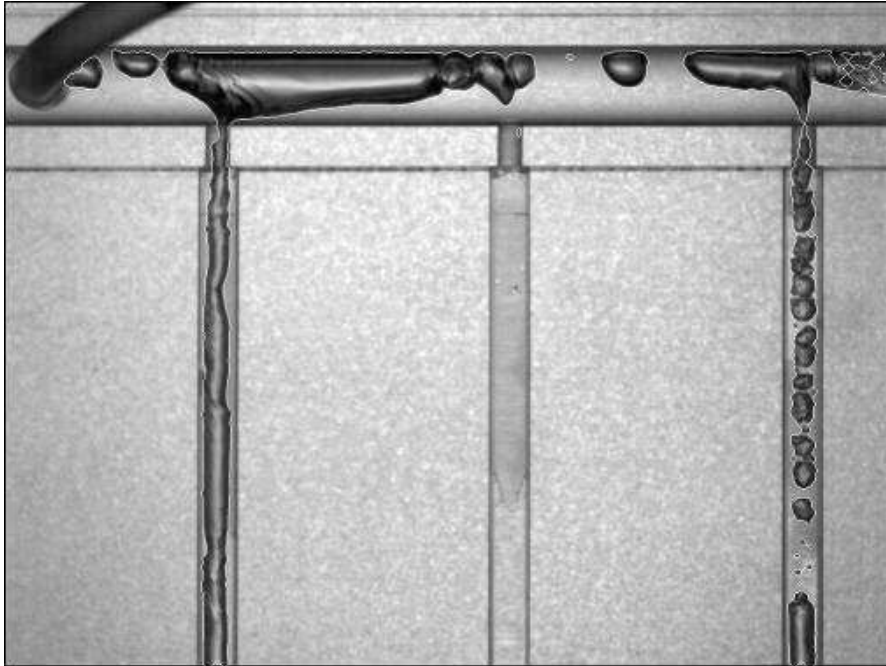
**Fig. 60.** Image resulting from the processing of the VI100vg120 video.



**Fig. 61.** Image resulting from the superposition of the original image and the processed image of the V1100vg120 video.



**Fig. 62.** Image resulting from the superposition of the original image and the processed image of the V1120vg80 video.



**Fig. 63.** Image resulting from the superposition of the original image and the processed image of the V1140vg80 video.



**Fig. 64.** Image resulting from the superposition of the original image and the processed image of the V1160vg80 video.

#### **I.4. Conclusions**

At the end of this part of the work, an easy to use procedure to extract gas contours from videos was created and well tested and optimized.

There are anyway some lacks in the program, in the sense that especially when the bubbles are very small or very close to each other they are seen as one entire bubble and it is not possible to divide the them into two or more contours.

On the other hand, the macro can be easily used and improved for other setups of microchannels just by changing some parameters within an optimisation procedure.

In the end, it is important to underline once again that the final results will be as good as the background image is taken in the same operating conditions in which the videos will be recorded.

## II. Fluid Physical properties

Properties of Liquid R134a

Temperature (C)	Pressure (bar)	Density (l, kg/m3)	Volume (l, m3/kg)	Internal Energy (l, kJ/kg)	Enthalpy (l, kJ/kg)	Entropy (l, J/g*K)	Cv (l, J/g*K)	Cp (l, J/g*K)	Viscosity (l, uPa*s)	Therm. Cond. (l, W/m*K)	Surf. Tension (l, N/m)
-20	1,3273	1358,3	0,000736	173,54	173,64	0,90025	0,85511	1,293	347,58	0,10107	0,014513
-19	1,3857	1355,2	0,000738	174,83	174,93	0,90534	0,85627	1,2952	342,81	0,10061	0,014362
-18	1,446	1352,1	0,00074	176,12	176,23	0,91042	0,85743	1,2973	338,12	0,10014	0,014212
-17	1,5084	1349	0,000741	177,42	177,53	0,91549	0,8586	1,2995	333,52	0,099684	0,014062
-16	1,5728	1345,9	0,000743	178,72	178,83	0,92054	0,85977	1,3017	329	0,099225	0,013912
-15	1,6394	1342,8	0,000745	180,02	180,14	0,92559	0,86095	1,304	324,56	0,098767	0,013762
-14	1,7082	1339,7	0,000746	181,32	181,44	0,93062	0,86212	1,3062	320,21	0,09831	0,013613
-13	1,7792	1336,6	0,000748	182,62	182,75	0,93564	0,86331	1,3085	315,93	0,097854	0,013464
-12	1,8524	1333,4	0,00075	183,93	184,07	0,94066	0,8645	1,3108	311,73	0,097398	0,013315
-11	1,928	1330,3	0,000752	185,24	185,38	0,94566	0,86569	1,3132	307,61	0,096944	0,013167
-10	2,006	1327,1	0,000754	186,55	186,7	0,95065	0,86688	1,3156	303,55	0,096491	0,013019
-9	2,0864	1323,9	0,000755	187,86	188,02	0,95563	0,86809	1,318	299,56	0,096039	0,012872
-8	2,1693	1320,8	0,000757	189,17	189,34	0,9606	0,86929	1,3204	295,65	0,095588	0,012725
-7	2,2548	1317,6	0,000759	190,49	190,66	0,96556	0,8705	1,3229	291,79	0,095138	0,012578
-6	2,3428	1314,3	0,000761	191,81	191,99	0,97051	0,87171	1,3254	288	0,094689	0,012431
-5	2,4334	1311,1	0,000763	193,13	193,32	0,97544	0,87293	1,3279	284,28	0,094241	0,012285
-4	2,5268	1307,9	0,000765	194,45	194,65	0,98037	0,87415	1,3304	280,61	0,093794	0,012139
-3	2,6228	1304,6	0,000767	195,78	195,98	0,98529	0,87538	1,333	277,01	0,093347	0,011994
-2	2,7217	1301,4	0,000768	197,11	197,32	0,99021	0,87661	1,3357	273,46	0,092902	0,011849
-1	2,8234	1298,1	0,00077	198,44	198,66	0,99511	0,87785	1,3383	269,96	0,092457	0,011704
0	2,928	1294,8	0,000772	199,77	200	1	0,87909	1,341	266,53	0,092013	0,01156
1	3,0356	1291,5	0,000774	201,11	201,34	1,0049	0,88034	1,3438	263,14	0,09157	0,011416
2	3,1462	1288,1	0,000776	202,45	202,69	1,0098	0,88159	1,3466	259,81	0,091128	0,011272
3	3,2598	1284,8	0,000778	203,79	204,04	1,0146	0,88284	1,3494	256,53	0,090687	0,011129
4	3,3766	1281,4	0,00078	205,13	205,4	1,0195	0,8841	1,3523	253,29	0,090246	0,010986
5	3,4966	1278,1	0,000782	206,48	206,75	1,0243	0,88537	1,3552	250,11	0,089806	0,010844
6	3,6198	1274,7	0,000785	207,83	208,11	1,0292	0,88664	1,3581	246,97	0,089367	0,010702
7	3,7463	1271,3	0,000787	209,18	209,47	1,034	0,88791	1,3611	243,88	0,088929	0,01056
8	3,8761	1267,9	0,000789	210,53	210,84	1,0388	0,8892	1,3641	240,83	0,088491	0,010419
9	4,0094	1264,4	0,000791	211,89	212,21	1,0437	0,89048	1,3672	237,83	0,088054	0,010278

10	4,1461	1261	0,000793	213,25	213,58	1,0485	0,89177	1,3704	234,87	0,087618	0,010138
11	4,2863	1257,5	0,000795	214,61	214,95	1,0533	0,89307	1,3736	231,95	0,087182	0,0099975
12	4,4301	1254	0,000797	215,98	216,33	1,0581	0,89437	1,3768	229,07	0,086747	0,0098579
13	4,5776	1250,5	0,0008	217,34	217,71	1,0629	0,89568	1,3801	226,22	0,086312	0,0097186
14	4,7288	1246,9	0,000802	218,71	219,09	1,0677	0,897	1,3835	223,42	0,085878	0,0095797
15	4,8837	1243,4	0,000804	220,09	220,48	1,0724	0,89832	1,3869	220,66	0,085444	0,0094413
16	5,0425	1239,8	0,000807	221,46	221,87	1,0772	0,89964	1,3903	217,93	0,085011	0,0093033
17	5,2052	1236,2	0,000809	222,84	223,26	1,082	0,90097	1,3939	215,24	0,084579	0,0091657
18	5,3718	1232,6	0,000811	224,23	224,66	1,0867	0,90231	1,3975	212,58	0,084147	0,0090285
19	5,5424	1229	0,000814	225,61	226,06	1,0915	0,90366	1,4011	209,96	0,083715	0,0088918
20	5,7171	1225,3	0,000816	227	227,47	1,0962	0,90501	1,4049	207,37	0,083284	0,0087555
21	5,8959	1221,7	0,000819	228,39	228,88	1,101	0,90636	1,4087	204,81	0,082854	0,0086196
22	6,0789	1218	0,000821	229,79	230,29	1,1057	0,90773	1,4125	202,28	0,082423	0,0084841
23	6,2662	1214,2	0,000824	231,19	231,7	1,1105	0,9091	1,4165	199,79	0,081993	0,0083492
24	6,4578	1210,5	0,000826	232,59	233,12	1,1152	0,91048	1,4205	197,32	0,081564	0,0082146
25	6,6538	1206,7	0,000829	233,99	234,55	1,1199	0,91186	1,4246	194,89	0,081134	0,0080805
26	6,8543	1202,9	0,000831	235,4	235,97	1,1246	0,91326	1,4288	192,48	0,080705	0,0079469
27	7,0592	1199,1	0,000834	236,82	237,4	1,1294	0,91466	1,4331	190,1	0,080277	0,0078137
28	7,2688	1195,2	0,000837	238,23	238,84	1,1341	0,91607	1,4375	187,75	0,079848	0,007681
29	7,483	1191,4	0,000839	239,65	240,28	1,1388	0,91748	1,4419	185,42	0,07942	0,0075488
30	7,702	1187,5	0,000842	241,07	241,72	1,1435	0,9189	1,4465	183,13	0,078992	0,007417

# Properties of Vapor R134a

Temperature (C)	Pressure (bar)	Density (v, kg/m3)	Volume (v, m3/kg)	Internal Energy (v, kJ/kg)	Enthalpy (v, kJ/kg)	Entropy (v, J/g*K)	Cv (v, J/g*K)	Cp (v, J/g*K)	Viscosity (v, uPa*s)	Therm. Cond. (v, W/m*K)
-20	1,3273	6,7845	0,14739	366,99	386,55	1,7413	0,70464	0,8158	9,9995	0,0098164
-19	1,3857	7,0662	0,14152	367,56	387,17	1,7404	0,70735	0,81948	10,036	0,0098996
-18	1,446	7,3571	0,13592	368,13	387,79	1,7396	0,71007	0,8232	10,072	0,009983
-17	1,5084	7,6574	0,13059	368,7	388,4	1,7387	0,7128	0,82695	10,108	0,010067
-16	1,5728	7,9673	0,12551	369,28	389,02	1,7379	0,71555	0,83075	10,144	0,01015
-15	1,6394	8,287	0,12067	369,85	389,63	1,7371	0,7183	0,83458	10,181	0,010234
-14	1,7082	8,6168	0,11605	370,41	390,24	1,7363	0,72106	0,83845	10,217	0,010318
-13	1,7792	8,9568	0,11165	370,98	390,85	1,7355	0,72384	0,84237	10,253	0,010402
-12	1,8524	9,3074	0,10744	371,55	391,46	1,7348	0,72662	0,84632	10,289	0,010486
-11	1,928	9,6688	0,10343	372,12	392,06	1,7341	0,72941	0,85031	10,325	0,010571
-10	2,006	10,041	0,09959	372,69	392,66	1,7334	0,73222	0,85435	10,362	0,010655
-9	2,0864	10,425	0,095925	373,25	393,27	1,7327	0,73503	0,85843	10,398	0,01074
-8	2,1693	10,82	0,092422	373,82	393,87	1,732	0,73786	0,86255	10,434	0,010825
-7	2,2548	11,227	0,089072	374,38	394,47	1,7313	0,74069	0,86672	10,471	0,010911
-6	2,3428	11,646	0,085867	374,95	395,06	1,7307	0,74354	0,87094	10,507	0,010996
-5	2,4334	12,077	0,082801	375,51	395,66	1,73	0,74639	0,8752	10,543	0,011082
-4	2,5268	12,521	0,079866	376,07	396,25	1,7294	0,74926	0,8795	10,58	0,011168
-3	2,6228	12,978	0,077055	376,63	396,84	1,7288	0,75214	0,88386	10,616	0,011254
-2	2,7217	13,448	0,074362	377,19	397,43	1,7282	0,75502	0,88827	10,653	0,01134
-1	2,8234	13,931	0,071782	377,75	398,02	1,7276	0,75792	0,89272	10,689	0,011427
0	2,928	14,428	0,069309	378,31	398,6	1,7271	0,76082	0,89723	10,726	0,011514
1	3,0356	14,939	0,066937	378,87	399,19	1,7265	0,76374	0,90179	10,763	0,011601
2	3,1462	15,465	0,064663	379,42	399,77	1,726	0,76666	0,90641	10,8	0,011689
3	3,2598	16,005	0,06248	379,98	400,34	1,7255	0,7696	0,91108	10,837	0,011777
4	3,3766	16,56	0,060385	380,53	400,92	1,725	0,77254	0,91581	10,874	0,011865
5	3,4966	17,131	0,058374	381,08	401,49	1,7245	0,7755	0,92059	10,911	0,011954

6	3,6198	17,717	0,056443	381,63	402,06	1,724	0,77846	0,92544	10,948	0,012043
7	3,7463	18,319	0,054587	382,18	402,63	1,7235	0,78144	0,93035	10,986	0,012132
8	3,8761	18,938	0,052804	382,73	403,2	1,723	0,78442	0,93532	11,023	0,012221
9	4,0094	19,573	0,05109	383,27	403,76	1,7226	0,78742	0,94036	11,061	0,012312
10	4,1461	20,226	0,049442	383,82	404,32	1,7221	0,79042	0,94546	11,099	0,012402
11	4,2863	20,896	0,047857	384,36	404,88	1,7217	0,79344	0,95063	11,137	0,012493
12	4,4301	21,584	0,046332	384,9	405,43	1,7212	0,79646	0,95588	11,175	0,012584
13	4,5776	22,29	0,044864	385,44	405,98	1,7208	0,7995	0,96119	11,214	0,012676
14	4,7288	23,015	0,043451	385,98	406,53	1,7204	0,80254	0,96659	11,252	0,012769
15	4,8837	23,758	0,04209	386,52	407,07	1,72	0,8056	0,97206	11,291	0,012862
16	5,0425	24,522	0,04078	387,05	407,61	1,7196	0,80866	0,97761	11,33	0,012955
17	5,2052	25,305	0,039517	387,58	408,15	1,7192	0,81174	0,98324	11,369	0,013049
18	5,3718	26,109	0,038301	388,11	408,69	1,7188	0,81482	0,98896	11,409	0,013144
19	5,5424	26,934	0,037128	388,64	409,22	1,7184	0,81792	0,99476	11,448	0,013239
20	5,7171	27,78	0,035997	389,17	409,75	1,718	0,82103	1,0007	11,488	0,013335
21	5,8959	28,648	0,034906	389,69	410,27	1,7177	0,82415	1,0067	11,529	0,013431
22	6,0789	29,539	0,033854	390,21	410,79	1,7173	0,82728	1,0127	11,569	0,013528
23	6,2662	30,452	0,032838	390,73	411,31	1,7169	0,83042	1,0189	11,61	0,013626
24	6,4578	31,389	0,031858	391,25	411,82	1,7166	0,83357	1,0252	11,651	0,013725
25	6,6538	32,35	0,030912	391,77	412,33	1,7162	0,83673	1,0316	11,693	0,013825
26	6,8543	33,335	0,029998	392,28	412,84	1,7159	0,83991	1,0382	11,735	0,013925
27	7,0592	34,346	0,029115	392,79	413,34	1,7155	0,8431	1,0448	11,777	0,014026
28	7,2688	35,382	0,028263	393,29	413,84	1,7152	0,8463	1,0516	11,82	0,014129
29	7,483	36,445	0,027438	393,8	414,33	1,7148	0,84951	1,0585	11,863	0,014232
30	7,702	37,535	0,026642	394,3	414,82	1,7145	0,85273	1,0655	11,907	0,014336

